



**HAL**  
open science

# Etude de la cinétique des particules dans les couches frontières de la magnétosphère terrestre à l'aide des observations des satellites CLUSTER et DOUBLE STAR

Chunlin Cai

## ► To cite this version:

Chunlin Cai. Etude de la cinétique des particules dans les couches frontières de la magnétosphère terrestre à l'aide des observations des satellites CLUSTER et DOUBLE STAR. Planète et Univers [physics]. Université Paul Sabatier - Toulouse III, 2010. Français. NNT: . tel-00499367

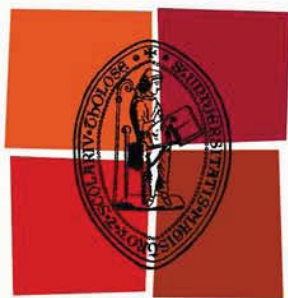
**HAL Id: tel-00499367**

**<https://theses.hal.science/tel-00499367>**

Submitted on 9 Jul 2010

**HAL** is a multi-disciplinary open access archive for the deposit and dissemination of scientific research documents, whether they are published or not. The documents may come from teaching and research institutions in France or abroad, or from public or private research centers.

L'archive ouverte pluridisciplinaire **HAL**, est destinée au dépôt et à la diffusion de documents scientifiques de niveau recherche, publiés ou non, émanant des établissements d'enseignement et de recherche français ou étrangers, des laboratoires publics ou privés.



Université  
de Toulouse

# THÈSE

En vue de l'obtention du  
**DOCTORAT DE L'UNIVERSITÉ DE TOULOUSE**

**Délivré par :**

Université Toulouse 3 Paul Sabatier (UT3 Paul Sabatier)

**Discipline ou spécialité :**

Astrophysique/Physique des plasmas spatiaux

---

**Présentée et soutenue par :**

Chunlin CAI

**le :** 22 Juin 2010

**Titre :**

Etude de la cinétique des particules dans les couches frontières de la magnétosphère terrestre à l'aide des observations des satellites CLUSTER et DOUBLE STAR

---

**JURY**

Prof Jinbin CAO, Dr Iannis DANDOURAS  
Dr Dominique DELCOURT, Dr Dominique FONTAINE  
Prof George K. PARKS, Dr Michel PARROT  
Prof Henri RÈME

---

**Ecole doctorale :**

Sciences de l'Univers, de l'Environnement et de l'Espace (SDU2E)

**Unité de recherche :**

Centre d'Etude Spatiale des Rayonnements

**Directeur(s) de Thèse :**

Professeur Henri RÈME/Docteur Iannis DANDOURAS

**Rapporteurs :**

Dr Dominique DELCOURT et Dr Michel PARROT



**Etude de la cinétique des particules dans les couches-frontières de la magnétosphère terrestre à l'aide des observations des satellites CLUSTER et DOUBLE STAR**

**Analysis of particle kinetics within boundary layers of the Earth's magnetosphere using CLUSTER and DOUBLE STAR data**



## **Acknowledgements**

I express my deepest gratitude to my supervisor Professor Henri Rème. He has guided me not only in my research work but also in other aspects of life. I am also obliged to him and Madam for their helps in many personal matters.

I am deeply grateful to Dr. Iannis Dandouras and Dr. Jinbin Cao. Without their invaluable aides, this thesis would not be possible.

I greatly appreciate Dr. G.K.Parks and Dr. D.Fontaine for their indispensable academic guidance.

I would like to acknowledge many persons from CESR, Dr. C. Mazelle, Dr. C. Aoustin, Dr. E.Penou, Dr. Christopher Harvey, for providing me many facilities both in my resacher work and in personal affairs.

I am grateful to Prof. G.C.Zhou for his continuous advice from the beginning of my academic career as a graduate student supervised by him, not only in my scientific research but also in personal life.

I am thankful to many members of CSSAR, Dr. Y.D.Ma, Dr. X.H.Wei, Dr.H.S.Fu, for their support throughout the task of this research work.

I would like to acknowledge the French Embassy in China for offering me a government scholarship and providing the financial assistance.

I am grateful to Dr. Jean-André Sauvaud, Director of the Centre d'Etude Spatiale des Rayonnements, for the hospitality during my staying in the laboratory.

I am also thankful to the CROUS of Toulouse for organizing my government scholarship and supplying me many facilities for my living in France.

I express my deepest gratitude to my father and my sister. Their encouragement gives me unexhausted mental strength in my academic career.

Finally, I wish to record my deepest obligations to my child and my wife for their love, patience and understanding.



## Table des matières

<b>Résumé</b>	<b>7</b>
<b>Abstract</b>	<b>10</b>
<b>Introduction (en français)</b>	<b>13</b>
<b>Introduction (in english)</b>	<b>16</b>
<b>1 The magnetosphere</b>	<b>19</b>
1. Introduction	19
2. The bow shock and the magnetosheath	19
3. The magnetopause	22
4. The magnetotail	23
5. Magnetic reconnection	25
<b>2 Instrumentation</b>	<b>29</b>
1. The Cluster mission	29
2. The CIS experiment	30
3. The fluxgate magnetometer	34
4. The Double Star Program	35
<b>3 Magnetosheath excursion and transport process at the magnetopause</b>	<b>39</b>
1. Introduction	39
2. Observations	40
3. Discussion	50
3.1 Excursion velocity of the bow shock	50
3.2 Drift instability	52
4. Conclusion	57
<b>4 Foreshock-like Density Cavity in the Magnetotail Reconnection</b>	<b>59</b>
1. Introduction	59
2. Observations	63
2.1 Overview	63
2.2 The reconnection layer structure and the steepened leading boundary of	

the earthward jet	68
2.3 Incident and backstreaming protons inside the cavity	70
2.4 ULF waves in the cavity	77
2.5 Backstreaming electrons in the cavity	80
3 Discussion and conclusion	82
<b>5 Observations of Thin Current Sheet in the Magnetotail</b>	<b>85</b>
1. Introduction	85
2. Observations	87
2.1 Overview	87
2.2 TCS embedding	92
2.3 TCS bifurcation	95
2.4 Flapping motion	98
3. Discussion	102
4. Conclusion	104
<b>Conclusions et perspectives (en français)</b>	<b>107</b>
<b>Conclusions and perspective (in english)</b>	<b>113</b>
<b>References</b>	<b>119</b>

## Résumé

L'environnement spatial proche de la Terre est complexe et divers. La cinétique des ions joue un rôle clé pour comprendre la nature des phénomènes essentiels et des processus physiques prenant place dans le "Géospace". Au moyen de données à haute résolution enregistrées par les quatre satellites Cluster et les deux satellites Double Star, cette thèse étudie la cinétique des ions de faible énergie dans certaines couches frontières essentielles de la magnétosphère terrestre.

Le chapitre 1 donne une brève description générale de l'environnement spatial proche de la Terre et de quelques processus physiques de base tels que la reconnexion du champ magnétique et l'accélération des particules.

Le chapitre 2 introduit, d'abord, la mission Cluster et le projet Double Star et leurs instruments, puis présente en détail les instruments de mesures des ions qui fournissent les données essentielles pour le travail de cette thèse.

Le chapitre 3 décrit une excursion de grande amplitude de la magnétogaine enregistrée simultanément par les satellites Cluster et TC1 de Double Star, évènement survenu pendant une période de champ magnétique interplanétaire dirigé vers le Nord, le 17 mars 2004. La cohérence entre les mouvements de l'onde de choc et de la magnétopause est mise en évidence. En outre, le phénomène de transport du plasma en découlant sous forme de fluctuations de flux en dessous de la gyrofréquence à la magnétopause est décrit et interprété comme la manifestation de l'instabilité de dérive. Les observations corrélées sur l'accumulation de charges et la perturbation du potentiel électrostatique sont fournies par des mesures d'électrons de grandes énergies et le mouvement du vortex éventuel à travers le champ dans l'état non linéaire et l'échange de masse en résultant sont mises en évidence.

Le chapitre 4 présente un nouveau type de cavité de faible densité dans la région de l'écoulement vers l'extérieur de la reconnexion pendant une traversée de la queue magnétique par les satellites Cluster. Elle contient des flux intenses de particules réfléchies alignées au champ magnétique qui sont produites par un mécanisme de

création semblable à celui du préchoc terrestre, et donc présente une morphologie de type préchoc. Dans cette cavité, les flux de protons réfléchis alignés au champ magnétique et les protons avec une distribution de type cône de perte étaient observés simultanément. Des fluctuations du champ magnétique, spécialement les oscillations quasi-monochromatiques, ont été observées. La bordure avant et la frontière du préchoc ionique sont identifiées à partir des observations de la séquence temporelle des observations des protons et du champ magnétique. Juste au-delà de la bordure avant du préchoc ionique, des électrons réfléchis le long du champ magnétique ont été détectés ; leur distribution est du type faisceau suprathermique étroit. Cependant, près du front du choc, des électrons réfléchis du même type de distribution mais avec une forme large, ont été mesurés. Ces deux manifestations différentes des électrons réfléchis montrent les différences dans la physique microscopique du processus de réflexion. De plus, une partie des ions incidents est accélérée plus loin dans la cavité en raison du pompage magnétique qui fournit un autre mécanisme possible dans les processus d'accélération à multi pas dans la reconnexion.

Le chapitre 5 est consacré à l'étude d'un évènement dans la couche de courant mince. Une géométrie simple et la bifurcation de la couche de courant mince ont été toutes les deux observées pendant un passage des satellites Cluster dans la queue magnétique. On a trouvé que l'anisotropie et la nongyrotopie sont responsables des caractéristiques de ce nouvel équilibre qui représente des modifications par rapport au modèle conventionnel d'Harris. Les observations montrent qu'une couche de courant mince à géométrie simple de protons présente une anisotropie de pression dont la composante parallèle au champ magnétique est plus grande que la composante perpendiculaire alors qu'une couche de courant mince d'ions oxygène, avec bifurcation, présente, au contraire, une anisotropie de pression, dont la composante parallèle au champ magnétique est plus petite que la composante perpendiculaire. Le mouvement de battement local de la couche de plasma mince a aussi été observé et quelques caractéristiques particulières telles que le comportement comme une onde solitaire et le mouvement d'oscillations (« kink ») dans le plan perpendiculaire à la

direction Soleil-Terre ont été mises en évidence.

A la fin sont présentées quelques conclusions générales et des perspectives. Le rôle dominant joué par la cinétique des particules dans les formations de ces structures de plasma à petite échelle et les caractéristiques des processus de couplage à différentes échelles y sont résumés.

## Abstract

The near-Earth space environment is complex and diverse. Ion kinetics plays a key role in understanding the nature of key phenomena and physical processes taking place in the Geospace. By means of the high-resolution data recorded by the multiple-point Cluster and Double star spacecraft, the present thesis investigated low energy ion kinetics in some crucial boundary layers of the terrestrial magnetosphere.

Chapter 1 gives a brief overview of the near-Earth space environment and some basic physical processes such as magnetic field reconnection and particle acceleration.

Chapter 2 first introduces the Cluster mission and the Double Star Project and their instrumentations, then presents in detail the hot ion instruments, which provide the crucial data for our work in the present thesis.

Chapter 3 reports a large-amplitude excursion of the magnetosheath recorded simultaneously by the Cluster and TC-1 spacecraft, which occurred during a period of northward interplanetary magnetic field on March 17, 2004. The coherence between the motions of bow shock and magnetopause is revealed. In addition, the relevant plasma transport phenomenon in the form of flux fluctuations below the ion gyrofrequency at the magnetopause is described and interpreted as manifestation of the drift instability. Correlated observations on charge accumulation and electrostatic potential perturbation are provided by electron measurements in high energy regime, and also the eventual cross-field vortex motion in the nonlinear stage and the consequential mass exchange are exhibited.

Chapter 4 presents a novel kind of density depleted cavity in the outflow region of reconnection during a Cluster spacecraft crossing of the magnetotail. It contains intense reflected field-aligned particles, which are produced by a generation mechanism similar to that of the terrestrial foreshock, and hence manifests a foreshock-like morphology. In this cavity, reflected field-aligned proton beams and the protons with a loss-cone distribution were observed simultaneously. Magnetic field fluctuations, especially quasi-monochromatic oscillations, were recorded. Both

the leading edge and the ULF wave boundary of the ion foreshock are identified from the time sequence of proton and magnetic field observations. Just upstream of the leading edge of the ion foreshock, reflected field-aligned electrons were detected, whose distribution has a narrow bump-on-tail pattern. However, close to the shock front, reflected electrons with a broad bump-on-tail pattern was measured. These two different manifestations of reflected electrons reveal the differences in their microscopic physics of the reflecting process. Moreover, a part of incident ions was further accelerated in the cavity due to a Fermi-type acceleration as well as a magnetic pumping which provide another possible mechanisms in the multi-step acceleration processes in reconnection.

Chapter 5 is devoted to an event of thin current sheet. Both embedding and bifurcation of the thin current sheet were observed during a Cluster spacecraft crossing of the magnetotail. It is found that the ion anisotropy and nongyrotropy are responsible for those new equilibrium features that represent deviations from the conventional Harris model. The observations show that an embedded proton thin current sheet manifests a pressure anisotropy, whose component parallel to magnetic field is larger than the perpendicular component; while a bifurcated oxygen ion thin current sheet exhibits a pressure anisotropy, whose component parallel to magnetic field is smaller than the perpendicular component on the contrary. The local flapping motion of the thin current sheet was also observed, and some particular features such as the solitary wave-like behavior and the kink motion in the plane perpendicular to the Sun-Earth direction were revealed.

Finally, some general conclusions and perspectives are given. The dominating roles played by the particle kinetics in the formations of those small-scale plasma structures and the feature of cross-scale coupling processes are summarized.



## **Introduction**

La magnétosphère terrestre est une région de l'espace dont la forme est déterminée par le champ magnétique interne de la Terre, le plasma du vent solaire et le champ magnétique interplanétaire. Elle consiste en plusieurs régions telles que la magnétogaine, les lobes de la queue, la couche de plasma, le courant annulaire et la plasmasphère. Ces régions sont réunies par des frontières telles que la magnétopause, le cornet polaire, la couche frontière de la couche de plasma et la couche de courant de la queue magnétique.

La magnétopause est la frontière entre le champ magnétique terrestre et le vent solaire. La reconnexion magnétique peut y prendre place et conduire au transport de masse, de quantité de mouvement et d'énergie depuis le vent solaire jusqu'à l'intérieur de la magnétosphère. La reconnexion magnétique est le paradigme de base du couplage vent solaire-magnétosphère. Quand le champ magnétique interplanétaire est dirigé vers le sud et antiparallèle au champ magnétique terrestre, les deux champs magnétiques peuvent se connecter à la magnétopause du côté jour et le transport en résultant du flux magnétique aux lobes de la queue peut augmenter la tension magnétique dans cette région.

Les orages et sous-orages sont les principales caractéristiques dynamiques de la magnétosphère, initiées par les interactions de la magnétosphère avec le vent solaire. Les orages dans l'environnement terrestre ont des échelles de temps en jours et sont associés avec les augmentations du courant annulaire dans la magnétosphère interne. Les sous-orages ont des durées de l'ordre de une à trois heures et sont liés aux processus plasma dans la queue magnétique. La caractéristique la plus significative de la magnétosphère est sa réponse globale aux activités géomagnétiques, qui impliquent un certain nombre de processus physiques couvrant une large gamme d'échelles spatiales et temporelles et ainsi révèle la nature fortement couplée des différents processus dans les différentes régions de la magnétosphère. Les phénomènes observés à grande échelle ont leur origine de processus physiques à microéchelle survenant

dans les couches frontières de la magnétosphère. Le couplage à différentes échelles dans la magnétosphère provient de la non linéarité du plasma et du champ électromagnétique et par conséquent la tenue multiéchelle en est une caractéristique inhérente. La magnétosphère présente donc des caractéristiques multiéchelles sur une large gamme d'échelles spatio-temporelle, allant des plus petites échelles des processus cinétiques à l'échelle globale des phénomènes magnétohydrodynamiques.

L'énergie du champ magnétique stockée dans la queue magnétique est dissipée de manière explosive; accompagnée par des manifestations telles que l'augmentation des courants alignés au champ magnétique, l'accélération de particules et des flux de plasma rapides. La couche mince de courant dans la queue magnétique est une région clé où les processus responsables de la montée de l'émission explosive de l'énergie se produisent. Bien que les processus de plasma dans ces couches de courant sont cinétiques en nature, avec des échelles aussi courtes que le rayon de giration électronique, le fort couplage multiéchelle conduit aux caractéristiques globales de la magnétosphère, telles que la formation de plasmoides et leur émission. Dans la queue magnétique, les processus à microéchelles, survenant sur des échelles de l'ordre du rayon de giration des électrons ou des ions, ont des échelles de temps correspondant inférieures à quelques secondes. D'autre part, les processus à grandes échelles, qui peuvent être décrits typiquement par des modèles globaux MHD, ont des échelles de temps supérieures à des dizaines de minutes. Entre ces deux échelles il y a un certain nombre de processus à meso-échelles, dont les dimensions spatiales sont de quelques rayons terrestres et les échelles de temps typiques sont de plusieurs minutes.

Les phénomènes magnétosphériques multiéchelles sont dus à la nonlinéarité inhérente au plasma et au champ électromagnétique et sa nature est hors équilibre. Les champs complexes et les populations de plasma avec des longueurs d'échelle très petites rendent difficiles les mesures in-situ aussi bien que les analyses théoriques. Un seul satellite mesure les séries temporelles de paramètres physiques telles que vues à la position du satellite. Ainsi ces mesures ne peuvent pas séparer sans ambiguïté les variations spatiales et temporelles. L'étude de la structure et de l'évolution des

processus physiques clés demande donc une approche multipoints.

La mission Cluster, lancée en juillet 2000; consiste en quatre satellites identiques volant en formation tétraédrique. Les orbites individuelles des satellites Cluster sont telles que dans les régions clés de l'environnement spatial de la Terre, telles que l'onde de choc, la magnétopause, la queue magnétique ou la zone aurorale, les quatre satellites conservent des séparations à peu près constantes, l'échelle pouvant être ajustée pendant les différentes phases de la mission de quelques dizaines de kilomètres à un rayon terrestre.

Le programme Double Star (DSP) est une mission spatiale de l'Agence Spatiale Chinoise (China National Space Administration) et de l'Agence Spatiale Européenne. DSP comporte un satellite équatorial et un satellite polaire. Le but principal de DSP est d'étudier la réponse globale de la magnétosphère aux orages géomagnétiques et aux sous-orages. En liaison avec Cluster, les deux missions permettent d'observer simultanément la magnétosphère terrestre en six points de l'espace.

Des mesures simultanées à quatre points ou à six points permettent pour la première fois de séparer les variations temporelles et spatiales et d'étudier les petites structures à trois dimensions dans l'environnement plasma de la terre. Elles fournissent une excellente occasion d'étudier de façon détaillée ces phénomènes à multiéchelles et les processus de couplage multiéchelles dans la magnétosphère.

## **Introduction**

The Earth's magnetosphere is a region in space whose shape is determined by the Earth's internal magnetic field, the solar wind plasma, and the interplanetary magnetic field. It consists of several main regions such as magnetosheath, tail lobes, plasma sheet, ring current and plasmasphere. These regions are joined through boundaries such as the magnetopause, cusp, plasma sheet boundary layer and magnetotail current sheet.

The magnetopause is the boundary between the Earth's magnetic field and the solar wind. Magnetic reconnection can take place there and lead to the transport of mass, momentum and energy from the solar wind into the magnetosphere. Magnetic reconnection is the basic paradigm of the solar wind-magnetosphere coupling. When the interplanetary magnetic field is southward and anti-parallel to the Earth's magnetic field, the two magnetic fields may connect at the dayside magnetopause and the resulting transport of magnetic flux to the tail lobes causes increased magnetic stress in that region.

Storms and substorms are the main dynamic features of the magnetosphere, initiated by interactions between the magnetosphere with the solar wind. The geospace storms have time scales of days and are associated with enhancements of the ring current in the inner magnetosphere. The substorms on the other hand have a characteristic period of the order of one to three hours and are linked to the plasma processes in the magnetotail. The most significant feature of the magnetosphere is its global response to geomagnetic activities, which involves a number of physical processes covering over a wide range of spatial and temporal scales and thus reveals the strongly coupled nature of different processes in the different regions of the magnetosphere. The observed large scale phenomena are believed to originate from the microscale physical processes occurring at the boundary layers of the magnetosphere. The cross-scale coupling in the magnetosphere arises due to the nonlinearity of plasma and electromagnetic field and consequently the multiscale behavior is an inherent feature.

Therefore, the magnetosphere exhibits multiscale features over a wide range of spatio-temporal scales, ranging from the smallest scale of kinetic processes to the global scale of magnetohydrodynamic phenomena.

The stored magnetic field energy in the magnetotail is released in an explosive manner, accompanied by manifestations such as enhanced field-aligned currents, particle acceleration, and fast plasma flows. Thin current sheet in the magnetotail is a key region where the processes responsible for the onset of explosive release of energy take place. Although the plasma processes in these current sheets are kinetic in nature, with scale sizes as short as the electron gyroradius, the strong cross-scale coupling drives more global magnetospheric features, such as plasmoid formation and release. In the magnetotail, microscale processes, occurring on the electron or ion gyroradius scales, have corresponding time scales of less than a few seconds. On the other hand, large-scale processes, which can be described typically by global MHD models, have time scales longer than tens of minutes. Between these two scales there is a number of processes in meso-scale, whose spatial sizes are at a few Earth radii and typical time scales are of several minutes.

The magnetospheric multiscale phenomena are due to the inherent nonlinearity of the plasma and electromagnetic field, and its non-equilibrium nature. The complex fields and plasma populations with wide variety of scales make in-situ measurements as well as theoretical analysis difficult. Single spacecraft measure the time series of physical parameters as seen at the spacecraft position. As such, these measurements cannot unambiguously separate spatial and temporal variability. The study of the structure and evolution of key physical processes therefore requires a multi-point approach.

The Cluster mission, launched in July 2000, consists of four identical satellites flying in a tetrahedral formation. The individual orbits of Cluster spacecraft are arranged so that in key geospace regions, such as the bow shock, the magnetopause, the magnetotail, or the auroral zone, the four spacecraft maintain an approximately constant separation, the scale of which can be adjusted during different mission

phases from tens of km to  $1 R_E$  .

The Double Star Program is a joint space mission between the China National Space Administration and the European Space Agency. The DSP consists of one equatorial satellite and one polar satellite. The main goal of DSP is to investigate the magnetospheric global response to the geomagnetic storms and substorms. In conjunction with the Cluster mission, the two missions allow simultaneous observations of the Earth magnetosphere at six points in space.

Simultaneous four-point or six-point measurements allow for the first time to separate spatial from temporal variations and to investigate the three-dimensional small scale structures in the Earth's plasma environment. They provide an excellent opportunity for detailed investigation of those multiscale phenomena and cross-scale coupling processes in the magnetosphere.

## Chapter 1

### The magnetosphere

#### 1. Introduction

The Earth's magnetosphere is a region in outer space, which is filled with free ions and electrons from both the solar wind and the Earth's ionosphere. It is a complex system whose structure and behavior is controlled by two factors. The first is the terrestrial magnetic field, supposed to be generated via dynamo effect by currents flowing in the Earth's core. Outside the Earth this field has the form of a dipole field in first approximation, aligned approximately with the Earth's spin axis. The second factor is the solar wind, a fully ionized plasma that streams continuously outward from the Sun into the solar system at speeds of about 300–800 kilometers per second and carries a large-scale interplanetary magnetic field (IMF). The boundary of the magnetosphere on the dayside is ellipsoidal, at a distance of about 10-15  $R_E$  to the Earth; while on the night side it approaches roughly a cylinder with a radius 20-25  $R_E$  due to the compression of solar wind plasma. The tail region stretches well past 200  $R_E$ . A overall schematic view of the magnetosphere is shown in Fig 1.1 (Kivelson and Russell, 1995).

#### 2. The bow shock and the magnetosheath

When an object or disturbance moves faster than the information about it can be propagated into the surrounding medium, medium near the disturbance cannot react or get out of the way before the disturbance arrives. Hence a compressed front forms and is called a shock. Shock waves are characterized by an abrupt, nearly discontinuous change in the characteristics of the medium. Across a shock there is always an

extremely rapid rise in parameters of medium such as pressure, temperature and density.

The solar wind plasma (Parker, 1958) travels usually at speeds up to 200-800km/s, which are faster than any fluid plasma wave relative to the magnetosphere. Therefore a standing shock wave forms around the magnetosphere. The standoff distance of the bow shock is about  $15 R_E$  on the dayside of the Earth.

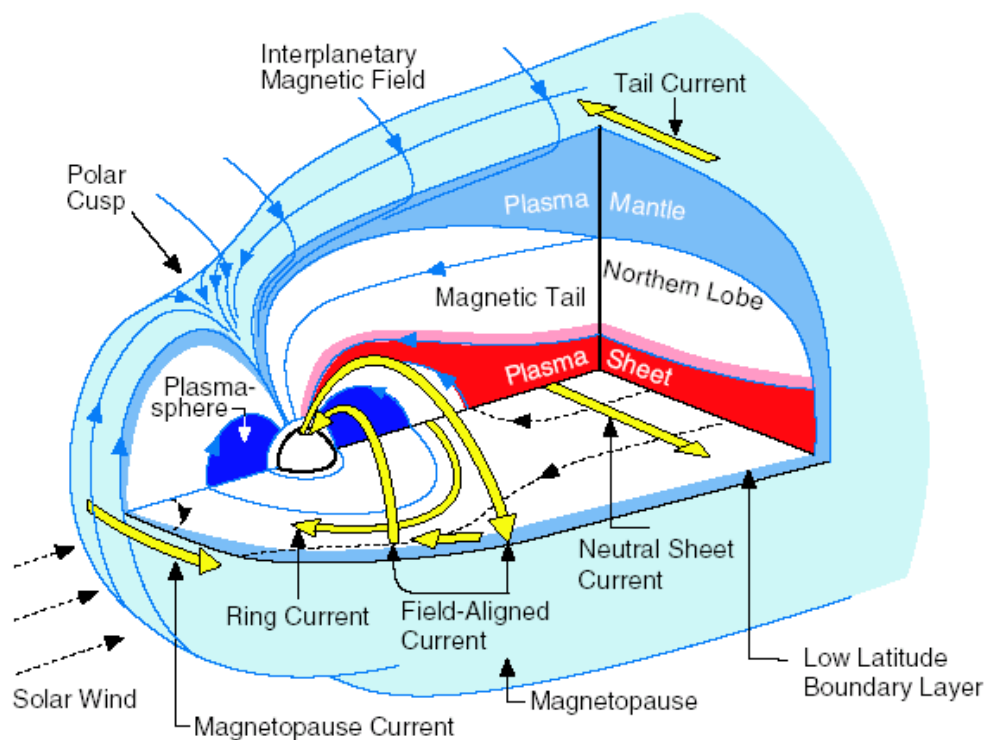


Fig.1.1 Three-dimensional schematic of the magnetosphere (Kivelson and Russell, 1995).

In a viewpoint of magnetohydrodynamics, a shock is treated as a discontinuity, i.e., the thickness of its transition layer is regarded as zero. In this approximation, conservation of mass, momentum, and energy, together with the Maxwell equations lead to a set of relations between the upstream and the downstream quantities, known as the Rankine - Hugoniot jump relations. The magnetohydrodynamic problem is

more complicated than the corresponding gas dynamic problem because the magnetized plasma supports three independent magnetoacoustic wave modes: fast wave, slow wave and the intermediate wave. The bow shock is a fast shock.

The properties of collisionless plasma shock waves depend primarily on two parameters. One is the Mach number of the shock wave, the ratio of upstream velocity to Alfvén speed, which is  $V_A = B_0 / \sqrt{\mu\rho}$ , where  $B_0$  is the magnetic field strength,  $\rho$  is the fluid density, and  $\mu$  is the magnetic permeability (in meter-kilogram-second units); for the terrestrial bow shock this is usually in the range from  $\sim 3$  up to 10. The second is the propagation angle, or the angle between the upstream magnetic field and the normal to the shock surface. Across the surface of the bow shock, this angle ranges from  $90^\circ$  to  $0^\circ$ , i.e. from quasi-perpendicular to quasi-parallel. For a quasi-parallel shock, the particles escape upstream from the shock relatively easy, gyrating along the field lines. The region of space upstream of the bow shock, magnetically connected to the shock and filled with particles backstreaming from the shock is known as the foreshock (Eastwood et al., 2005).

It is not directly the solar wind plasma which constitutes the boundary of the magnetosphere but the strongly heated and compressed plasma behind the bow shock, which is called the magnetosheath. The magnetosheath is formed mainly from decelerated and deflected solar wind, with a small contribution of plasma from the magnetosphere. Because the nature of the bow shock depends on the orientation of the interplanetary magnetic field with respect to the local bow shock normal, the properties of the magnetosheath plasma just behind the bow shock depend also on whether the shock is quasi-perpendicular or quasi-parallel. In general, the magnetosheath tends to be in a more turbulent state behind the spatially extended quasi-parallel bow shock than it is behind the quasiperpendicular shock.

Inside the magnetosheath, the direction of the magnetic field changes from parallel with the IMF in the outer region to drape around the blunt inner boundary, which is called the magnetopause. Meanwhile, the average flow direction deviates from the

direction along the Sun-Earth line such that the plasma flows around the magnetopause. The velocity downstream of the bow shock is subsonic; but it increases again to supersonic speeds around the magnetopause flanks. In addition, the magnetosheath plasma develops a pronounced temperature anisotropy behind the bow shock that increases toward the magnetopause and is more pronounced in the ions than in the electrons.

### 3. The magnetopause

The existence of magnetopause (Chapman and Ferraro, 1931), the inner boundary of the magnetosheath, is a direct consequence of solar wind interaction with a magnetized planet. It is formed at a distance where the solar wind dynamic pressure equals the magnetic pressure of Earth's field. At this location, typically around 8 - 11  $R_E$  away on the Earth - Sun line on the dayside, the Earth's intrinsic dipolar magnetic field is separated from the ambient magnetosheath field. Ampere's law then tells us that a sheet of electrical current, which is called the Chapman-Ferraro current, must develop to cancel the Earth's field outside.

The magnetopause is constantly in motion. Observations from ISEE spacecraft indicate that the velocity of magnetopause motion is quite variable ranging from about 3 to over 40 km/s and typically being about 20 km/s. The motion of the magnetopause seems to be driven by pressure fluctuations in the solar wind or the Kelvin- Helmholtz instability.

Classical theory of interaction between the solar wind and the magnetosphere predicts the magnetopause to be an impenetrable boundary separating cold plasmas on magnetosheath magnetic field lines from hot tenuous plasmas on magnetospheric magnetic field lines. But in fact, observations indicate that a boundary layer of magnetosheath-like plasmas can be found just inside all regions of the magnetopause. These observations are evidence for the entry of magnetosheath plasma into the magnetosphere. A wide variety of processes, including magnetic reconnection, finite

Larmor radius effects, diffusion due to resonant interaction of ions with plasma waves, the Kelvin-Helmholtz instability and impulsive penetration, have been proposed to account for the transfer of solar wind mass into the magnetosphere, and the escape of magnetospheric particles into the magnetosheath.

#### 4. The magnetotail

In contrast to the dayside magnetosphere, which is compressed and confined by the solar wind and is shaped like a paraboloid of revolution with the apex towards the Sun, the nightside is stretched out into a long tail. In the nightside region, magnetic field lines emanating from polar latitudes are stretched away anti-sunwards to form a long ( $>1000 R_E$ ) cylindrical volume of field lines. This region constitutes the magnetotail. The tail radius increases with downstream distance, e.g. about  $25 R_E$  at a downstream distance of  $30 - 50 R_E$ .

Early observations revealed the internal structure of the magnetotail. Most of the volume of the magnetotail is taken up by two large bundles of nearly parallel magnetic field lines, known as the "tail lobes". The bundle north of the equator points earthwards and connects to the north polar region. The southern lobe contains antisunward field lines, connecting to the southern polar cap linking to the southern polar region. The magnetotail lobes are separated by a region of weaker, and more variable magnetic field and hotter plasma, which is centered on the equator and typically 2-6 Earth radii thick and called the plasma sheet. Across this high plasma regime, the magnetic field undergoes a transition from earthward to tailward. This directional change takes place within a section of the plasma sheet limited in north-south extent where a sheet current, known as the cross-tail current, flows in the dawn to dusk direction. The region in the centre of the plasma sheet, where  $B_x$  changes sign, is frequently called the 'neutral sheet'. The plasma sheet and the embedded current-sheet extend at least to  $60 R_E$ .

In addition to the lobe and the plasma sheet, several boundary regimes have been

identified in the magnetotail. At the boundary between the magnetosheath and the tail lobe there is the plasma mantle in high latitudes and the low latitude boundary layer. The plasma mantle is the part of the lobe into which cold plasma of the solar wind has been introduced. The low latitude boundary layer is the low latitude region where the solar wind and the hot tail plasma are seen as a mixture. The plasma sheet boundary layer is a boundary region between the plasma sheet and the lobe.

The solar wind and the Earth's ionosphere are potential sources of magnetotail plasmas. Both of them have their own assets; the solar wind plasma is closer to the tail plasma in energy, while the ionospheric plasma is abundant. The solar wind has generally been taken as the major source, but it has been argued that the ionosphere could provide enough plasma to the tail. Entry of the solar wind plasma into the mantle has been confirmed by continuity of the plasma characteristics across the magnetosheath-tail boundary; in the energy-time spectrograms of the ions it is often observed that a band representing a plasma population continues smoothly from the magnetosheath to the mantle. Both density and flow speed in the mantle are seen to decrease with increasing separation from the boundary region. The oxygen ion beam tends to be observed in the mantle during geomagnetically active times. At such times field lines and plasma move equatorward in the tail lobe. The ionospheric ions could be carried quite significantly equatorward by this convection while they flow tailward along field lines to the distant tail.

The magnetotail is quite dynamic, a wide variety of energy conversion processes between magnetic field and plasma can take place there. Of its many dynamic features, perhaps the most important and basic is the so-called magnetospheric substorm (Akasofu, 1981), a period of the order of one to three hours, during which energy is rapidly released in the magnetotail.

The entire substorm process involves a growth phase, expansion phase, and recovery phase. The first stage of substorm dynamics is called the growth phase, which is characterised with equatorward shifting of the boundaries of the auroral oval after southward IMF turning. During the growth phase the polar cap region expands

equatorward, the auroral oval shrinks in width, and the nightside magnetic field lines are stretched. The onset of the expansion phase is an extremely fast, whose typical temporal scale is tens of seconds or even less. The manifestation of expansion phase is characterized by a localized brightening of auroral arc and a localized turbulent disturbance in the near-Earth plasma sheet equatorial region, e.g., the dipolarization of the magnetic field topology in the inner central plasma sheet, the energization of sheet particles, and the magnetic signatures of the enhanced ionospheric currents. The expansion phase of substorm occurs for any IMF orientation but it is most intense during southward IMF created main phase of magnetic storm. The expansion phase persists minutes to tens of minutes, after which the system returns to a less disturbed state during the recovery phase which persists tens of minutes. The global geomagnetic field depression weakens and the auroral oval contracts after the IMF turns northward during the recovery phase.

The complete substorm process reflects a dynamical sequence of energy storage and release in the magnetotail. The growth phase is a period of enhanced energy storage in the magnetotail. Due to the equatorward compression and tailward stretching of the magnetic field lines, a large amount of magnetic energy is stored in the plasma sheet. During the expansion phase, the reserved magnetic energy releases dramatically and converts into plasma kinetic energy to excite a wide variety of plasma turbulences. These turbulences spread in the plasma sheet, redistribute and energize the plasma, causing the crosstail current density to be reduced as well as the magnetic field to dipolarize in the central plasma sheet. Eventually, after the turbulence level decreases, the plasma sheet and the ionosphere recover to a less disturbed state during the recovery phase.

## 5. Magnetic reconnection

Magnetic reconnection, an ubiquitous phenomenon in plasma physics, is essentially a topological restructuring of a magnetic field caused by a change in the connectivity of

its field lines. Breaking and reconnecting the field lines in a plasma allows the release of stored magnetic energy, that is, conversion of magnetic energy to plasma kinetic and thermal energy. Magnetic reconnection plays a key role in wide range of phenomena in the universe, relaxation events of fusion plasmas, the dynamics of the Earth's magnetosphere, the evolution of solar and stellar flares, and the formation process of stars. On a solar scale, reconnection is thought to be responsible for solar flares and coronal mass ejections. The auroras are also generally considered to be related to reconnection events in the Earth's magnetosphere. Tokamaks and other laboratory setups with plasmas display irrefutable evidence of reconnection.

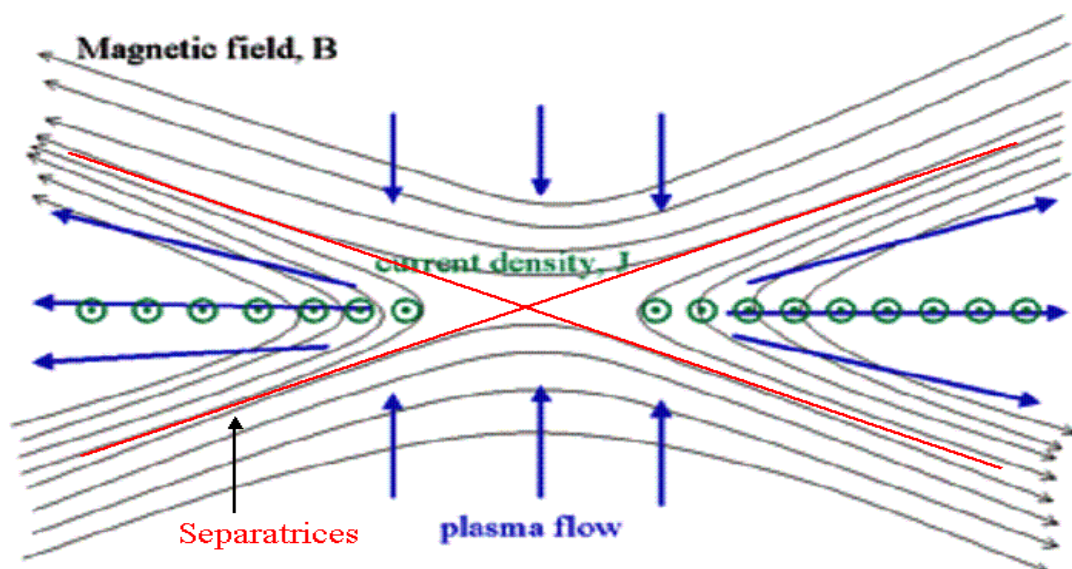


Fig.1.2 Schematic illustration of magnetic reconnection.

In a plasma, magnetic field lines are frozen to field lines that are topologically distinct from other field lines nearby. This topology is approximately preserved even when the magnetic field itself is strongly distorted by the presence of variable currents or motion of magnetic sources. The structure of reconnection layer is shown in Fig 1.2. Four separate magnetic domains in a magnetic plasma are separated by two separatrix

surfaces: curved surfaces in space that divide different bundles of flux. Field lines on one side of the separatrix all terminate at a particular magnetic pole, while field lines on the other side all terminate at a different pole of similar sign. The intersection of the separatrices forms a separator at the center. Field lines in association with plasma flow inward from above and below the separator, reconnect, and spring outward horizontally.

The separator is called diffusion region where the frozen-in condition breaks down. According to resistive MHD theory, reconnection happens because the resistivity of the current layer allows magnetic flux from either side to diffuse through the current layer, cancelling out flux from the other side of the boundary. When this happens, the plasma is pulled out by magnetic tension along the direction of the magnetic field lines.

Classical reconnection theory relies on magnetohydrodynamics to model plasma dynamics. Magnetohydrodynamics is a single fluid theory, meaning that it describes a plasma which is electrically neutral (i.e. containing a macroscopically equal density of positive and negative charge carriers). It is applicable only in this macroscopic limit. Reconnection has been described by MHD theory for most of its history. The classical models, however, struggle to provide energy release of the correct magnitude on the right time scales. The first serious mechanism was developed by Sweet and Parker (Sweet, 1958; Parker, 1957). In the Sweet-Parker model of reconnection, magnetic field reconnects in a diffusion region with a length corresponding to the total system size. The reconnection rate is defined as the Alfvén Mach-number in the inflow region. This rate is far too small to explain observed phenomena such as those on solar scales. Therefore, Petschek (1964) proposed a model which requires an external field and shock formation. In the Petschek model, the diffusion region is much shorter than the overall size and that the outer region contains two pairs of standing slow mode shocks. These shocks deflect and accelerate the incoming plasma into two exit jets wedged between the shocks: acceleration is due to the Maxwell stress at the slow mode shocks. The maximum reconnection rate much larger than the Sweet-Parker rate and typically

of the order 0.1.

The Petschek rate is very controversial, and experiments suggest that it is applicable only when resistivity is non-constant. Reasons for this are not known. Many scientists consider the Sweet-Parker rate to be the maximum allowed by MHD. Use of anomalous resistivity models also allows reasonable reconnection rates to be achieved. The reason is that in the reconnection region particles are undergoing more turbulence, collisions, etc. and resistivity may increase there. A good theoretical understanding of this is not available, although there is some experimental evidence that it may be a real effect.

While MHD provides the framework for the classical models described above, it may break down on the small scales at which reconnection occurs. Ion and electron motions decouple in this regime, with the electron flow rate becoming much greater than the ion rate and driving so-called whistler waves, which are dispersive. This electron driven mechanism gives a much faster reconnection rate. Whistler driven reconnection creates a strong out-of-plane magnetic field, which has been observed in Earth's magnetosphere.

In the recent years, computational advances have allowed simulation of three dimensional reconnection events. This was a great advance over two dimensional theories, which fail to capture many of the subtleties present in real reconnection processes. Plasma physics is an often controversial field, possibly due to its complexity, and debates over mechanisms for reconnection are far from settled.

A crucial problem is that observed reconnection happens much faster than predicted by MHD theory. Classical reconnection theories require the poorly understood assumption of anomalous resistivity in order to achieve physically reasonable time scales. Although some models such as turbulent reconnection and Hall MHD have claimed to solve this puzzle, the triggering mechanism of fast reconnection and size of the diffusion region are still controversial. Generally speaking, magnetic reconnection is still poorly understood, making it one of the most important problems in plasma physics today.

## Chapter 2

### Instrumentation

#### 1. The Cluster mission

The Cluster mission (Escoubet et al., 1997) is a European Space Agency space mission (cooperation with NASA) to study the Earth magnetosphere and the near-Earth solar wind. Simultaneous multi-point measurements allow for the first time to separate spatial from temporal variations and to investigate the three-dimensional small scale structures in the Earth's plasma environment.

The Cluster mission was first proposed in 1982. Though the original Cluster spacecraft were completed in 1995, the explosion of the rocket carrying the satellites in 1996 delayed the mission. In April 1997, the ESA Science Programme Committee approved the recovery mission.

On 16 July 2000, a Soyuz-Fregat rocket launched two of the Clusters into an orbit between 25000 and 125000 km with a period of 57 hours. Three weeks later on 9 August 2000 another Soyuz-Fregat rocket lifted the remaining two Cluster spacecraft into similar orbits. Due to the slightly different orbital parameters, the spacecraft form a tetrahedron with a characteristic size which can be varied from 200km to 20000 km, according to the key scientific regions.

Each satellite carries a scientific payload of 11 instruments designed to study the small-scale plasma structures in space and time in the key plasma regions: the solar wind and bow shock, magnetopause, polar cusps, magnetotail and the auroral zone.

The FluxGate Magnetometer (FGM) (Balogh et al., 2001) and the Electron Drift Instrument (EDI) (Paschmann et al., 1997) are dedicated to measure the magnetic and electric field. The Wave Experiment Consortium (WEC) (Pedersen et al., 1997) employs five experiments which investigate plasma waves: the Spatio-Temporal

Analysis of Field Fluctuation experiment (STAFF) (Cornilleau-Wehrin et al., 1997), the Electric Field and Wave experiment (EFW), the Waves of High frequency and Sounder for Probing of Electron density by Relaxation (WHISPER) (Décréau et al., 1997) experiment, the Wide Band Data (WBD) (Gurnett et al., 1997) receiver and the Digital Wave Processing (DWP) (Woolliscroft et al., 1997). The measurement for particles is executed by the Cluster Ion Spectroscopy (CIS) (Rème et al., 1997, 2001) experiment, the Plasma Electron and Current Experiment (PEACE) (Johnstone et al., 1997) and the Particle Imaging Detectors (RAPID) (Wilken et al., 1997) instrument. The Active Spacecraft Potential Control (ASPOC) (Riedler et al., 1997) experiment is responsible for the control and stabilization of the spacecraft electrostatic potential.

## 2. The CIS experiment

The prime scientific objective of the CIS experiment is the study of the dynamics of magnetized plasma structures in and in the vicinity of the Earth's magnetosphere, with the determination, as accurately as possible of the local orientation and the state of motion of the plasma structures required for macrophysics and microphysics studies. To achieve the scientific objectives, the CIS instrumentation has been designed to satisfy the following criteria, simultaneously on the 4 spacecraft:

- a. Provide a uniform coverage of ions over the entire  $4\pi$  steradian solid angle with good angular resolution.
- b. Separate the major ion species from the solar wind and ionosphere.
- c. Have high sensitivity and large dynamic range to support high-time-resolution measurements over the wide range of plasma conditions.
- d. Have the ability to routinely generate on-board the fundamental plasma parameters for major ion species and with one spacecraft spin time resolution (4 seconds).
- e. Cover a wide range of energies, from spacecraft potential to about 40 keV/e.
- f. Have versatile and easily programmable operating modes and data-processing routines to optimize the data collection for specific scientific studies and widely

varying plasma regimes.

To satisfy all these criteria, the CIS package consists of two different instruments (Fig. 2.1): a Hot Ion Analyser (HIA) sensor and a time-of-flight ion COmposition and DIstribution Function (CODIF) sensor. The CIS plasma package is capable of measuring both the cold and hot ions of Maxwellian and non-Maxwellian populations from the solar wind, the magnetosheath, and the magnetosphere with sufficient angular, energy and mass resolutions.

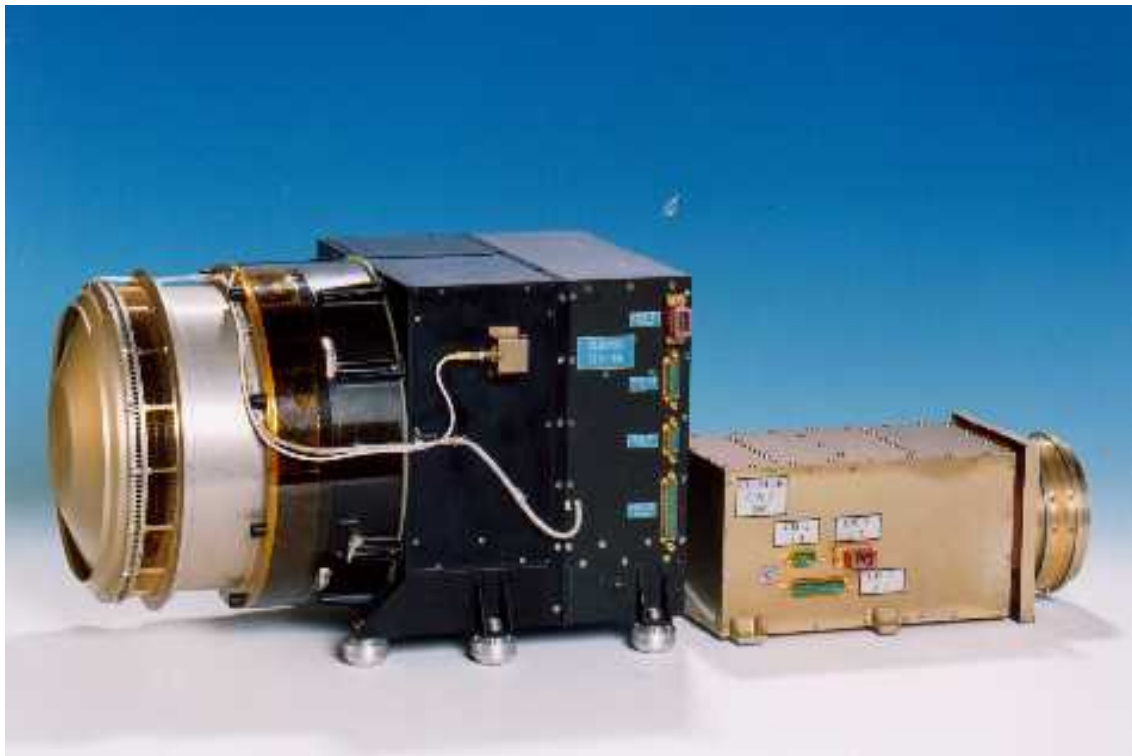


Fig. 2.1 The photo of the CODIF (left) and HIA (right) sensors.

The Hot Ion Analyser (HIA) instrument combines a symmetrical quadrispherical electrostatic analyzer with a fast imaging particle detection system based on microchannel plate (MCP) electron multipliers and position encoding discrete anodes.

Fig.2.2 provides a cross-sectional view of the HIA electrostatic analyser.

The HIA instrument has two  $180^\circ$  field of view sections parallel to the spin axis with two different sensitivities, corresponding respectively to the 'high G' (high geometrical factor) and 'low g' (low geometrical factor) sections. The 'low g' section allows detection of the solar wind and the required high angular resolution is achieved through the use of  $8 \times 5.625^\circ$  central anodes, the remaining 8 sectors having in principle  $11.25^\circ$  resolution; the  $180^\circ$  'high G' section is divided into 16 anodes,  $11.25^\circ$  each. Fig. 2.3 illustrates the principle of the HIA anode sectoring.

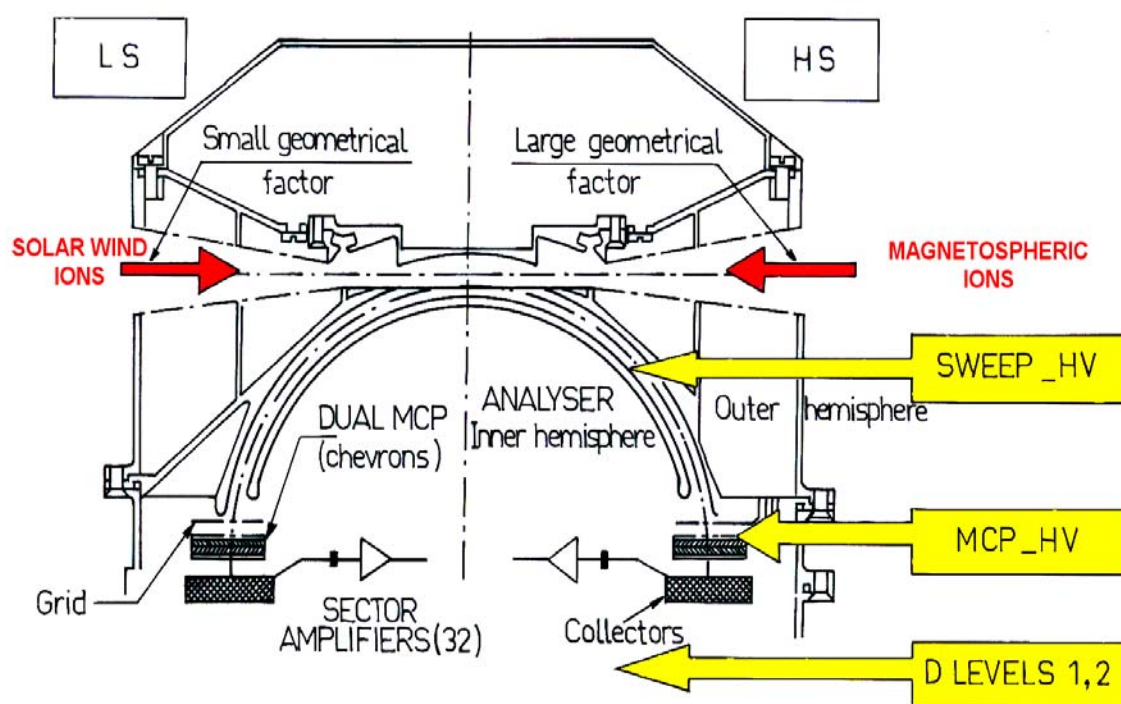


Fig.2.2 Cross-sectional view of the HIA analyser.

The CODIF instrument is a high-sensitivity mass-resolving spectrometer with an instantaneous  $360^\circ \times 8^\circ$  field of view to measure complete 3D distribution functions of the major ion species, within one spin period of the spacecraft. The sensor primarily covers the energy range between 0.02 and 38 keV/charge.

The electrostatic analyser (ESA) has a toroidal geometry, consisting of inner and outer analyser deflectors, a top-hat cover and a collimator. The full angular range of the analyser is divided into 16 channels of  $22.5^\circ$  each. In order to extend the energy range of the CODIF sensor to energies below  $15 \text{ eV/e}$ , a retarding potential analyser assembly is incorporated in the two CODIF apertures (see Fig.2.4). The retarding potential analyser provides a way of selecting low-energy ions at the entrance of the CODIF analyser without requiring the electrostatic analyzer inner deflector to be set accurately near zero Volt.

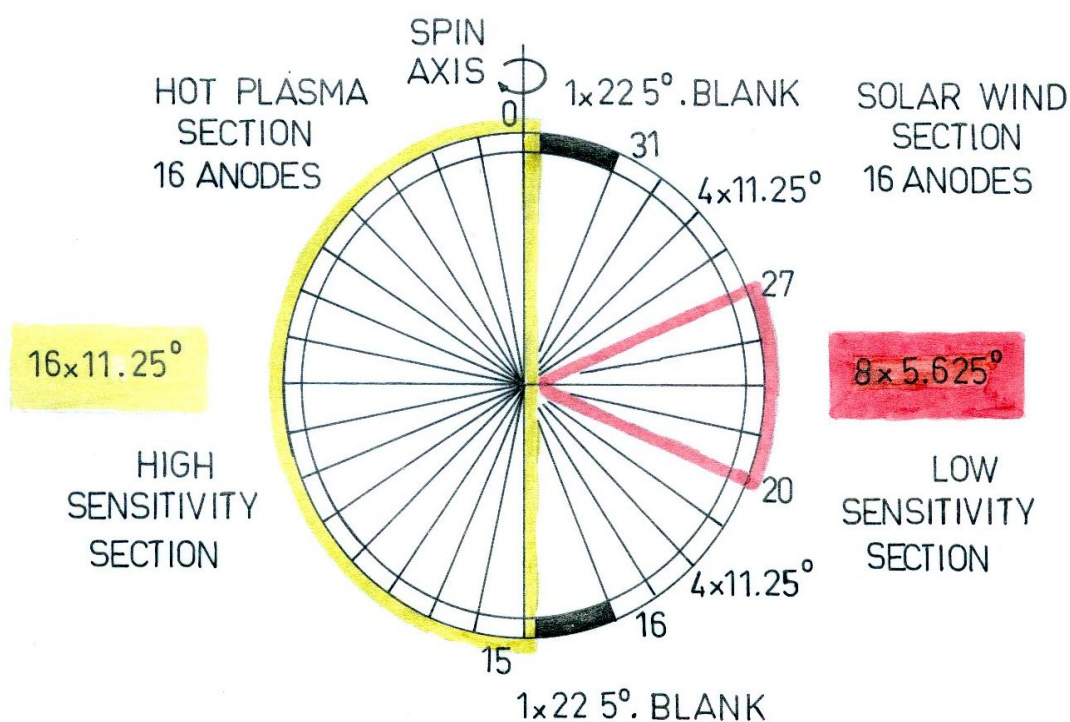


Fig. 2.3. Principle of the HIA anode sectoring.

CODIF uses a time-of-flight spectrometer to resolve the different plasma species. This section lies between the exit from the deflection plates and the solid state detector. In the time-of-flight spectrometer, the velocity of the incoming ions is measured. The

flight path of the ions is defined by the 3 cm distance between the carbon foil at the entrance and the surface of the 'stop' microchannel plate (MCP). The start signal is provided by the secondary electrons emitted from the carbon foil during the passage of the ions. The detection of the ions at the MCP marks the stop time. Knowing the velocity and the energy per charge of the detected ions, their mass per charge can be deduced. Fig.2.4 provides a cross-sectional view of the CODIF sensor.

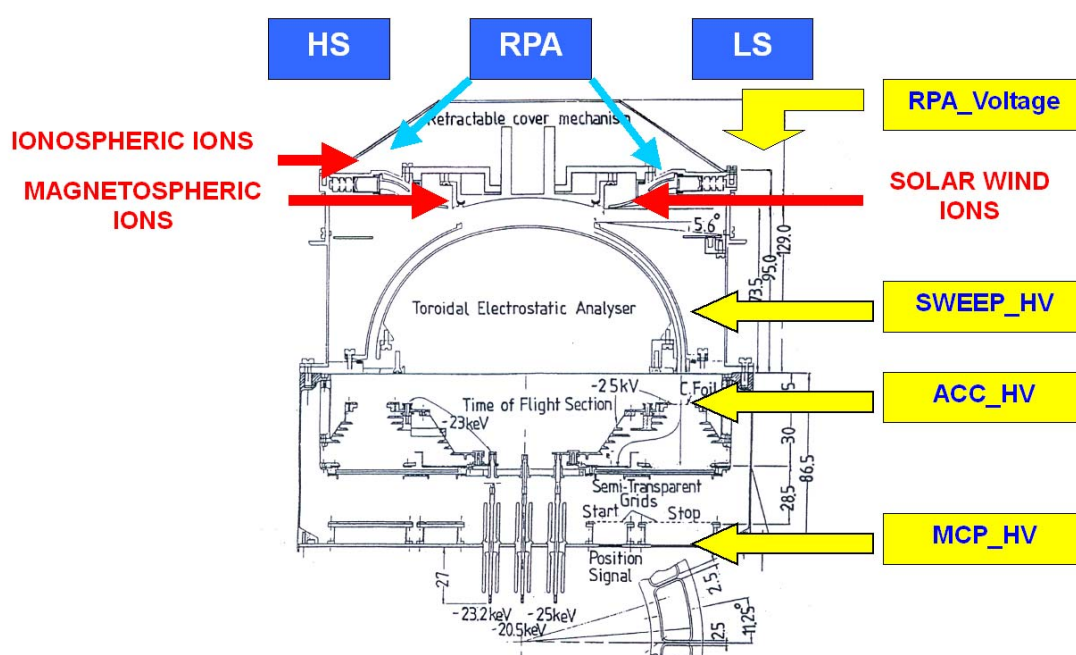


Fig.2.4. Cross-sectional view of the CODIF sensor.

### 3. The fluxgate magnetometer

Many types of magnetometers measure the magnetic field by using the potential difference produced by a change in the magnetic flux. Fluxgate magnetometers are using the variation of the relative permeability with the intensity of the magnetic field to measure static or low frequency magnetic fields. A pick-up coil is wound around two parallel ferromagnetic cores made from high permeability material. The ferromagnetic cores are periodically driven deep in and out saturation by the drive

windings. The strong nonlinear coupling due to core saturation results in harmonics of the driven frequency in the pick-up coil. The amplitude of the even harmonics is proportional to the component of the magnetic field parallel with the cores.

The FGM instrument on each spacecraft of the Cluster mission consists of two triaxial fluxgate magnetic field sensors, one at the end of a 5m long radial boom, and the second 1.5m inboard from the tip of the boom. The sampling of vectors from the magnetometer sensor designated as the primary sensor is carried out at the rate of 201.793 vectors/s. It can also provide measurements with high resolution up to 8 pT.

#### 4. The Double Star Program

Double Star Program (DSP) is the first joint space mission between the China National Space Administration and the European Space Agency. The DSP consists of two satellites: the equatorial satellite of DSP (TC-1) and the polar satellite of DSP (TC-2). The first spacecraft, TC-1 was launched on December 29, 2003, and the second one, TC-2, was launched on July 25, 2004. The TC-1 is at an eccentric equatorial orbit with a  $28^{\circ}$  inclination and an apogee of about  $13.4R_E$  and the TC-2 is at a polar orbit with an apogee of about  $6.0R_E$ . The equatorial satellite of DSP with on-board particle and field instruments detect the physical processes of magnetic storms and magnetospheric substorms in the near-Earth magnetotail, as well as the energy transfer from the solar wind to the magnetosphere via the dayside magnetopause. The polar satellite of DSP, capable of making remote sensing observations as well, detect energy transfer from the solar wind and the near-Earth magnetotail to the polar ionosphere and upper atmosphere, as well as ionized particle transfer from the ionosphere to the magnetosphere.

Each Double Star spacecraft carries eight scientific instruments. Among several European instruments on board this spacecraft, which are identical to those developed for the Cluster spacecraft, the HIA (Hot Ion Analyzer) instrument (Rème et al., 2005) on board the TC-1 spacecraft is an ion spectrometer nearly identical to the HIA sensor

of the CIS instrument on board the 4 Cluster spacecraft. This instrument has been specially adapted for TC-1:

- a. The interface board has been changed.
- b. In order to include radiation shielding, taking into account the orbit of TC-1, the size of the box has been increased by 4mm on each side, on the top and on the rear, and the total mass of the sensor is 3.5 kg.
- c. There is a new interface for telemetry.
- d. The telemetry products have some changes.
- e. There is a new interface for commanding.
- f. The telemetry data rate is 4.44 kbits/s (The rate for Cluster is 5.5 kbits/s).

The HIA instrument onboard the Cluster mission has two sections with two different sensitivities (different geometrical factors), corresponding respectively to the 'high G' and 'low g' sections, where the 'low g' section is designed mainly for solar wind studies. For Double Star the instrument operation is on the "high G" section, since the spacecraft was planned to rarely cross the average (model-predicted) position of the bow shock. However, due to the higher apogee than scheduled of the TC-1 spacecraft, and to the bow shock in/out motion around its average position, the spacecraft frequently gets into the solar wind but stays near the bow shock thanks to its skimming orbit.

There are three Chinese high-energy particle instruments (Cao et al., 2005) on board both TC-1 and TC-2:

- a. The High Energy Electron Detectors (HEED) measure high energy electrons in the range of 200 keV to 10MeV.
- b. The High Energy Proton Detectors (HEPD) measure high energy protons in the energy range 3MeV to 400 MeV.
- c. The Hot Ion Detectors (HID) measure high energy heavy ions in the energy range 10MeV (He) to 8 GeV (Fe) with atomic numbers from 2 (He) to 26 (Fe).

The Low Energy Ion Detector (LEID) is mounted only on the polar orbit satellite and is used to measure energy spectrum, the 3-D velocity distribution function and the

differential flux of low energy ions. The working principle and hardware design of LEID are almost identical to that of HIA on board the Cluster. However, the software of LEID is different from that of HIA. On board TC-2, LEID does not perform any processing of the raw data, and the complete ion distribution functions are sent into the telemetry. Thus, the time resolution of LEID is only 12 s (3 times the satellite spin period) due to the telemetry limitation. LEID only produces the 3-D velocity distribution function for the first spin period of each 12-s interval.



## Chapter 3

# Magnetosheath excursion and transport process at the magnetopause

### 1. Introduction

The shape and location of the bow shock and magnetopause are very sensitive to the solar wind conditions, especially the solar wind kinetic pressure and the orientation of the interplanetary magnetic field (IMF). Observations have indicated that the magnetopause and bow shock are almost always in motion, sometimes at large velocities, even during periods of low solar and geomagnetic activity (Holzer et al., 1966; Anderson et al., 1968). The magnetopause and the bow shock motions are usually found to be coherent over a large distance. Previous statistical studies on the speed of the magnetopause motion showed that typical values were in the range 10-60 km/s (Anderson et al., 1968). Further investigations based on energetic ion remote sensing technique found that the velocities are usually less than 20 km/s but for one case, the value was 156 km/s (Kaufmann and Konradi, 1969). Time lag measurements from ISEE 1 and 2 found the speeds were in the range 5-380 km/s, with 80% falling in the range 10-80 km/s. (Berchem and Russell, 1982). Recent statistical study of the bow shock motion based on Cluster data shows that typical shock velocities are 35 km/s, and the fastest one was nearly 150 km/s (Horbury et al., 2002).

Although the magnetopause is commonly supposed to be an impenetrable boundary, the well-established existence of plasma of solar wind origin inside the magnetosphere implies that solar wind plasma is able to cross the magnetopause (Phan et al., 2005). A variety of processes has been proposed to account for this transport phenomenon. In the case of southward IMF, it is widely believed that magnetic reconnection is responsible for the transfer of solar wind mass into the

magnetosphere. In contrast, during northward IMF which mechanism facilitates the magnetosheath plasma to enter into the magnetosphere, especially through the subsolar point region, is still unclear. A possible candidate is the diffusive wave-particle transport by the lower hybrid drift instability (Gary and Eastman, 1979; LaBelle and Treumann, 1988; Treumann et al., 1991). An alternative mechanism is direct large-scale intrusion of plasma into the magnetosphere by the formation of the mixed transition layer at the magnetopause (Lemaire, 1977; Lemaire and Roth, 1978). In this chapter, we report a bulk excursion of the magnetosheath that was recorded simultaneously by the Cluster and TC-1 spacecraft in quiet solar wind conditions during a period of northward IMF on March 17, 2004. The relevant plasma transport phenomenon in the form of flux fluctuations below the ion gyrofrequency at the magnetopause is shown and interpreted as manifestation of the drift instability.

## 2. Observations

Fig.3.1 shows the solar wind parameters from the Advanced Composition Explorer (ACE). ACE is an Explorer mission that was managed by the Office of Space Science Mission and Payload Development Division of the National Aeronautics and Space Administration. ACE orbits the L1 libration point which is a point of Earth-Sun gravitational equilibrium about 1.5 million km from Earth and 148.5 million km from the Sun. The top and bottom panels in Fig. 3.1 show the magnetic fields and ion bulk velocity in the GSE-x direction respectively. During the period 00:00-02:00 UT, the IMF  $B_z$  was entirely northward, and the total field amplitude was almost constant. The solar wind velocity had only some small fluctuations and the kinetic pressure manifested some modest perturbations. The solar wind conditions in this time interval can be considered as moderately quiet. The propagation time for plasma from L1 point to Earth is well approximated by the advection shift. The advection shift is calculated by assuming that solar wind encountered by the monitor spacecraft travels ballistically from the L1 point to Earth, uniformly at the measured solar wind bulk

velocity. In the present event, the travel time from L1 to Earth for plasma with a bulk velocity of 450 km/s is about 55 minutes. Since the concerned time interval is 02:30-02:50 UT, hence ACE observations before 02:00 UT are relevant.

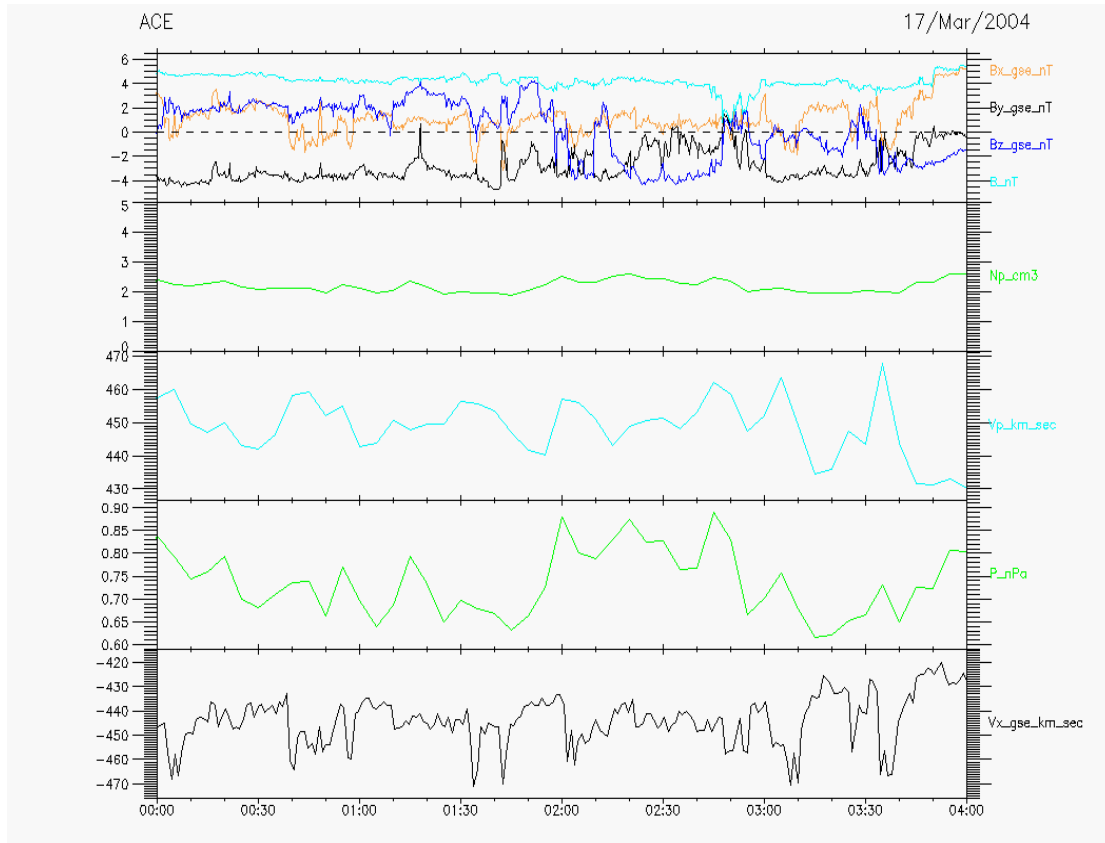


Fig.3.1 Solar wind parameters from ACE.

On early March 17, 2004, all the Cluster and TC-1 spacecraft were inbound. The geographical locations are schematically shown in Fig.3.2. The Cluster spacecraft were approximately at  $\mathbf{R} = (14.00, -6.87, -9.13)_{\text{GSE}} R_E$ . The individual orbits of Cluster are arranged so that the four spacecraft maintain an approximately constant separation, the scale of which can be altered during different mission phases from tens of km to 1  $R_E$  depending on the different science objectives. At that time, the characteristic scale of the tetrahedron was only about 200km. The TC-1 spacecraft was at  $\mathbf{R} = (12.03, -4.69, -1.80)_{\text{GSE}} R_E$ .

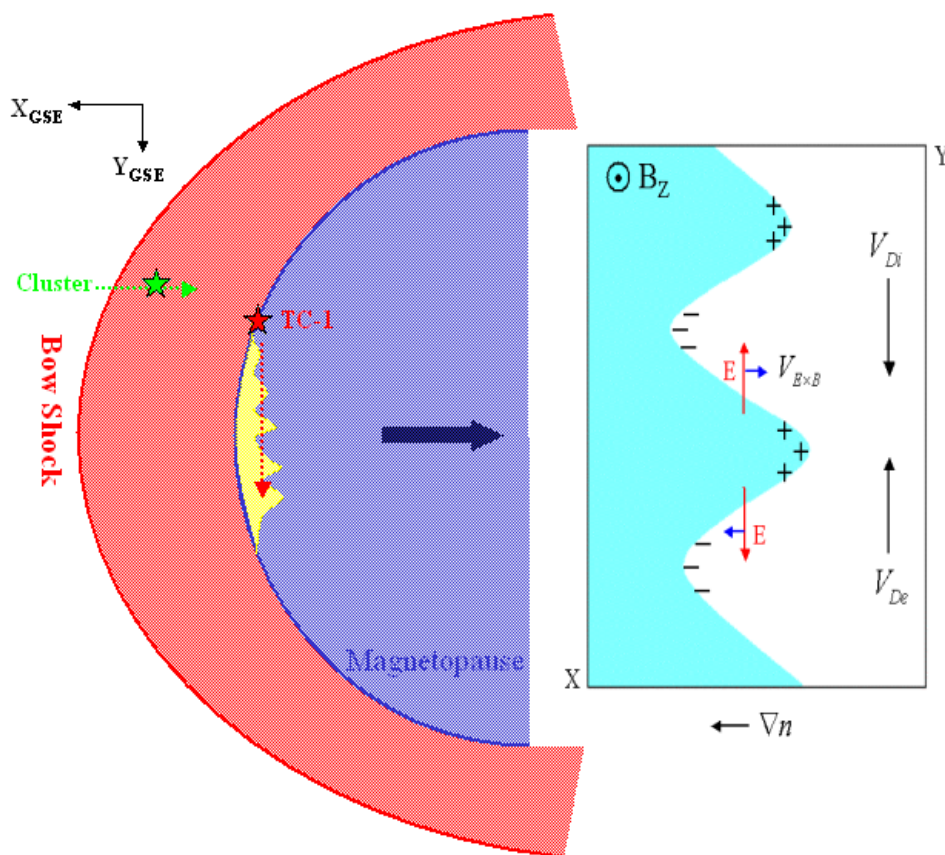


Fig.3.2 A schematic of the geographical locations of the Cluster and TC-1 spacecraft projected to the ecliptic plane. The bow shock and the magnetopause are shown by the red and blue bows respectively. The green and red stars and the dashed arrows denote the Cluster and TC-1 spacecraft and their orbits respectively. The ripples at the magnetopause describe the scenario of the drift instability. Meanwhile, its fundamental physical picture is illustrated at the right side. A sinusoidal electrostatic potential perturbation tight ties to a sinusoidal plasma density perturbation, and both them propagate with the plasma diamagnetic drift velocity. For more details see the text.

Fig.3.3, 3.4 and 3.5 show magnetic field measurements and hot ion measurements recorded by the Cluster spacecraft. The magnetic field measurements come from the FGM experiment (Balogh et al., 2001) and the hot ions from the CIS instrument (Rème et al., 2001). The hot ion measurements shown in Fig.3.3 and Fig.3.4 are from the HIA sensors onboard C3 and C1 respectively, while the proton measurements displayed in Fig.3.5 are from the CODIF sensor onboard C4. Fig.3.6 shows magnetic

field measurements and hot ion measurements recorded by the TC-1 spacecraft. The hot ion measurements come from the almost identical HIA instrument onboard TC-1 (Rème et al., 2005).

The first panel in Fig.3.3 displays the time-energy spectrogram of the low geometrical factor HIA sensor designed to detect the solar wind particles. The density and velocities are shown in the second and third panels. The fourth panel shows the time-energy spectrogram of the high geometrical factor C3 HIA sensor, which is designed to detect the magnetosheath and magnetospheric particles. The density and velocities from this detector are shown in the fifth and sixth panels. Until 02:30 and after 02:47 UT, the energy spectrum shows almost monoenergetic ions, with velocities nearly in the x-direction (GSE). All these features indicate that the observations were recorded inside the solar wind, while during the interval 02:30-02:47 UT, the observational characteristics indicate that the spacecraft entered into and stayed in the magnetosheath. Due to the deceleration and thermalization of the solar wind plasma behind the bow shock, the ion energy spectrum in the magnetosheath is spread, and the corresponding density rises to a much higher level. During this period, the bulk velocities also decreased and was deflected in comparison to the solar wind velocities. Because of the very small size of the tetrahedron all Cluster showed very similar features. As shown in Fig.3.4 and Fig.3.5 respectively, until 02:30 and after 02:47 UT, C1 and C4 also observed the monoenergetic solar wind plasma; and during the interval 02:30-02:47 UT, they observed the thermalized magnetosheath plasma. Likewise, TC-1 was inside the magnetosheath till 02:30 and after 02:47 UT as it can be easily identified from Fig.3.6 and also the bottom panel in Fig. 3.3. During the interval 02:30-02:47 UT, it is clear that the observations were recorded in the magnetosphere, where the ion energy spectrum is in a higher energy regime compared to that of the magnetosheath. Here, the reason that the density recorded by the low geometrical factor HIA sensor decreases inside the magnetosheath is due to the fact that it is in the solar wind mode and therefore it is an instrument effect. The HIA instrument has two  $180^\circ$  field of view sections parallel to

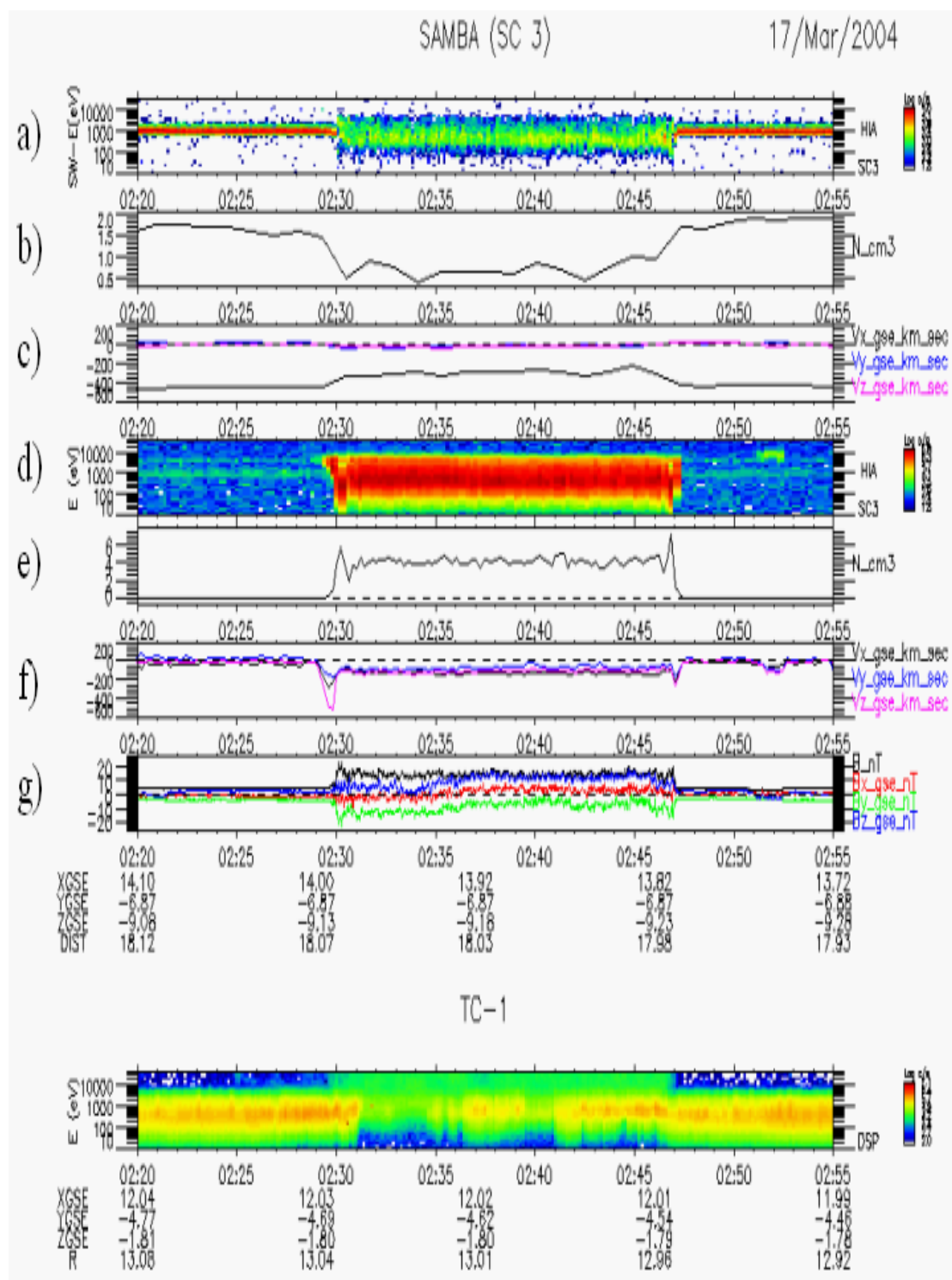


Fig.3.3 Magnetic field and hot ion parameters from Cluster C3. From top, a) -c) are time-energy spectrogram and density and velocities of solar wind particles respectively, d)-f) are time-energy spectrogram and density and velocities of magnetosheath particles respectively. g) components of magnetic field. The last panel is hot ion time-energy spectrogram from TC-1.

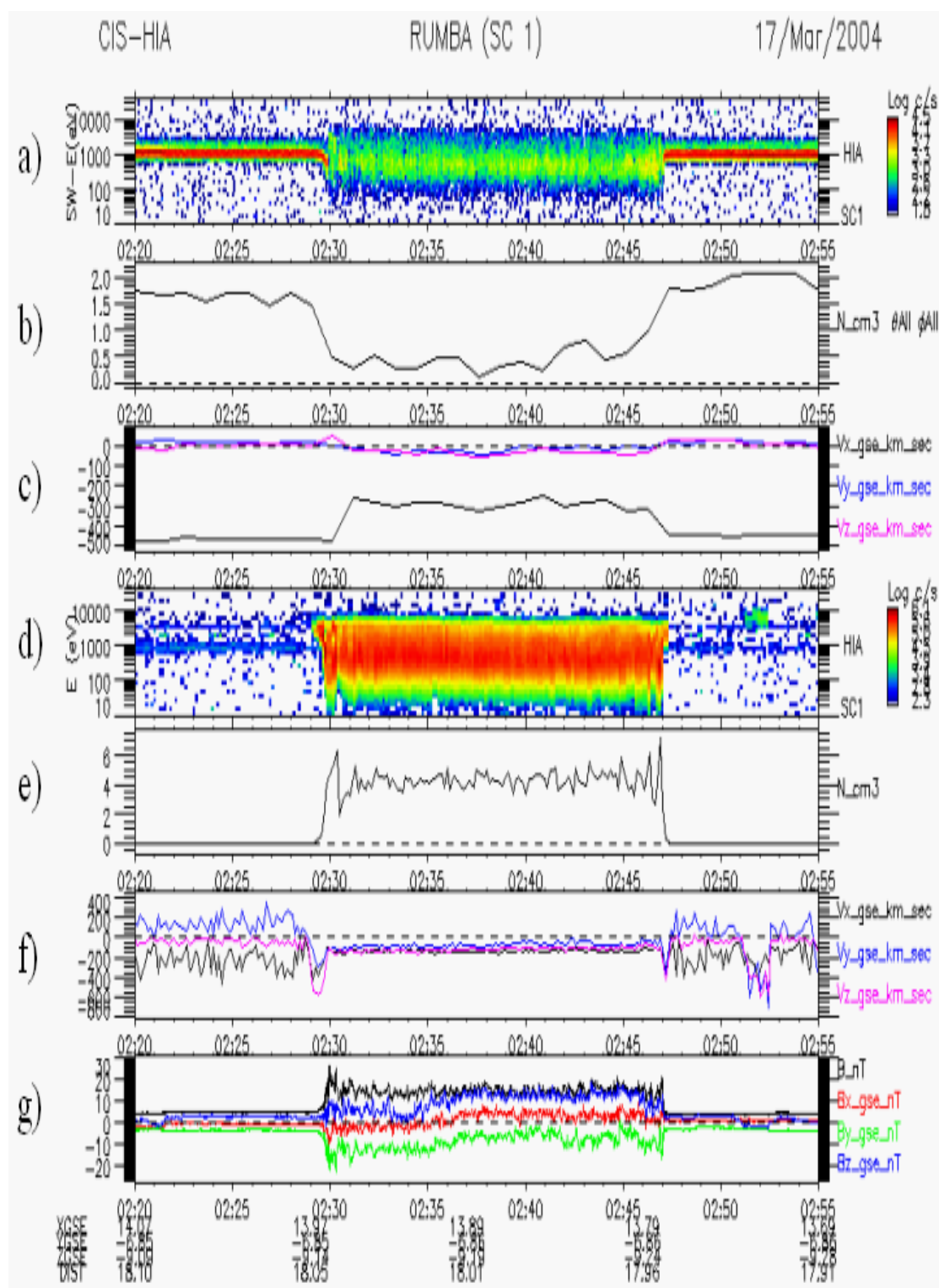


Fig.3.4 Magnetic field and hot ion parameters from Cluster C1. From top, a) -c) are time-energy spectrogram and density and velocities of solar wind particles respectively, d)-f) are time-energy spectrogram and density and velocities of magnetosheath particles respectively. g) components of magnetic field.

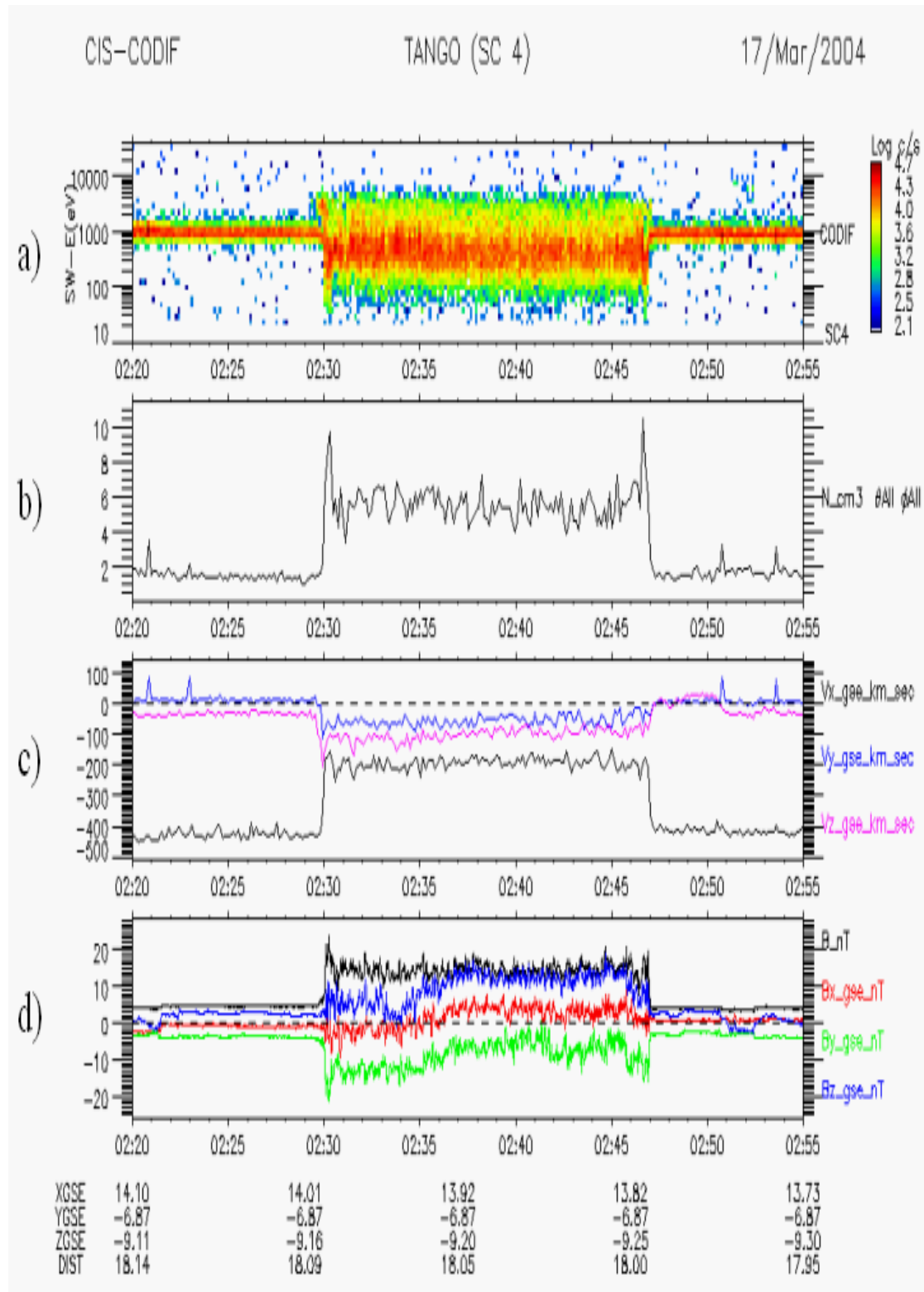


Fig.3.5 Magnetic field and hot ion parameters from Cluster C4. From top, a) time-energy spectrogram. b) density and c) components of bulk velocity in GSE coordinates. d) components of magnetic field.

the spin axis with two different sensitivities, corresponding respectively to the 'high G' and 'low g' sections. The 'low g' section of HIA sensor allows detection of the solar wind and the required high angular resolution is achieved through the use of 8 x 5.625° central anodes, the remaining 8 sectors having in principle 11.25° resolution. In contrast, the 180° 'high G' section is divided into 16 anodes, 11.25° each.

Combining the observations of the Cluster and TC-1 spacecraft, the present event reveals a large-amplitude bulk excursion of the magnetosheath. Initially, the Cluster spacecraft was in the solar wind and TC-1 in the magnetosheath. At 02:30 UT, a rapid bulk sunward motion of the magnetosheath took place Cluster entered the magnetosheath, and TC-1 encountered the magnetopause. After about 17 minutes at 02:47 UT, a rapid earthward motion of the magnetosheath occurred. Thus Cluster reentered the solar wind, and TC-1 returned to the magnetosheath. An impressive feature of the present event is the good coherence between the bow shock and the magnetosheath motion. To expose this point, we added the time-energy spectrogram recorded at the same time by TC-1 satellite on the bottom panel of Fig.3.3. It can be seen that the period of Cluster in the magnetosheath exactly coincides with the period of TC-1 at the magnetopause.

In the present event, the magnetosheath magnetic field has components with a positive  $B_z$ , a negative  $B_y$  and a nearly zero  $B_x$ , while the magnetopause magnetic field is mainly in the  $z$  direction with small  $B_x$  and  $B_y$  components. So, the magnetosheath magnetic field is sheared to the terrestrial magnetic field with an angle of about 45°. Based on the temperature of magnetosheath ions and the total magnetic field, we can estimate the proton gyroradius  $r_i = v_i / \omega_{ci}$  to be approximately 80km and the gyroperiod  $T = 2\pi / \omega_{ci}$  about 2s, where  $v_i = \sqrt{2kT_i / m_i}$  is the proton thermal velocity,  $\omega_{ci} = eB / m_i c$  is the proton gyrofrequency,  $T_i$  is proton temperature,  $m_i$  is the mass of proton,  $B$  is the total magnetic field, and  $c$  is the light speed in vacuum.

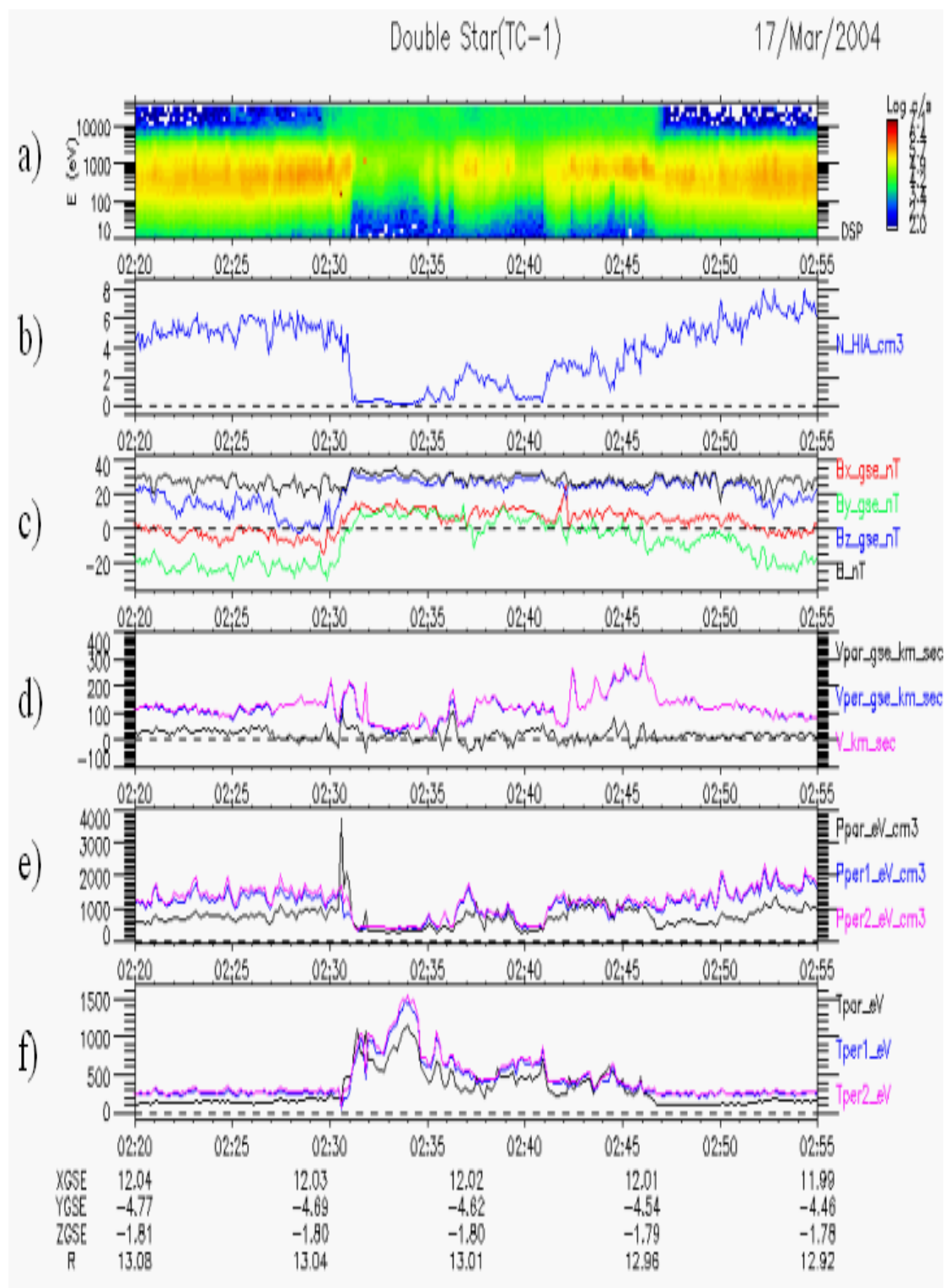


Fig.3.6 Magnetic field and hot ion parameters from TC-1. From top to bottom, are: a) hot ion time-energy spectrogram, b) hot ion density, c) components of the magnetic field, d) ion bulk velocities. e) and f) components of hot ion pressure, and temperature respectively.

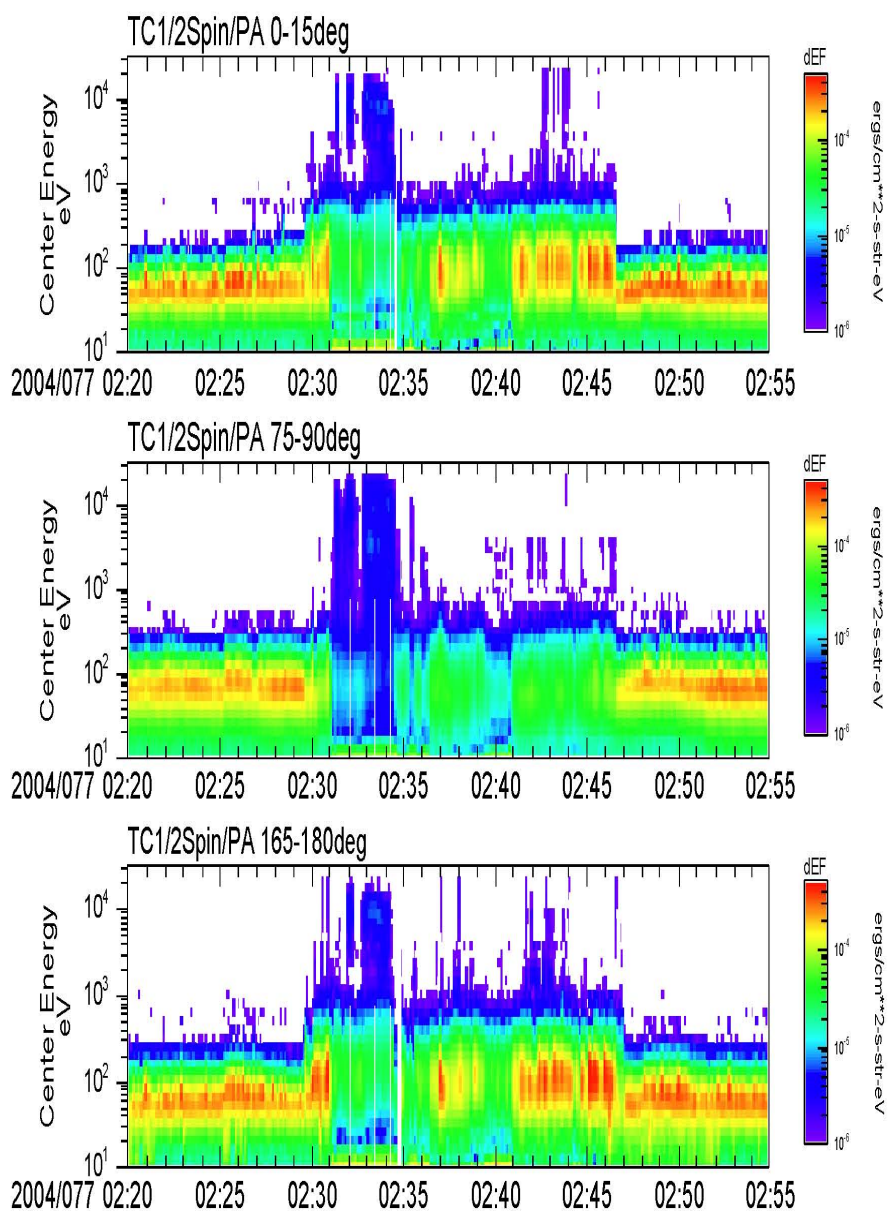


Fig.3.7 Time-energy spectrogram of low energy electrons from TC-1. From top to bottom, are electron energy fluxes in the pitch angle range of  $0-15^\circ$ ,  $75-90^\circ$  and  $165-189^\circ$  respectively.

Another remarkable feature recorded by TC-1 at the magnetopause is the mixture of the magnetosheath and magnetospheric ion composition: the high energy ions characteristics of magnetosphere ions, are mixed with variable magnetosheath ions. In the time interval 02:30 and 02:47 UT, the encountered mixtures is the well known low latitude boundary layer (LLBL) composition, which has a completed energy spectrum of both magnetosheath and magnetospheric ions. Besides the LLBL, there are some irregular mixtures, where some sporadic magnetosheath composition is observed in a stable background of the magnetospheric ion composition. TC-1 was skimming over the ellipsoidal magnetopause at that time, hence these flux fluctuations should be regarded as local spatial structures at the magnetopause instead of temporal variations due to the radial vibration of the magnetopause. Otherwise, the background of the magnetosheath and magnetospheric ion composition should be alternately observed, instead of a stable background of the magnetospheric ion composition that was observed. Therefore, the fluctuated mixtures actually represent a transport of the magnetosheath ions across the magnetopause. A possible ripple structures at the magnetopause is shown in the schematic of Fig.3.2. Note that the duration of each fluctuation structure is much longer than the ion gyroperiod ( $\sim 2$ s). For example, during 02:35-02:36 UT, some wavy flux tubes were recorded, and each tube persisted for 20s, and those fluctuations encountered later have even longer durations.

Fig.3.7 shows time-energy spectrogram of low energy electrons detected onboard the TC-1 spacecraft. From top to bottom, are electron energy fluxes in the pitch angle range of  $0-15^\circ$ ,  $75-90^\circ$  and  $165-189^\circ$  respectively. The electron observations also show a mixture of magnetosheath and magnetospheric compositions. The higher energy population (lower flux) is the magnetospheric population, while the lower energy population (higher flux) is from the magnetosheath.

### 3. Discussion

#### 3.1 Excursion velocity of the bow shock:

The small size of the Cluster tetrahedron allows the normal direction of the bow shock to be determined by a magnetic field gradient method (Shen *et al.*, 2007). Then the velocity in the normal direction of the shock front can be estimated by the shock mass flux conservation equation, that is,  $\rho_u(\mathbf{V}_u - V_n \mathbf{n}) \cdot \mathbf{n} = \rho_d(\mathbf{V}_d - V_n \mathbf{n}) \cdot \mathbf{n}$ , where  $\rho_u$  ( $\rho_d$ ) and  $\mathbf{V}_u$  ( $\mathbf{V}_d$ ) are the plasma density and velocity upstream (downstream) of the shock respectively,  $\mathbf{n}$  is the shock normal vector, and  $V_n$  is the excursion velocity in the normal direction (Schwartz, 1998). From the above equation,  $V_n$  can be solved to be  $V_n = \Delta(\rho \mathbf{V}) \cdot \mathbf{n} / \Delta \rho$ . For the first bow shock encounter at 02:30 UT, the normal direction is determined to be  $\mathbf{n} = (0.740, -0.580, -0.340)_{\text{GSE}}$ . The density and velocity upstream and downstream of the shock are  $\rho_u = 1.60 \text{cm}^{-3}$ ,  $\mathbf{V}_u = (-453, 18, -4)_{\text{GSE}}$  km/s and  $\rho_d = 5.76 \text{cm}^{-3}$ ,  $\mathbf{V}_d = (-92, -74, -112)_{\text{GSE}}$  km/s respectively. Hence  $V_n$  is evaluated to be roughly 156 km/s. Similarly, for the second bow shock encounter at 02:47 UT, the normal direction is  $\mathbf{n} = (0.744, 0.141, -0.653)_{\text{GSE}}$ . The density and velocity upstream and downstream of the shock are  $\rho_u = 1.63 \text{cm}^{-3}$ ,  $\mathbf{V}_u = (-437, 13, 20)_{\text{GSE}}$  km/s and  $\rho_d = 7.16 \text{cm}^{-3}$ ,  $\mathbf{V}_d = (-102, -31, -83)_{\text{GSE}}$  km/s, hence  $V_n$  is approximately 65 km/s.

Which mechanism is responsible for the motion of the bow shock and magnetopause is a long-standing issue. It has been proposed that certain plasma instabilities, for instance the convective Helmholtz-Kelvin instability, which can occur when velocity shear is present within a continuous fluid, might be responsible for the motion of the magnetospheric boundary and that disturbances thus created propagate along the flanks of the magnetopause as a kind of magnetohydrodynamic surface waves (Anderson *et al.*, 1968). An alternative approach is that periodic perturbations in the solar wind are responsible for driving the motion of the bow shock and magnetopause (Smit, 1968). Although here a large-amplitude excursion of magnetosheath was

clearly observed, the driving source is not clear since neither an apparent correlation between the magnetosheath motion and the variance of solar wind parameters can be found nor large scale MHD waves were observed. The identification of the driving mechanism of the motion of bow shock and magnetopause is left for future investigation.

### 3.2 Drift instability:

During the period when TC-1 stayed at the magnetopause, there were no apparent magnetic perturbation, hence an electrostatic type instability is responsible for the generation of the ripple structures (Fig.3.2). Moreover, since there were prominent density gradient and the corresponding plasma pressure gradient at the magnetopause, thus they can act as free energy to excite drift instability, which is a collective mode due to plasma inhomogeneity and whose fundamental physical picture is illustrated on the right side of Fig.3.2. Here, a sinusoidal density perturbation is assumed. In the scenario of drift wave, the dynamics of electrons parallel to the magnetic field is adiabatic. Therefore, a plasma density perturbation directly connects to a plasma potential perturbation via the electron Boltzmann distribution in the parallel direction and an electric field in the plane perpendicular to the magnetic field builds up. Consequently, the  $E \times B$  drift leads to propagation of the perturbation in the plasma diamagnetic drift direction, where the ion diamagnetic drift direction is eastward and opposite to that of electrons. In the magnetopause environment, the electron perpendicular temperature is much lower than the ion perpendicular temperature (Phan et al., 2005). Thus, the electron diamagnetic drift velocity can be neglected and the drift wave propagates in the positive  $y$  direction with the ion diamagnetic drift velocity.

Drift waves are intrinsically three-dimensional and the plasma dynamics parallel to the magnetic field is a crucial parameter for stability. Due to an adiabatic and instantaneous electron response parallel to the magnetic field, the initial perturbation is linearly stable. However, when certain effects that lead to non-adiabaticity of

electrons react, or in other words, the parallel dynamics of electrons is somewhat inhibited, the potential perturbation will increase slowly and the drift wave becomes unstable. Therefore, in the low frequency regime drift instability is essentially an electrostatic instability due to charge accumulation and accordingly electrostatic potential perturbation. This kind of manifestation in the present event is revealed in Fig.3.8. The first panel shows the time-energy spectrogram of electrons in the energy range of 0.2-0.4MeV provided by the TC-1 HEED experiment between 02:34-02:44 UT (Cao *et al.*, 2005). The second panel is HIA time-energy spectrogram and the third panel shows the ion bulk velocities deduced from HIA measurements: the black curve represents the total velocity, and the blue and red represent parallel and perpendicular velocities respectively. In the interval 02:35:58-02:36:12 UT, a filament of electron flux up to  $400\text{cm}^{-2}\text{sr}^{-1}\text{s}^{-1}$  was observed, which implies that a region of negative charge accumulation and accordingly a potential minimum is encountered. While during the period of 02:41:26-02:42:25 UT, a flux tube with ion flux below ten  $\text{cm}^{-2}\text{sr}^{-1}\text{s}^{-1}$  was recorded, which implies that a region of positive charge accumulation and accordingly a potential maximum. Also, as shown by two short dashed lines, during the period of 02:39:22-02:40:51 UT, a minor potential minimum is exhibited, which is bounded by two minor regions of negative charge accumulation. Why the whole region of this potential perturbation did not display apparent variations of electron flux but only at the edges? Since electrons satisfy approximately the Boltzmann distribution and also the potential perturbation at that time is small, hence the electron perturbation is proportional to the ambient plasma density and inversely proportional to the plasma temperature. Thus, the electron perturbation and corresponding charge accumulation in the magnetospheric ambience are much smaller than that in the magnetosheath ambience and accordingly no apparent variations of electron flux are observed.

In comparison with the second panel in Fig.3.8, it can be found that all the potential perturbations basically have a good correlation to the ion density perturbations. As shown in the schematic Fig.3.2, a potential minimum corresponds to a low density region, where only the magnetospheric composition was encountered; while a

potential maximum corresponds to a high density region, where the magnetosheath composition was met and mixed with the magnetospheric composition. This fact is coincident to the intrinsic feature of drift instability, and the electrostatic potential perturbation tightly ties to the plasma density perturbation. At the beginning there is no phase shift between them; however the phase shift increases rather slowly due to charge accumulation and eventually reaches to a small but finite value. Here, the minor potential minimum observed in the interval 02:39:22-02:40:51 UT is exactly a growing potential perturbation during the evolution of drift instability. In fact, this growing potential minimum and the fully enhanced potential maximum encountered later during 02:41:26-02:42:25 UT make up spatially a complete sinusoid-like perturbation propagating in the positive  $y$  direction on one hand, while they also record temporally the history of potential growth on the other hand, namely, the time sequence of the potential growth from the initial minor potential minimum to the final fully enhanced potential maximum.

As shown by two long dashed lines at 02:36:10 and 02:42:20 UT respectively in Fig.3.8, at the end of the record of both major potential perturbations, a pulse of the perpendicular velocity is observed. These pulses are due to the  $E$  cross  $B$  motion in the nonlinear regime. In the linear stage of drift instability, although the potential perturbation grows up slowly, however both the potential and density perturbation harmonically oscillate and no net mass transport across the boundary takes place. When the potential perturbation is high enough, the  $E \times B$  motion will give rise to convective instability, causing mass interchange between the high density region and the low density region. Consequently, the exchanged magnetosheath ion fluxes are observed in the interval 02:36:20-02:37:40 UT and after 02:42:20 UT respectively. It is worthy to point out that associated with the first perpendicular velocity pulse, there is also a parallel velocity pulse, which implies that at this stage, the ion parallel motion is relevant, or in other words, the ion acoustic wave plays a role in the system evolution. For the second perpendicular velocity pulse, no parallel velocity pulse occurs. However, an apparent corresponding magnetic perturbation can be found from

the third panel in Fig.3.6. It indicates that at that stage, the instability is not merely electrostatic but electromagnetic, namely, a shear Alfvén wave is involved in the whole dynamics.

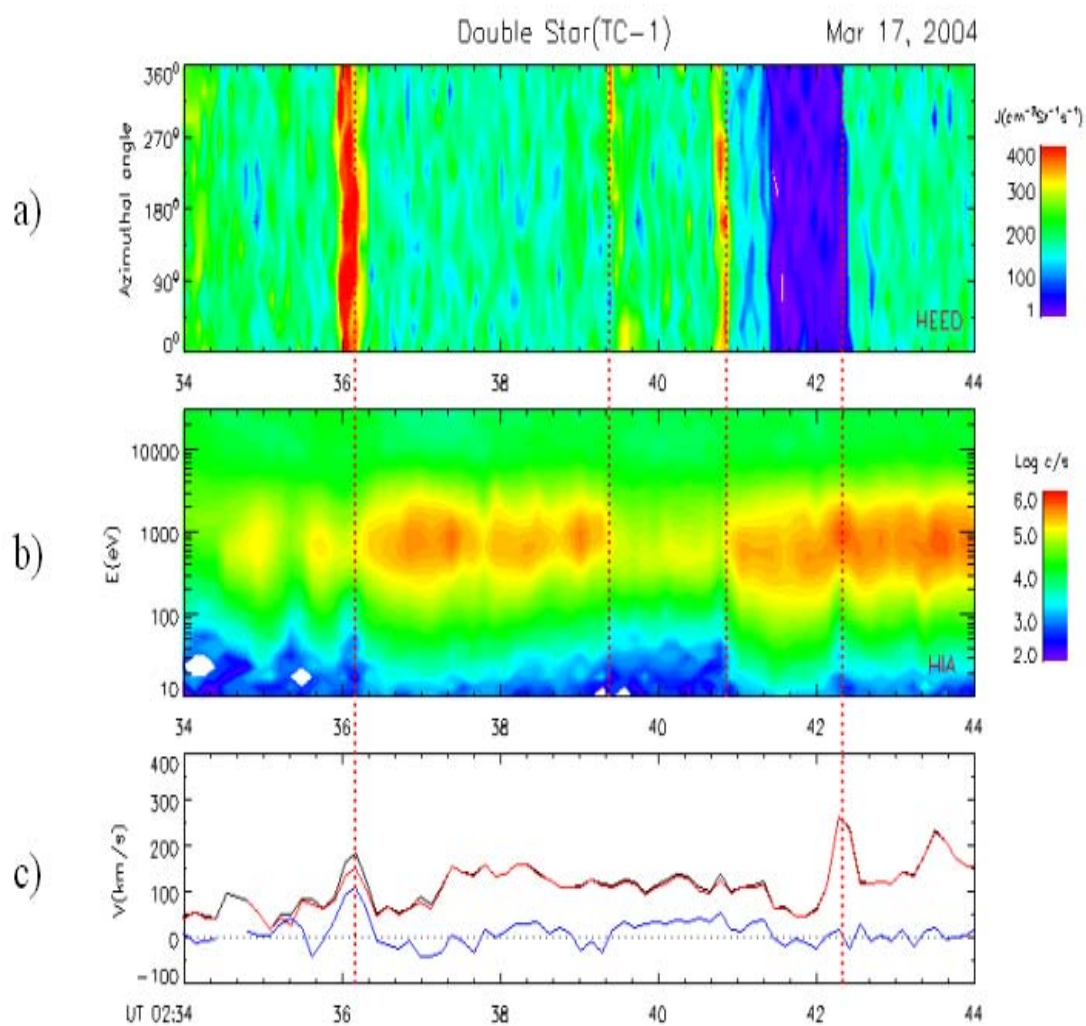


Fig.3.8 a) Time-energy spectrogram of electrons in the energy range of 0.2-0.4MeV recorded by the HEED experiment onboard the TC-1 spacecraft. The vertical axis is the azimuthal angle, which is defined in the plane perpendicular to the satellite spin axis. b) HIA time-energy spectrogram. c) Ion bulk velocities: the black curve represents the total velocity, and the blue and red represent parallel and perpendicular velocities respectively.

In contrast to the measurements of high energy electrons that reveal some evidence on charge accumulation and potential perturbation, the observations of low energy electrons as shown in Fig.3.7 display no similar indication. The reason is thought that high energy electrons show non-adiabaticity in the parallel motion due to their larger effective viscosity and are responsible for the charge accumulation. Another issue is the stabilization of magnetic shear effect on the drift instability, since in the present event the magnetosheath magnetic field is sheared to the terrestrial magnetic field with an angle of about  $45^\circ$ . The answer is that due to the bulk excursion of magnetosheath, a localized region with a small magnetic shear or without shear developed. This is made more apparent in the third panel in Fig.3.6. After 02:47 till 02:51 UT, the plasma measurements clearly indicate that the satellite was already drifting away from the magnetopause and entered into the magnetosheath, while the magnetic field records were still similar to that of the terrestrial magnetic field.

Finally, the perpendicular wavelength can be estimated by the product of each duration time of the filament structure and the ion diamagnetic drift velocity. The ion diamagnetic drift velocity is  $v_{ith} \cdot \rho_i / L_n$ , where  $v_{ith}$  is the ion thermal velocity,  $\rho_i$  is the ion gyroradius and  $L_n^{-1} = -dn/n dx$  is the scale length of the density gradient.

Usually, at the magnetopause the scale length of density gradient is typically a few ion gyroradii (Winske, 1996). Here, we assume that the ratio of the characteristic length to the ion gyroradius is about five, so the ion diamagnetic drift velocity is one-fifth of the ion thermal velocity and is about 30km/s. Then, the perpendicular wavelength of drift waves can be estimated to be roughly from 1200km to 5400km. Since a drift wave has a much larger parallel wavelength than its perpendicular wavelength, the volume of each flux tube is large and hence eventual particle transport by exchange of flux tubes is actually considerable. Based on this interpretation, it is interesting to point out that in contrast to the most investigated drift instability at the magnetopause in the low hybrid regime and the assumed stationary turbulent diffusion, the observations presented here reveal the drift instability frequency is much smaller than

the ion gyrofrequency and consequently large-scale convective interchange seems to be a more efficient transport mechanism at the magnetopause during periods of northward IMF.

#### 4. Conclusion

In summary, a large-amplitude excursion of the magnetosheath in quiet solar wind conditions during period of northward IMF is reported, which was observed simultaneously by the Cluster and TC-1 spacecraft. The good coherence between the bow shock motion and the magnetopause motion is revealed and the excursion velocity of the bow shock motion is analyzed by a multi-satellite data analysis technique. Furthermore, the relevant plasma transport phenomenon in the form of flux fluctuations below the ion gyrofrequency at the magnetopause is shown and interpreted as a manifestation of the drift instability. It is indicated that even in the case of IMF having a large shear to the terrestrial magnetic fields, a localized region at the magnetopause without shear can develop due to the bulk motion of the magnetosheath and hence this stabilization factor in the drift instability is absent. In addition, evidence of charge accumulation and electrostatic potential perturbation related the evolution of drift instability are exhibited from the measurements of high energy electrons. All these potential perturbations show a good correlation to the ion density perturbations. Moreover, the relevant rapid ExB motion in the nonlinear stage and the corresponding mass exchange are recorded. Finally, based on rough estimation of the scale of drift wave lengths, it is pointed out that in contrast to the most investigated drift instability at the magnetopause in the low hybrid regime and the assumed stationary turbulent diffusion, the observations presented here reveal the drift instability to be much less than the ion gyrofrequency and consequently large-scale convective interchange seems to be a more efficient transport mechanism at the magnetopause during a period of northward IMF. The results of this chapter have been published in Cai et al., 2009a.



## **Chapter 4**

### **Foreshock-like Density Cavity in the Magnetotail Reconnection**

#### 1. Introduction

Magnetic reconnection plays a crucial role in the dynamics of the magnetotail. During magnetic reconnection, the lobe plasma is convected toward the central plasma sheet, and is driven out from the X-type diffusion region in the form of ion jets in two opposite directions (Hones, 1979). The magnetic topological structures of these ion jets and their effects on the surrounding plasmas have been intensively investigated. For instance, reconnection generated flux ropes, usually described as a three-dimensional “rope” which has a helical magnetic field structure together with a strong core field, were observed (Hones, 1977; Slavin et al., 1989). Also, the interaction between the fast-moving flux rope and the lobe manifests as a bulge that compresses the lobe plasma, which is called traveling compressed plasma region (Slavin et al., 1984, 2005). Moreover, the ion outflows observed in the Earth’s magnetotail reconnection show a wide variety of singular boundary layers, in addition to the well-known slow-mode shock boundary (Eriksson et al., 2004). On the basis of Geotail spacecraft data, it had been found that during magnetic reconnection a contact discontinuity exists binding two different plasma regions in the sheet, separating the shock-heated plasma from plasma that is Joule heated by magnetic diffusion (Hoshino et al., 2000). Computer simulations also show that a tangential discontinuity inside the plasmoid can form to separate the accelerated plasmas from the original plasma (Abe and Hoshino, 2001). Moreover, simulation results indicate the interaction between the fast reconnection jets and the original sheet plasmas associated with a magnetic loop can form a fast shock at the edge of the reconnection jet (Ugai, 1996, 1999).

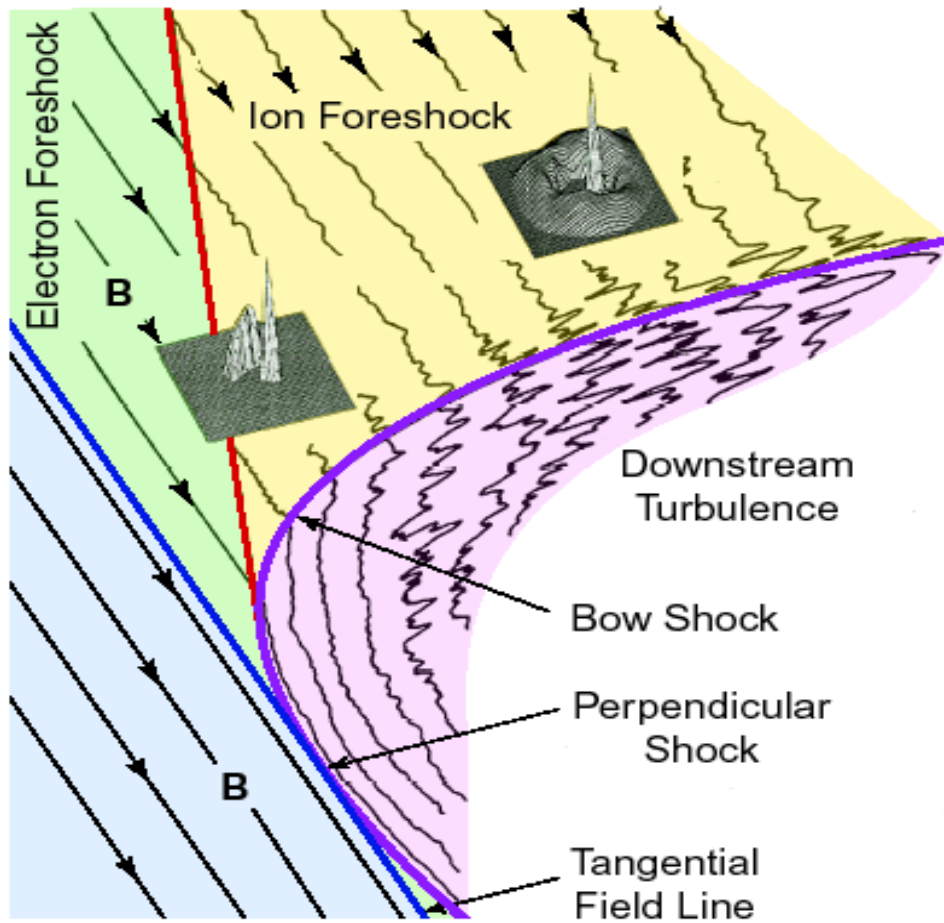


Fig.4.1 A schematic of the terrestrial shock-foreshock system. The foreshock, which is confined to the region of space behind the tangent field line (blue line), exhibits complex spatial structure. Just behind the tangent field line is the electron foreshock; here, only backstreaming electrons are observed. Behind the ion foreshock boundary, field-aligned backstreaming ion distributions are typically observed. Deeper in the foreshock, close to the quasi-parallel shock, diffuse backstreaming ion distributions are observed. (Treumann and Scholer, 2001).

In the Geospace, the most significant singular boundary created by high-speed plasmas confronting an obstacle is the terrestrial magnetospheric bow shock. When the supersonic solar wind plasma carrying the interplanetary magnetic field encounters Earth's dipole magnetic field, the bow shock is formed, which slows down the solar wind plasma from supersonic to subsonic speeds and thermalises it. Simultaneously, a foreshock forms if a part of incident particles is reflected. The

foreshock is a region upstream of the bow shock, which is magnetically connected to the bow shock and comprises both incident solar wind plasma and reflected particles. For the quasi-perpendicular shock, the foreshock is confined to the shock foot, while upstream of the quasi-parallel shock, it occupies a much larger area (Balogh et al., 2005). The foreshock possesses complex kinetic processes, which give rise to accordingly unusual spatial structure ((Bale et al., 2005, Eastwood et al., 2005). It is generally thought that a certain portion of the incident particles can be specularly reflected at the shock magnetic ramp (Paschmann et al., 1980; Gosling et al., 1982, Schwartz et al., 1983). In a shock rest frame, an incident particle with a velocity consisting of components parallel and perpendicular to the normal of the shock reflects specularly at the shock surface by the shock electric field such that the component perpendicular to the normal remains unchanged while the component parallel to the normal is reversed. Those reflected particles that have high enough velocity parallel to the magnetic field (hence their guiding center velocity along the shock normal is larger than the convection speed) will escape upstream along the field line to create a backstreaming field-aligned beam, which move both along the magnetic field line and simultaneously drift in the convective electric fields of the incident particles. Eventually, these backstreaming field-aligned beams can be found behind the tangential magnetic field line. Therefore, the upstream boundary of the foreshock is the locus of the tangential field lines, and the downstream boundary of the foreshock is the quasi-parallel part of the shock. The higher energy particles can be observed close to the upstream foreshock boundary, while the lower energy particles can be recorded further downstream. Just behind the tangent field line is the electron foreshock. The ion foreshock will be encountered downstream the electron foreshock. The reflected field-aligned ion beams with the smallest drift distance make up the upstream boundary of the ion foreshock, which is also called the leading ion foreshock boundary. Behind the leading ion foreshock boundary, field-aligned backstreaming ion distributions are observed. Deeper in the foreshock, diffuse backstreaming ion distributions are usually recorded (Meziane et al., 2001, 2004).

Moreover, there exists a second boundary within the ion foreshock, closer to the quasi-parallel shock, usually referred to as the ULF foreshock boundary or the ion foreshock wave boundary (Le and Russell, 1992, Meziane et al., 1998). This boundary borders the domain of ULF wave activity. The terrestrial shock-foreshock system is schematically shown in Fig.4.1.

In this chapter, the following particular scenario is considered, where the reconnection ion jets, especially those traveling earthward, collide with the original plasmas at rest before reconnection. The reconnected magnetic field lines carried outward by the high-speed ion jet emanating from the X-type diffusion region can be blocked by the original magnetic field lines bordering the outflow region. Therefore, in the edge of outflow region, there exists a region where field lines are piled up. When the magnetic compression, or in other words the impact of ion jet, is intense enough to cause some kinds of singular boundary layer such as a discontinuity or a shock to form, it isn't hard to find that there is a remarkable similarity in the underlying physical process between the present situation and that of the bow shock. However, since there are many differences in the respective environments of two cases, whether the ion jets can interact with the original plasmas in a bow shock-like manner is still unclear. Also, since the existence of reflected particles is an intrinsic feature of collisionless shock, can some particular characteristics relevant to foreshock-like structure be exhibited in the vicinity of a steepened boundary of the field lines piled up region in the edge of outflow region?

Here, we present some reliable observations of a singular boundary of an ion jet that is formed due to its interaction with the original plasmas, and report observations of a density depletion cavity with a foreshock-like structure in the outflow region of magnetotail reconnection. First, an overview of the reconnection layer encountered by the spacecraft is given. Then, particle kinetics and magnetic field measurements are analyzed in an attempt to reveal the remarkable characteristic structures in the density cavity that manifests a highly similar morphology to the foreshock region.

## 2. Observations

### 2.1 Overview

During the time interval 00:30-00:50 UT on August 6, 2003, the 4 Cluster spacecraft crossed the near-Earth magnetotail at  $X_{\text{GSM}} = -17 R_E$ . Fig.4.2, 4.3 and 4.4 show magnetic field measurements and hot ion measurements from spacecraft 4, 1 and 3 respectively. The magnetic field measurements come from the FGM experiment (Balogh et al., 2001) and the hot ions from the CIS instrument (Rème et al., 2001). The proton measurements shown in Fig.4.2 are from the CODIF sensor onboard C4 (HIA is not onboard this spacecraft), while the hot ion measurements displayed in Fig.4.3 and Fig.4.4 are from the HIA sensors onboard C1 and C3 respectively.

While the spacecraft was in the plasma sheet of the southern hemisphere, due to a negative  $B_x$ , it suddenly observed an earthward fast proton flow with a total velocity up to  $\sim 610$  km/s in the interval 00:33:20-00:35:10 UT. Accompanied with this plasma ejection is a strong magnetic field variation. The magnetic field magnitude of the leading boundary increases from  $-20$  nT to  $-34$  nT in  $B_x$  and from 3 to 10 nT in  $B_z$ . In this jet, the proton density decreases from  $0.72 \text{ cm}^{-3}$  to  $0.32 \text{ cm}^{-3}$ , about half of the original level. The oxygen ion abundance is very low and not shown here.

After passing the density cavity, the spacecraft subsequently observed two density dips at 00:37:30 UT and 00:43:40 UT respectively. Finally, the spacecraft met a tailward fast flow with a total velocity up to  $\sim 600$  km/s in the interval 00:45-00:49 UT. In this event,  $B_0 = 25$  nT,  $T_H = 5$  keV, and  $n_H = 0.7 \text{ cm}^{-3}$ , where  $B_0$  is the magnetic field in unperturbed plasma sheet,  $T_H$  and  $n_H$  are the proton temperature and density respectively. The Alfvén speed  $V_A$ , the proton Larmor radius  $\rho_H$ , and the proton inertial length  $c/\omega_{pH}$  are respectively  $V_A = 650$  km/s,  $\rho_H = 410$  km and  $c/\omega_{pH} = 270$  km.

Because of the very small size of the 4 spacecraft tetrahedron ( $\sim 200$  km) all spacecraft

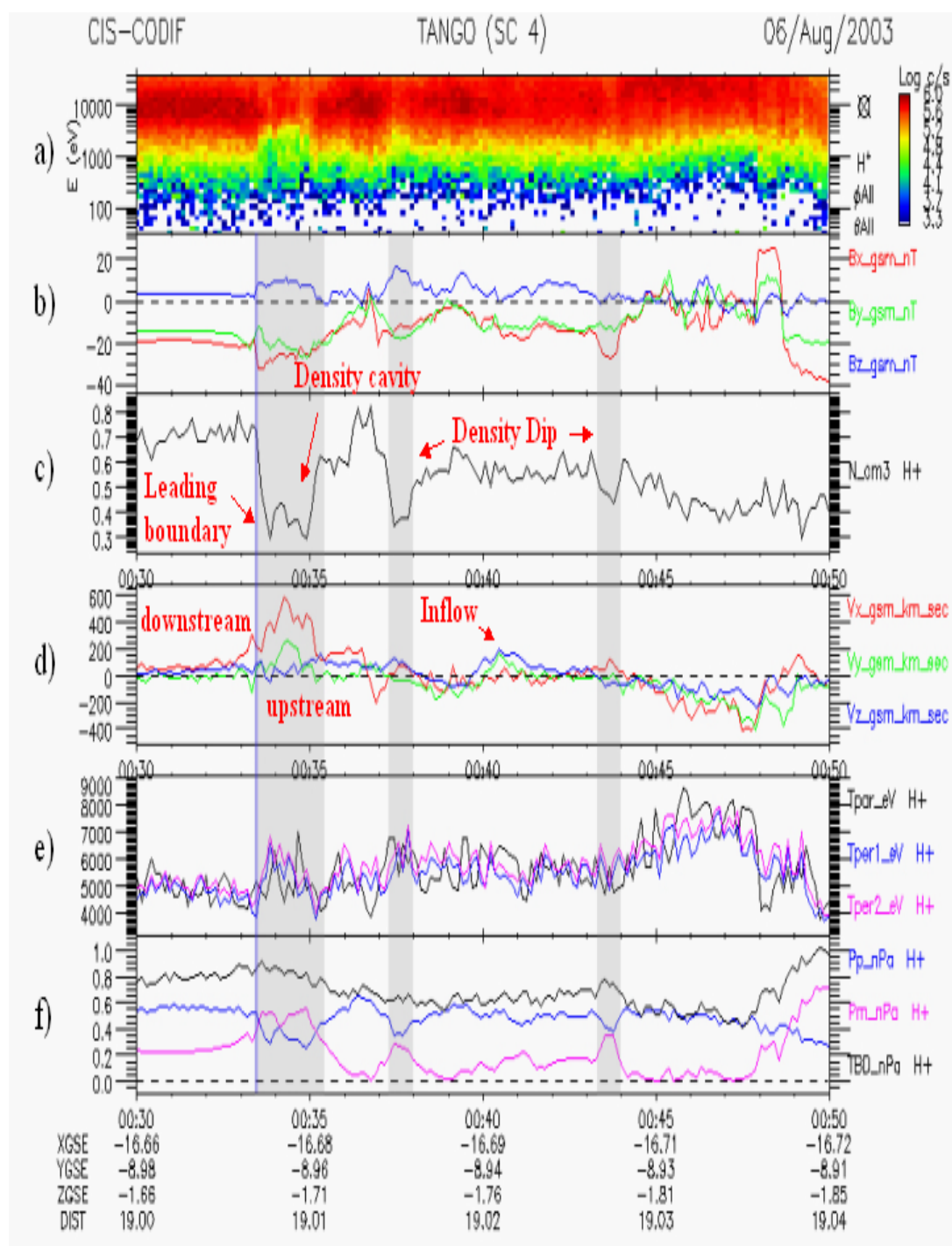


Fig.4.2 Magnetic field and proton measurements from C4. From top: a) time-energy spectrogram, b) components of magnetic field, c) and d) proton density and bulk velocities in GSM coordinates respectively, e) proton pressure components parallel and perpendicular to the magnetic field, and f) magnetic pressure, proton pressure and total pressure respectively. The shadows denote the density cavity and two density dips respectively.

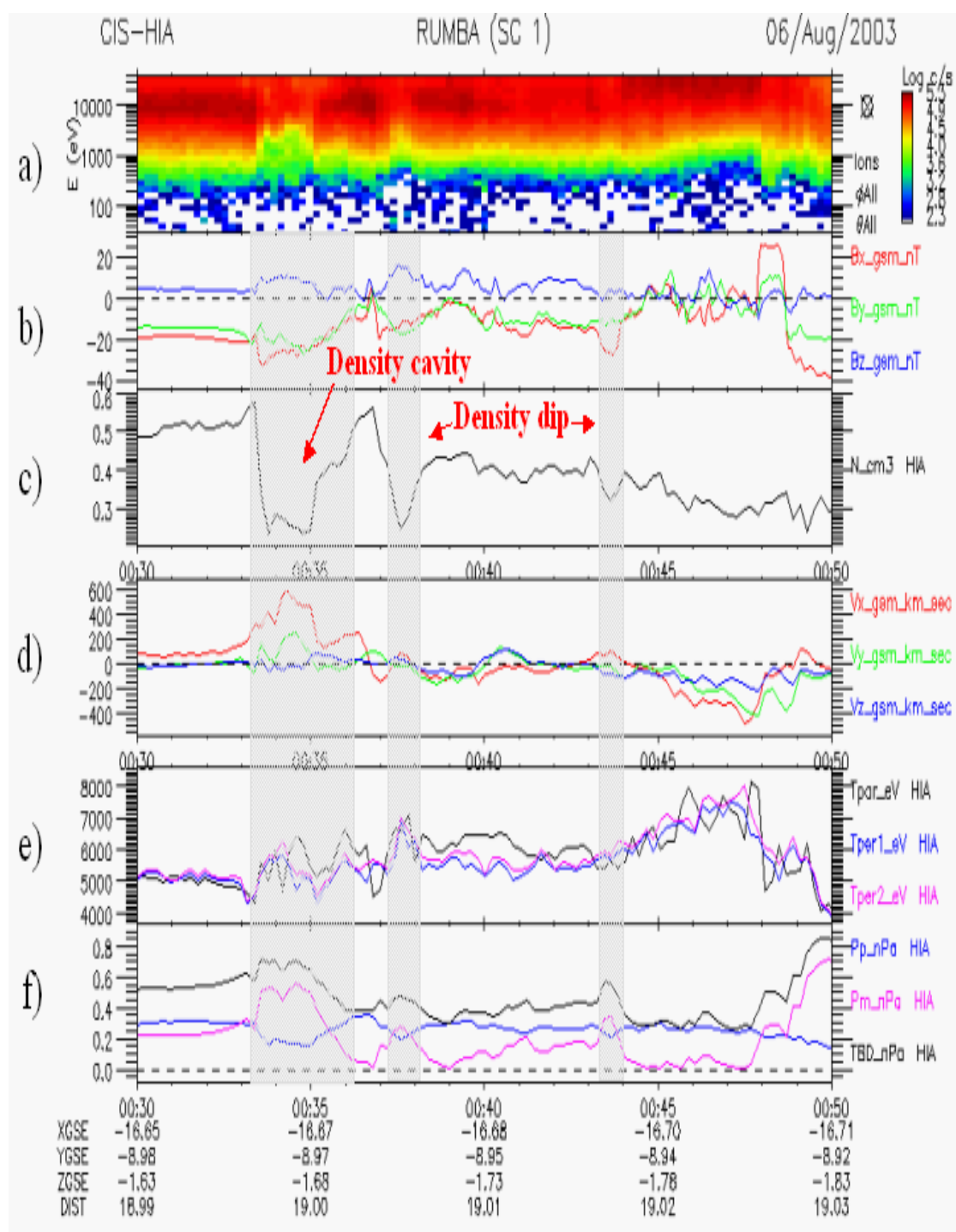


Fig.4.3 Magnetic field and hot ion measurements from C1. a) time-energy spectrogram, b) components of magnetic field, c) and d) hot ion density and bulk velocities in GSM coordinates respectively, e) hot ion pressure components parallel and perpendicular to the magnetic field, and f) magnetic pressure, plasma pressure and total pressure respectively. The shadows denote the density cavity and two density dips respectively.

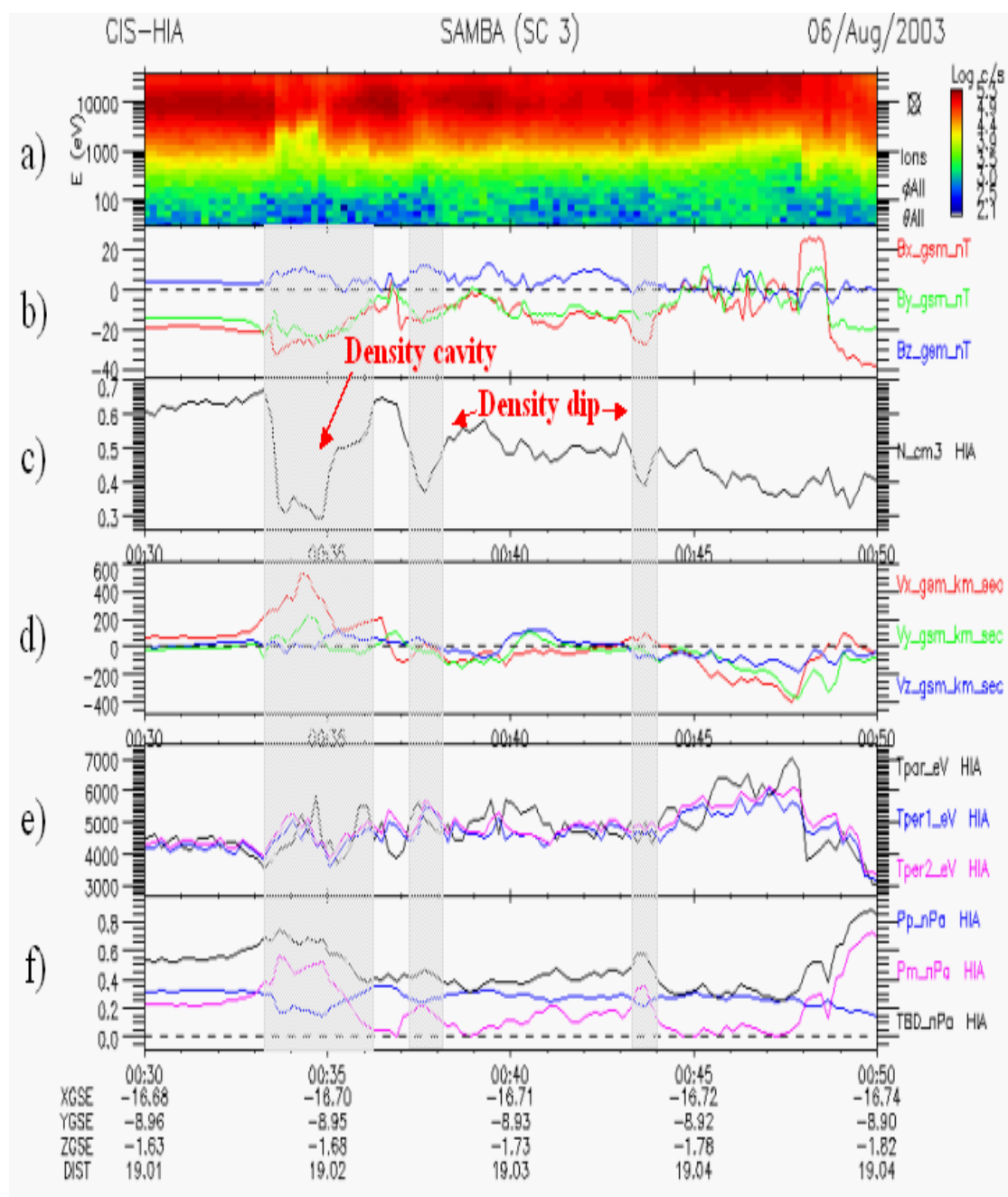


Fig.4.4 Magnetic field and hot ion measurements from C3. a) time-energy spectrogram, b) components of magnetic field, c) and d) hot ion density and bulk velocities in GSM coordinates respectively, e) hot ion pressure components parallel and perpendicular to the magnetic field, and f) magnetic pressure, plasma pressure and total pressure respectively. The shadows denote the density cavity and two density dips respectively.

measured very similar observational features. As shown in Fig.4.3 and Fig. 4.4 respectively, in the interval 00:33:20-00:35:10 UT, an earthward fast flow with a velocity up to  $\sim 590$  km/s in the GSM x direction was observed. Accompanied with this plasma ejection is a strong magnetic field variation. In this jet, both the density records from C1 and C3 decrease to nearly half of the original value, from  $0.5 \text{ cm}^{-3}$  to  $0.25 \text{ cm}^{-3}$  in Fig. 4.3 and from  $0.62 \text{ cm}^{-3}$  to  $0.32 \text{ cm}^{-3}$  in Fig. 4.4 respectively. Also, two density dips at 00:37:30 UT and 00:43:40 UT respectively were recorded by both C1 and C4.

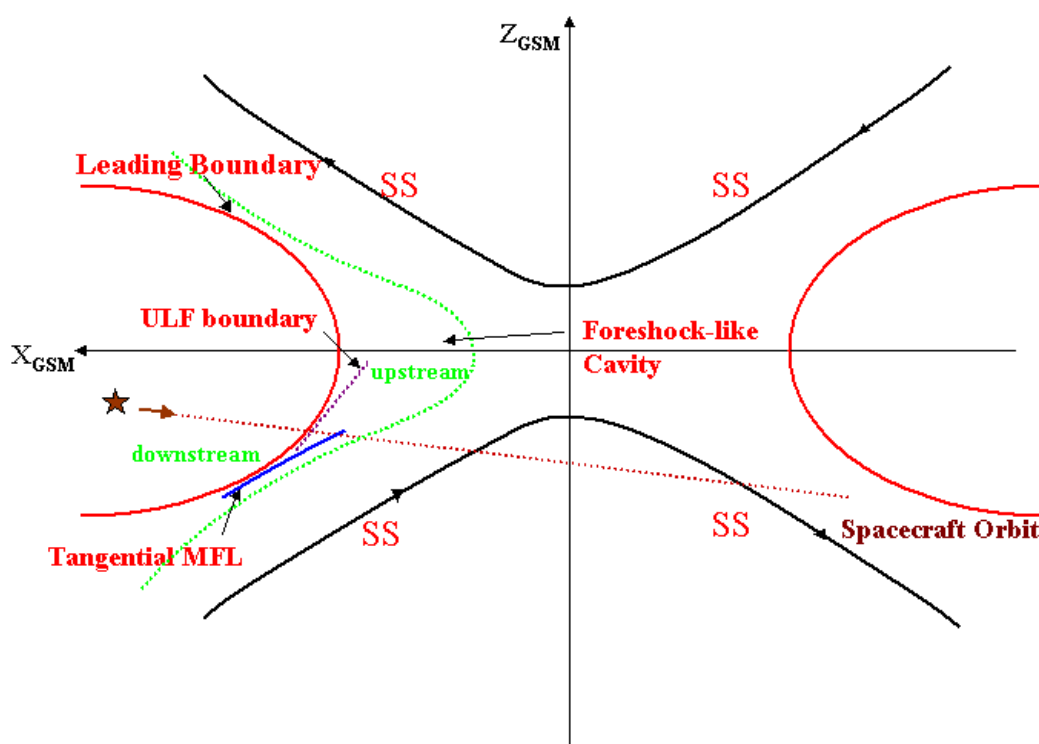


Fig.4.5 A schematic of the reconnection layer encountered by the spacecraft and boundaries in the cavity. The two black curves represent a pair of slow-mode separatrices. The dashed green line depicts the local magnetic configuration of field line piled up region. The red curve in the left-side describes the shock front, i.e., the sharp leading edge of ions jet. The blue line signifies the magnetic field line tangent to the quasi-perpendicular shock front. The star and the dashed brown line denote the spacecraft and its orbit. More details can be founded in the text.

## 2.2 The reconnection layer structure and the steepened leading boundary of the earthward jet

The present observation of fast ion jets is identified as a reconnection event, and the encountered reconnection layer is schematically shown in Fig.4.5. The nascent magnetic flux ropes can be carried out by the ion jet emanating from the diffusion region (Slavin et al., 2005). They are blocked by the original magnetic field lines bordering the outflow region and hence are piled up at the edge of outflow region. When the magnetic compression is intense enough, it is believed that plasma depletion phenomena usually take place due to pressure balance, and in most cases in association with some kind of singular boundaries. Here the earthward jet in the form of a density cavity with a sharp leading boundary is interpreted as exactly that case. In addition, this sharp leading boundary can be considered in principle as an MHD discontinuity or shock and hereinafter we refer to it as a shock. Here, the term “shock” is used in a rather general meaning, that is, if the front becomes steep enough that the entropy increases across it and the changes become irreversible, we refer to the front as a "shock" (Southwood and Kivelson, 1992).

By the magnetic field timing analysis, the normal direction and speed of the shock are estimated to be  $\mathbf{n}_{\text{GSM}}=(0.45, -0.01, 0.89)$  and 78 km/s respectively. The duration of its crossing is 14s. Hence its thickness is estimated to be 1100km, four times the proton inertial length. In the GSM frame, the magnetic fields upstream and downstream of the shock are  $\mathbf{B}_u=(-29, -23, 7)$  nT and  $\mathbf{B}_d=(-21, -16, 3)$  nT respectively. Therefore the angle between the magnetic field and the normal to the shock is about  $80^\circ$ , which means that the front encountered is a nearly proper perpendicular part of the shock. Moreover, we have approximately  $\Delta\mathbf{B} \cdot \mathbf{n} = 0$  and  $(\mathbf{B}_u \times \mathbf{B}_d) \cdot \mathbf{n} = 0$ , where  $\Delta\mathbf{B}$  is  $\mathbf{B}_u - \mathbf{B}_d$ , and hence verify the magnetic coplanarity. In addition, in the shock rest frame, the bulk velocities upstream and downstream of the shock are  $\mathbf{V}_u=(550, 242, -74)$  km/s and  $\mathbf{V}_d=(270, -130, -54)$  km/s respectively. Thus the calculated upstream and downstream normal velocities are 179 km/s and 75 km/s respectively. The ratio of the upstream normal velocities to the downstream normal velocity is about 2.4, while the

upstream and downstream densities are  $0.72 \text{ cm}^{-3}$  and  $0.33 \text{ cm}^{-3}$  respectively. The ratio of the downstream density to the upstream density is about 2.2. Hence the mass conservation is approximately satisfied. A lesser agreement is obtained for the full set of jump conditions. The reason is due to the non-stationarity behavior of this cavity because of the explosive reconnection jets. Taking into account this fact, the upstream parameters may be highly time-dependent. In addition, the calculated velocity of the ion jet includes the contribution from reflected backstreaming particles and should be less than the actual incident velocity. Therefore, although the calculated upstream normal velocity ( $\sim 179 \text{ km/s}$ ) is even smaller than the slow-mode speed, which is estimated to be  $\sim 250 \text{ km/s}$ , it seems reasonable that this leading boundary is identified as a time-dependent slow-mode transition layer.

It is worth noting that this leading boundary inside the outflow region that separates the accelerated plasmas from the original plasma should not be confused with the well-known Petschek-type slow-mode shock around the reconnection region since it moved earthward. Otherwise, it would not be the leading boundary of the jet and the bulk flow would be encountered first. Petschek (1964) proposed that the changes required as plasma flows into the field reversal region can be accomplished by two slow compressional waves placed back to back bounding the field reversal region. The waves propagate (with respect to the plasma) away from the field reversal region, but they are also convected toward it by the plasma flow. These two effects must balance in a steady state in which the waves must be stationary; thus the plasma flow speed toward the field reversal region must equal the wave propagation speed. Therefore, the field reversal region is bounded by a pair of slow waves that extend out from the diffusion region. Since these are compressional waves of finite amplitude, it is further proposed that they steepen and become slow shocks, as would be expected from the theory of finite amplitude MHD waves. Slow-mode shocks were first observed in the distant magnetotail based on ISEE-3 measurements (Feldman et al., 1984; Smith et al., 1984) and subsequently also reported in the near-Earth tail in conjunction with substorm events (Hones et al., 1986; Eriksson et al., 2004).

Density dips encountered in reconnection layers are usually identified as Petschek-type slow-mode separatrices (Cattell et al., 2005; Borg, et al., 2005). Here the two density dips encountered at 00:37:30 UT and 00:43:40 UT are regarded as the slow-mode separatrices bounding the earthward side and tailward side outflow regions respectively. Between the slow-mode separatrices, there is the southern inflow region. Thus nearly in the middle of this region at 00:40:30 UT, a peak of  $V_z$  was recorded as shown in the fourth panel in Fig.4.2, which is identified as the inflow velocity with speed up to  $\sim 200\text{km/s}$ .

It is worthy to note that in the intervals 00:36:40-00:37 UT and 00:47:50-00:48:30 UT, the spacecraft encountered the neutral line and the outer current sheet respectively due to the very rapid large-scale shift of the current sheet, which are phenomena frequently occurring in the thin current sheet and usually referred to as the flapping motion (Sergeev et al., 2003; Cai et al., 2008). The fifth panel in Fig.4.2 shows the components of the proton temperature. It can be seen that in both the earthward and tailward ion jets, the proton temperature rose, apparently due to the heating by both the magnetic diffusion and by the slow-mode separatrices.

### 2.3 Incident and backstreaming protons inside the cavity

The global morphology of the density cavity can be established from the observational characteristics of particle kinetics. Fig.4.6 gives the spectrogram of the pitch angle and azimuthal angle of protons recorded by C4 in 2 energy ranges. Similar measurements of hot ions recorded by C1 and C3 are shown in Fig 4.7 and Fig 4.8 respectively. As mentioned above, the proton measurements are from the CODIF sensor onboard C4, while the hot ion measurements are from the HIA sensors onboard C1 and C3 respectively because the CODIF sensors onboard C1 and C3 were switched off at that time.

In the cavity, from 00:34:05 to 00:34:44 UT as shown in the sixth panel in Fig.4.6, intense incident protons within energy range 1.5-40 keV in the anti-parallel magnetic

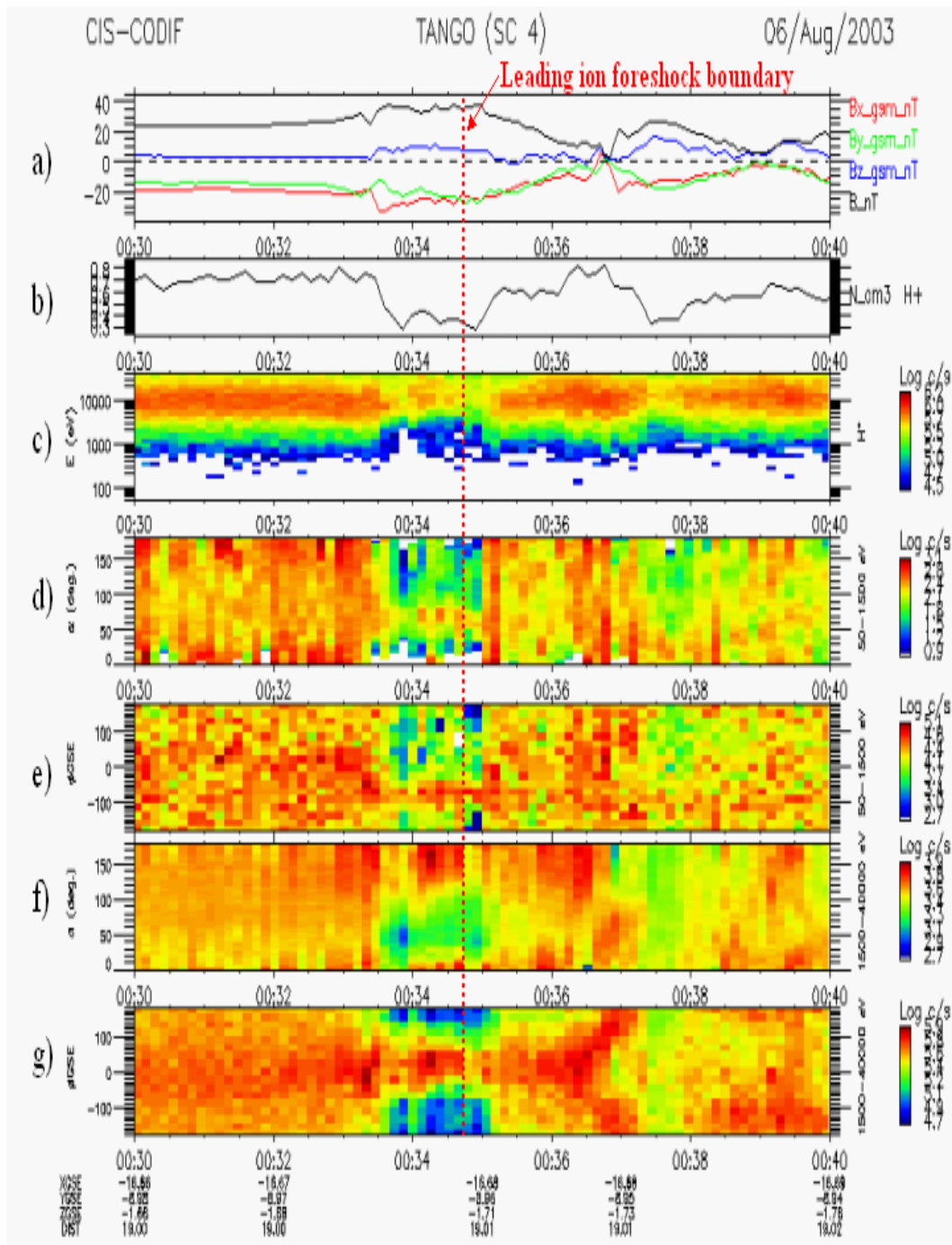


Fig.4.6 A snapshot of proton measurements in the cavity from the CODIF sensor onboard C4. The third panel is time-energy spectrogram. The fourth and fifth panels show spectrograms of pitch angle and azimuthal angle respectively for protons within the energy range 50-1500eV, and the sixth and seventh panels show those for protons within the higher energy range 1.5-40keV. A collimated backstreaming beam distribution in the parallel magnetic field direction can be found in panel f) of the pitch angle spectrogram within the higher energy range 1.5-40keV in the time interval 00:34:05 to 00:34:44 UT.

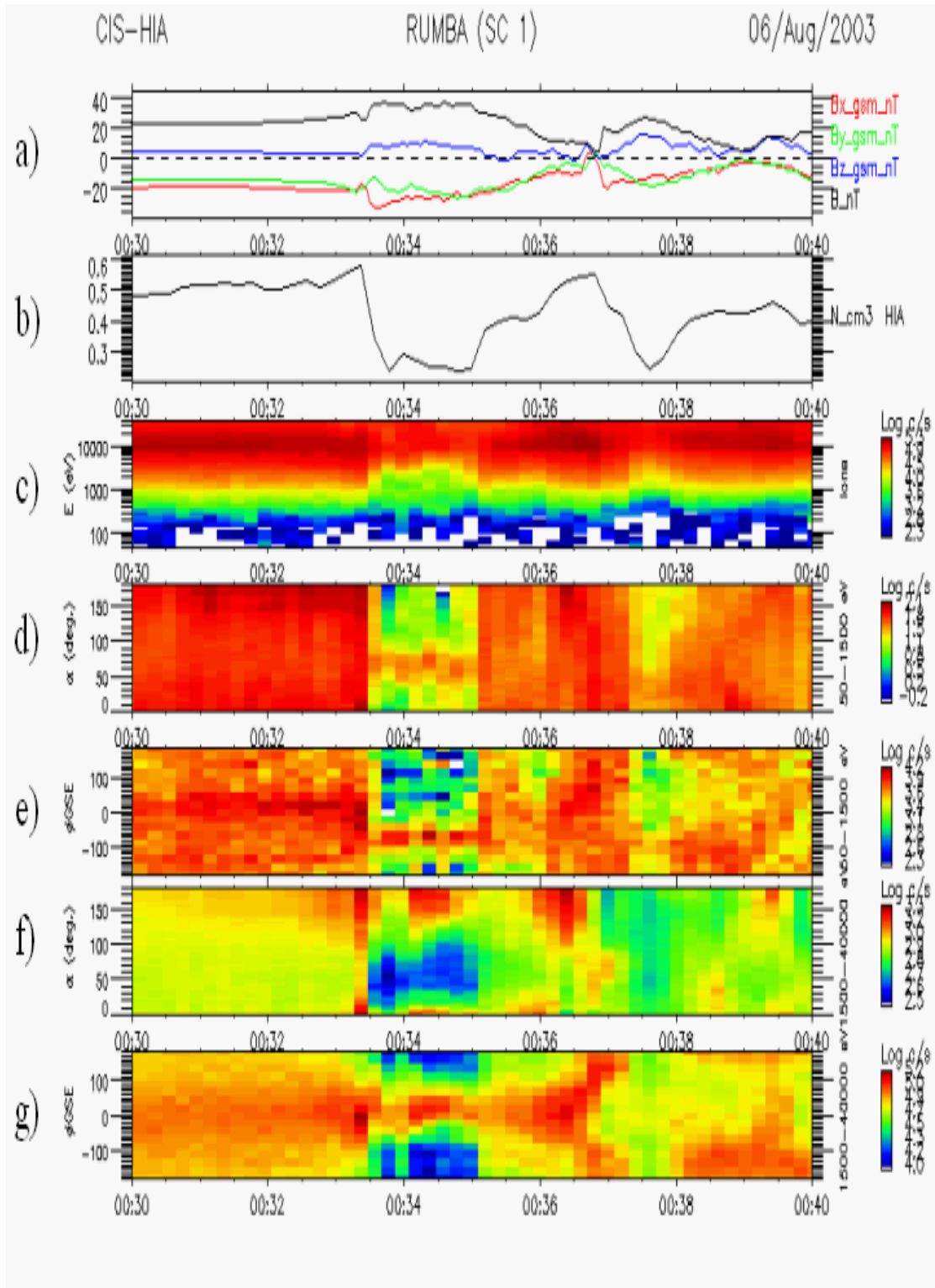


Fig.4.7 Hot ion measurements in the cavity from the HIA sensor onboard C1. The fourth and fifth panels show spectrograms of pitch angle and azimuthal angle respectively for hot ions within the energy range 50-1500eV, and the sixth and seventh panels show those for protons within the higher energy range 1.5-40keV.

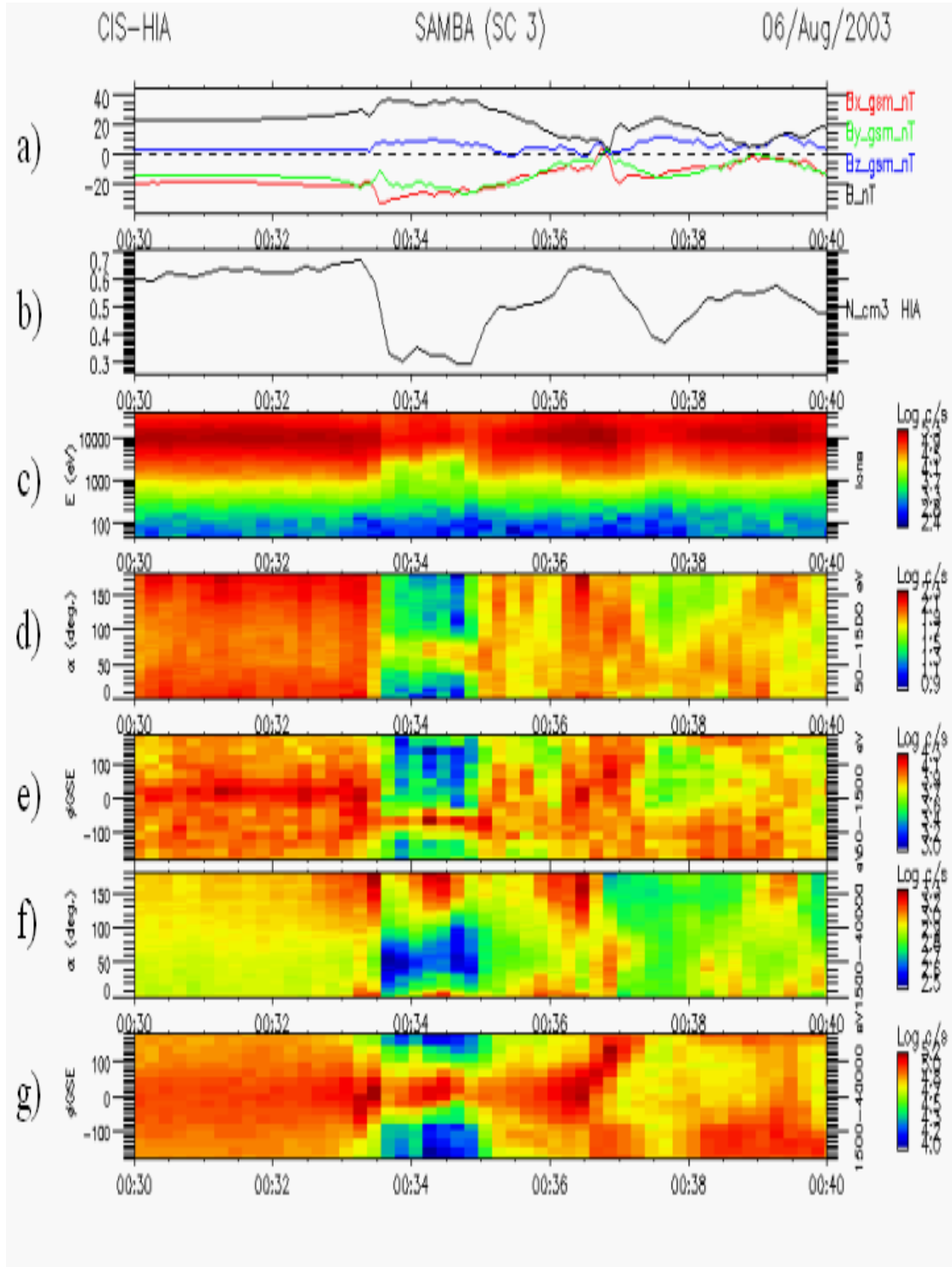


Fig.4.8 Hot ion measurements in the cavity from the HIA sensor onboard C3. The third panel is time-energy spectrogram. The fourth and fifth panels show spectrograms of pitch angle and azimuthal angle respectively for hot ions within the energy range 50-1500eV, and the sixth and seventh panels show those for protons within the higher energy range 1.5-40keV.

field direction were observed. Simultaneously, a very collimated backstreaming beam distribution in the parallel magnetic field direction was recorded. The fourth and fifth panels show the proton behaviors in the energy range 50-1500eV. It can be seen that in the cavity the pitch angles of these protons with lower energies display a narrow profile between  $50^{\circ}$  and  $70^{\circ}$ . Also, along the negative Y direction they are within an azimuthal angle profile centered between  $-80^{\circ}$  and  $-100^{\circ}$ . The backstreaming beam distribution in the parallel magnetic field direction from 00:34:05 to 00:34:44 UT in the cavity can be also seen in the panel of pitch angle spectrogram within the higher energy range 1.5-40keV in Fig.4.7 and Fig.4.8 respectively. In addition, the characteristics of hot ions with lower energies recorded by C1 and C3 is likewise similar to that of C4.

Fig.4.9 shows the proton distribution functions from C4 for all the twelve data acquisition periods in the cavity (Each ion data acquisition period is here two spacecraft spins, i.e. 8s). It isn't difficult to find that from the third period to the last one, all these distribution functions show an apparent loss-cone distribution in the direction parallel to the magnetic field. Fig.4.10 shows a sample of these distribution functions in the seventh period at 00:34:13 UT.

As mentioned above, the depleted density cavity, in association with a steepened leading boundary, is generated by the piled up magnetic field lines, which are carried out by the ions jet emanating from the diffusion region. The present scenario resembles highly the case that when the solar wind impacts the magnetosphere, a curved bow shock front forms. In contrast to the hydrodynamics shock, in which no information can be transmitted to upstream region, the existence of reflected particles back to the upstream region is an intrinsic feature of collisionless MHD shock. Here the observed collimated backstreaming beam is interpreted to be those reflected particles by the steepened leading boundary, that is, whose generation mechanism is exactly similar to that of the foreshock (Paschmann et al., 1980; Gosling et al., 1982, Schwartz et al., 1983).

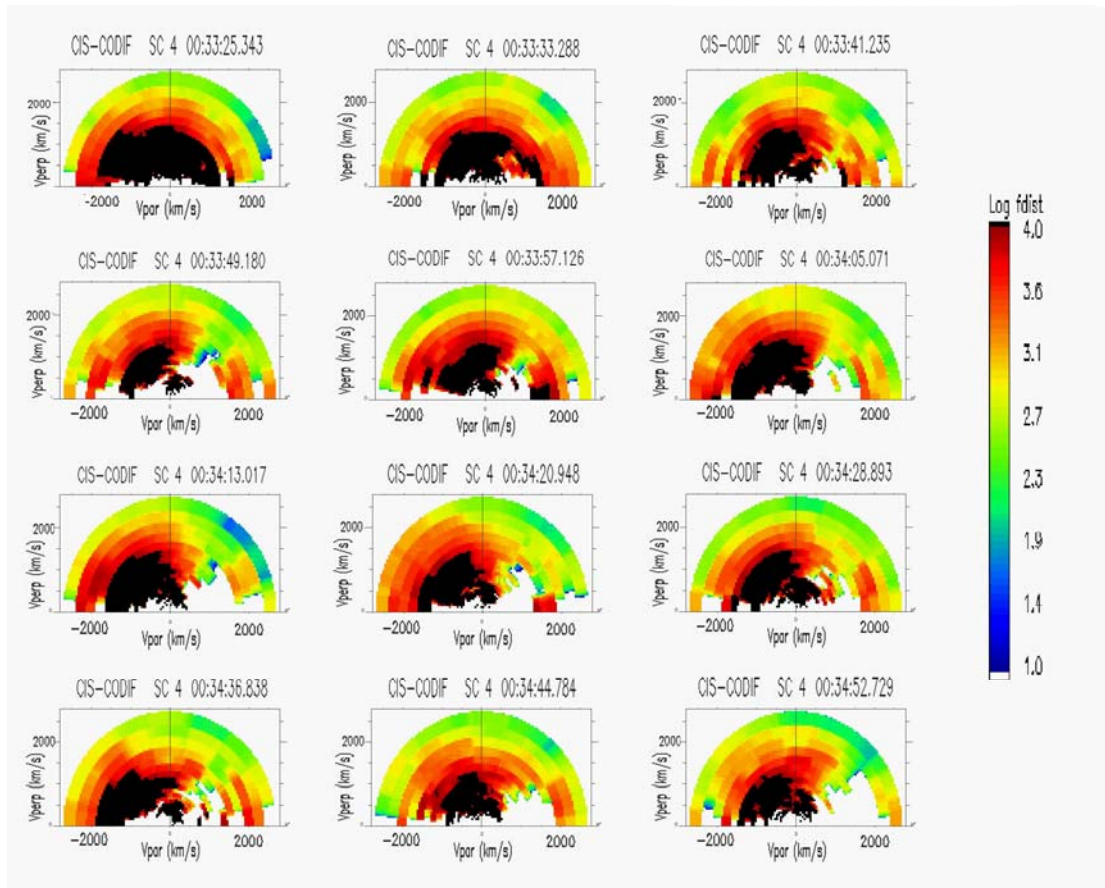


Fig.4.9 Proton distribution functions for all the twelve data acquisition periods in the cavity. The black masses are incident particles. From the third one, all these distribution functions show an apparent loss-cone distribution in the direction parallel to the magnetic field.

In Fig.4.5, a schematic is shown in which the blue line indicates the magnetic field line tangent to the perpendicular part of the curved shock front. The specularly reflected particles with high field-aligned velocity move both along the magnetic field line and simultaneously drift in the convective electric fields of the incident protons. Eventually, these backstreaming field-aligned beams can be found behind the tangential magnetic field line, along which they escape upstream from the shock front. In the present case, the leading ion foreshock boundary is encountered at 00:34:44 UT while the spacecraft crossed the foreshock region from downstream to upstream, thus no field-aligned ion beam was observed after this time.

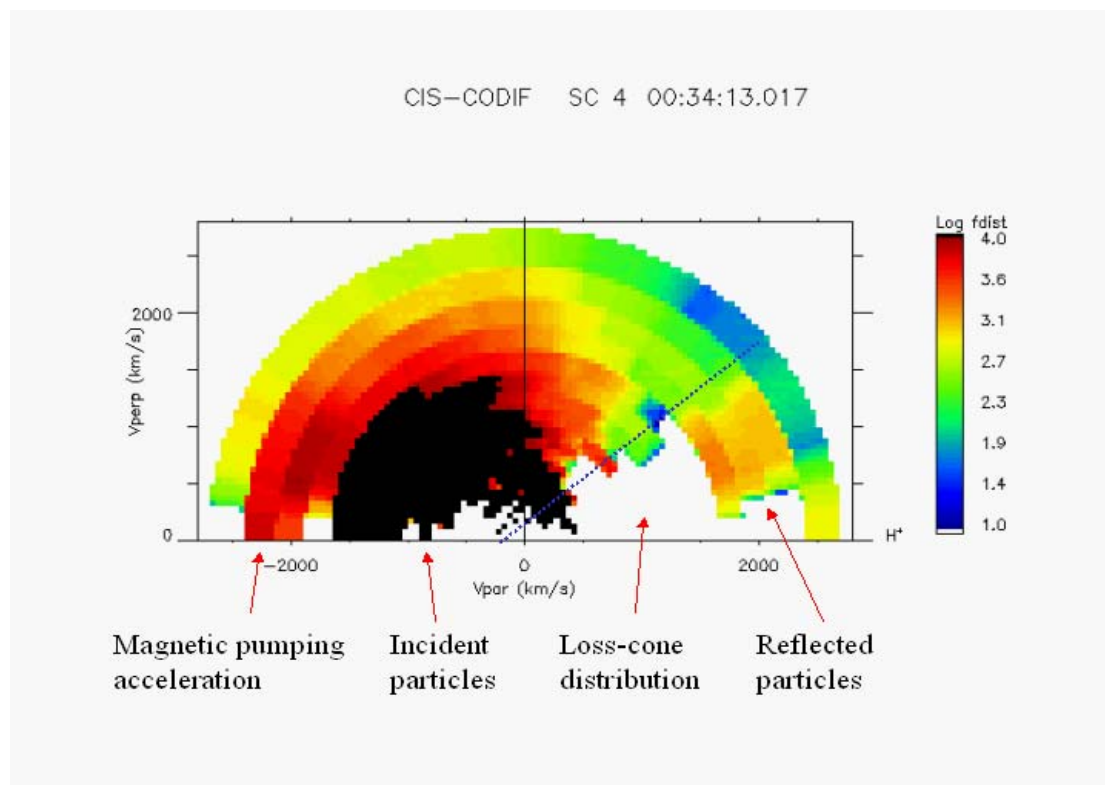


Fig.4.10 Proton distribution function in the sixth data acquisition period in the cavity at 00:34:05 UT. Several populations with different kinetic characteristics are identified. The feature of loss-cone distribution is lined out. The population which fills the edge of the loss-cone with a large parallel velocity is the specularly reflected field-aligned beam. On the most left, it is the accelerated incident population.

Table 4.1 Characteristic parameters and differences between the reconnection shock and the bow shock

	Reconnection shock	Bow shock
Type	Time-dependent slow-mode	Fast-mode
$V_{\text{upstream}}$	$\sim 600 \text{ km/s}$	$\sim 500 \text{ km/s}$
$B_{\text{upstream}}$	$\sim 40 \text{ nT}$	$\sim 5 \text{ nT}$
$n_{\text{upstream}}$	$\sim 0.4 \text{ cm}^{-3}$	$\sim 4 \text{ cm}^{-3}$
$V_{\text{Alfven}}$	$\sim 650 \text{ km/s}$	$\sim 50 \text{ km/s}$
Larmor radius	$\sim 400 \text{ km/s}$	$\sim 90 \text{ km/s}$
Thickness(perp)	$\sim 3$ Larmor radius	$\sim 3$ Larmor radius

One issue of the interpretation of the reconnection outflow region as analogous to the bow shock-foreshock region must be clarified here. For the bow shock, it is a fast-mode type, while in the present case the sharp boundary is a slow-mode shock based on the above investigation. Characteristic parameters and differences between the reconnection shock and the bow shock are shown in Table 4.1. However, whatever the shock is, the crucial point is that in both cases a steepened current sheet is generated and can act as a reflecting layer. The interpretation of the generation mechanism of those field-aligned backstreaming particles in the cavity is a natural explanation.

Apart from the specularly reflected particles, there are also other populations flowing back upstream of the shock by magnetic mirroring or in any other way. For example, several populations can be identified in Fig.4.10. The loss-cone is the most prominent characteristic in this distribution due to magnetic mirroring. The population which fills the edge of the loss-cone with a large parallel velocity is the specularly reflected field-aligned beam. Moreover, there are two populations of incident protons: the major population has lower velocity, the minor population has higher velocity. Compared with the distributions in the other periods, we can infer that the population with lower velocity is the normal incident particles, while the population with higher velocity is apparently accelerated. It demonstrates the possibility that the incident particles can be further energized in the field line piled up region in the outflow region of reconnection, especially in the case that the singular boundary condition occurs. The energisation mechanism here is supposed to be a Fermi-type, which is the acceleration that charged particles undergo when reflected by a magnetic mirror, as well as a transit time magnetic pumping, which is an acceleration or heating process operating in temporally changing magnetic fields in the presence of particle scattering. Therefore, it provides another possible acceleration mechanism for the particles in their multi-step acceleration processes in the reconnection (Imada et al., 2007).

#### 2.4 ULF waves in the cavity

The presence of intense low frequency electromagnetic fluctuations is an inherent feature of the ion foreshock region (Eastwood et al., 2002, 2004). ULF waves in association with backstreaming diffuse ion distributions are usually observed deep into the ion foreshock region, approaching to the quasi-parallel shock front (Bame et al., 1980, Meziane et al., 2001, 2004, Cao et al., 2009, Fu et al., 2009). Those ULF waves are believed to be generated by the backstreaming field-aligned beams, and the beams then become diffused. The upstream boundary of the ULF wave activity region is commonly called the ULF foreshock boundary or the ion foreshock wave boundary. Thus this boundary is between the backstreaming field-aligned beam distributions and diffuse distributions in the ion foreshock.

Fig.4.11 shows a snapshot of the magnetic field measurements with 1s time resolution and the proton density in the cavity. The red, gray and blue shadows denote respectively the time intervals of the shock ramp, ULF waves and the backstreaming field-aligned beam. Both the leading edge and the ULF wave boundary of the ion foreshock can be identified from the time sequence of proton and magnetic field observations. It is important to note that in the interval of the shock ramp, a bipolar structure of  $B_y$  was recorded. This particular feature gives a trusty evidence of the existence of a strong surface current in the shock front, which is regarded to result from the decoupling of the ion motion with the electron motion due to the finite Larmor radius effect (Bale et al., 2005). Meanwhile, the decoupling of the ion motion with the electron motion can cause intense electrostatic fields in the shock surface. It is just those strong electrostatic fields that are believed to be responsible for the generation of the reflected field-aligned proton beams described in the previous section. Therefore, the observational particulars of particles and electromagnetic fields in the present event are mutually justified.

Shortly after the shock ramp, ULF wave activity was observed in the interval 00:33:40-00:34 UT. Especially, in the second panel, a quasi-monochromatic  $B_x$  oscillation was found. Its period is about 9s, while the period of the fast magnetosonic

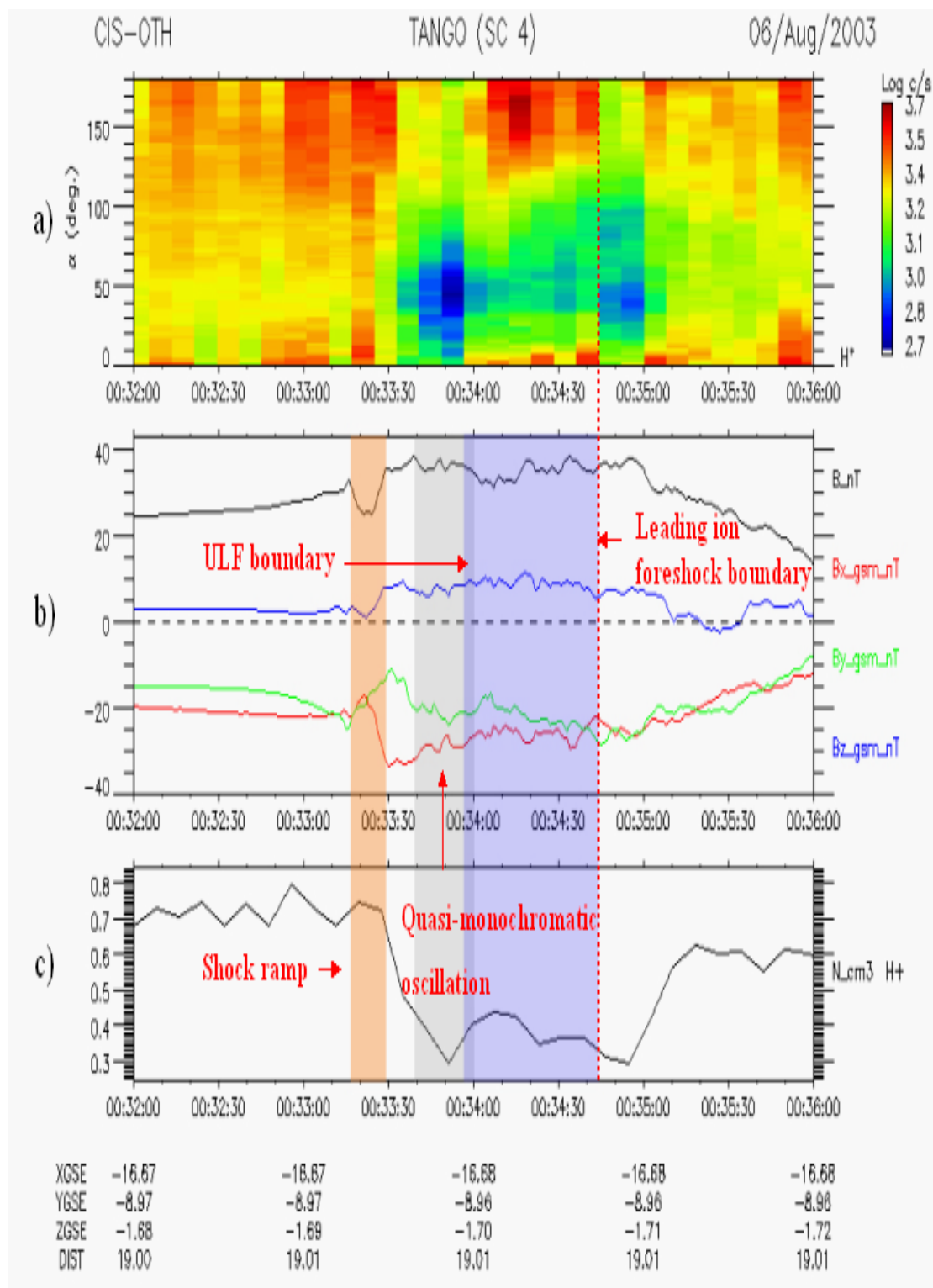


Fig.4.11 A snapshot of magnetic field measurements with 1s time resolution and proton density in the cavity from C4, where the ion measurements are from CODIF sensor. The red, gray and blue shadows denote respectively the time intervals of the shock ramp, ULF waves, and the backstreaming field-aligned beam.

waves upstream the bow shock is typically about 30s (Eastwood et al., 2002, 2004). Also, just after the ULF wave region, the ion foreshock was encountered. It can be seen that the wave observations are well coincident with the particle kinetic measurements. The field-aligned beam distributions were not observed in conjunction with ULF waves, and the time gap between the ULF boundary and the backstreaming field-aligned beam distribution is less than one ion data acquisition period. Of course, in addition to the quasi-monochromatic ULF waves, intense higher frequency magnetic field turbulences can be found in the entire foreshock region including downstream of the shock front.

### 2.5 Backstreaming electrons in the cavity

Fig.4.12 shows three selected electron distributions parallel, anti-parallel and perpendicular to the magnetic field from the PEACE experiment (Johnstone et al., 1997) onboard C4. The first and second distributions parallel to the magnetic field show a global enhancement, which represents a broad type of bump-on-tail pattern, that is, the flux parallel to the magnetic field (green curve) shows an increase in a rather broad energy regime. While the third electron distribution parallel to the magnetic field has a narrower bump compared with that of the first and second distributions, which we refer to as a narrow type of bump-on-tail pattern. The distributions recorded in other periods in the cavity have not obvious variation and are thus not shown here.

The two type bump-on-tail distributions are interpreted as the reflected electrons by the specular reflecting mechanism. However, the difference in their manifestations reveals the difference in their microscopic physics of reflecting process. The narrow bump is caused by the electrons suffering a reflecting process that has a very short interaction time with the front, that is, interact only with the shock precursor and cannot reach the ramp itself. Furthermore, there is a second class of backstreaming electrons, which succeed to penetrate deeper the front and interact with the ramp (Lembège and Savoini, 2002). In this case, the trapped electrons can gain sufficient

energy, including the parallel energy, from the shock electrostatic field while they excursion along the shock front. Corresponding to the two types of electron reflecting mechanisms, as revealed in simulations, there are two types of electron distributions parallel to the magnetic field, the narrow type of the bump-on-tail pattern and the broad type (Savoini and Lembège, 2001). The narrow type corresponds to the reflecting population that has lower parallel velocity, while the broad one corresponds to electrons that spend some time interacting with the macroscopic fields at the shock front and thus have higher parallel velocity. What kind of distribution can be found in the foreshock depends on the relative location of the shock geometry, and sometimes both types can coexist at the same location.

The narrow type of bump-on-tail pattern represents the population in the electron foreshock in a conventional meaning, that is, similar to the backstreaming field-aligned ions, backstreaming field-aligned electrons will also move along the magnetic field line and simultaneously drift in the convective electric fields, but within a smaller distance. It is coincident with the fact that these reflected electrons were observed at 00:34:54 UT, shortly after the passing of the leading ion foreshock boundary when the spacecraft crossed the foreshock region from downstream to upstream. However, the broad type of bump-on-tail pattern was observed within the two consecutive spin periods at 00:33:31 UT and 00:33:35 UT respectively, very close to the shock front. They are the second class of backstreaming electrons mentioned above, that is, electrons that interact with the ramp for a much longer time and gain more energy. This measurement gives evidence on the difference in their microscopic physics of reflecting process. It also indicates the remarkable impact of the local shock geometry on the electron kinetics. For the proper perpendicular part of the shock with a larger angle between the shock normal and the magnetic field direction, the electrons suffering a reflecting process that has a very short interaction time with the front. In contrast, for the quasi-perpendicular part with a smaller angle, the shock electrostatic field will make its contribution to the electron dynamics via local trapping and acceleration (Lembège et al., 2004).

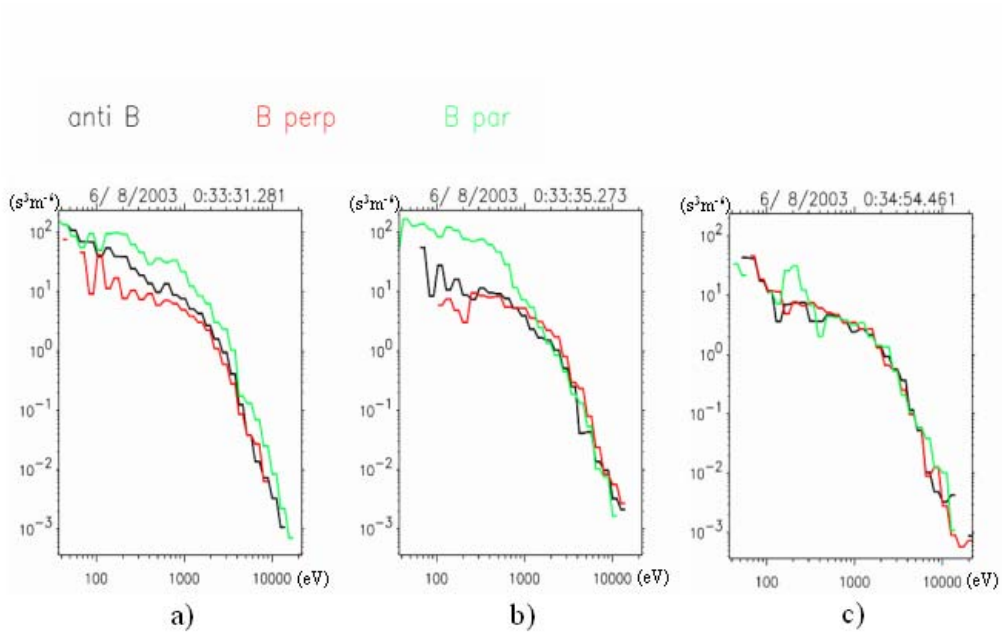


Fig.4.12 Selected electron distributions parallel, anti-parallel, and perpendicular to the magnetic field in the cavity from C4. The first and second distributions parallel to the magnetic field manifest the broad type of bump-on-tail pattern, while the third distribution shows the narrow type of bump-on-tail pattern.

### 3. Discussion and conclusion

We first give a summary on the morphology of the density cavity, which is analogous to the foreshock region. During the interval 00:33:16-00:33:30 UT, the spacecraft crossed the shock front from the downstream to the upstream. Just close to the front, in two consecutive spin periods at 00:33:31 UT and 00:33:35 UT respectively, reflected electron distribution with a broad type of bump-on-tail pattern was observed. Then in the interval 00:33:40-00:34:00 UT, ULF waves, especially a quasi-monochromatic  $B_x$  oscillation, were recorded. Just passing the ULF boundary, in the interval 00:34:05-00:34:44 UT, specularly reflected field-aligned proton beams were measured. Shortly after the passing of the leading ion foreshock boundary, corresponding to the spin period at 00:34:54 UT, specularly reflected field-aligned

electrons, whose distribution has a narrow type of bump-on-tail pattern, were detected. Moreover, magnetic-mirror loss-cone proton distributions in the cavity were observed. Since the spacecraft had crossed both the left-side and the right-side outflow regions, a question arises: why it didn't observe the same thing on the right-side? There are two possible reasons. The first is that in comparison to the situation of flowing earthward, it is easier for the ion jet to push away its barrier while flowing tailward. The second is possibly due to the particular interaction manner of the reconnection jets with the rest plasma, that is, the jets are explosive and are bounded by a narrow slow-mode shock pair as mentioned above. Hence the shock and its accessories, if they can be generated at the edge of jets, will be localized both in space and time.

In addition, it is interesting to interpret the foreshock-like cavity in the viewpoint of a coherent structure. In the previous investigations, some transient structures such as hot diamagnetic cavities, foreshock cavities and short large-amplitude magnetic structures, have been reported in the upstream regions of the Earth's bow shock. Recently, the Cluster and Double Star satellites observed intense plasma density holes, with a characteristic dimension of ion gyroradius, upstream of the bow shock (Parks et al., 2006). Likewise, much attention has been paid on the coherent structures in the reconnection region, especially those electrostatic coherent structures in the diffusion region.

Large-amplitude solitary waves, identified as electron holes, have been observed during the passage of a magnetotail reconnection neutral line. These electron holes were generated near the outer edge of the plasma sheet, within and at the edge of a density cavity, at distances on the order of a few ion inertial lengths from the center of the current sheet (Cattell et al., 2005). These density cavities accompanied with electron holes can also be found in computer simulations (Drake et al., 2003). Therefore, large-scale coherent structures such as density cavity, which usually have a characteristic scale on the ion inertial length, seem to be an organic part of the reconnection and closely relevant to the small-scale electrostatic coherent structures. Coherent structures are usually responsible for those nonlinear microphysics in space

plasma environment. For example, the electron holes are believed to participate in the electron energisation process (Drake et al., 2005). The present analysis shows that the density cavity can also act as the accelerator for ions to provide further acceleration. Our investigation here gives an insight into the significant role played by the self-organized larger-scale coherent structures in the collisionless magnetic reconnection region. The results of this chapter have been published in Cai et al., 2009b.

## Chapter 5

### Observations of Thin Current Sheet (TCS) in the Magnetotail

#### 1 Introduction

The understanding of dynamics of the magnetotail current sheet is important to many space phenomena. The conventional current sheet model is based on the Harris equilibrium, which has the well-known tanh-type magnetic field profile and the bell-shaped density and current profile, that is, current and plasma densities have a simple profile with a single peak in the center of the sheet where the magnetic field has a minimum (Harris, 1962). The Harris equilibrium is in a good agreement with the observations of the thick quiet time current sheet (Fairfield, 1979, Thompson et al., 2005). However, Thin Current Sheets (TCS), whose thicknesses are on the order of ion gyroradius or inertial length, were reported recently by numerous studies (Sergeev et al., 1993, Hoshino et al., 1996, Runov et al., 2003a, 2005, Sergeev et al., 2003). Behaviors of TCS were significant deviated from the Harris's equilibrium. Observations revealed that in some instances, TCSs have a manifestation of embedding, which means that TCSs with rather large current densities are embedded into a much thicker current sheet, and the thicker current sheet is usually in accord with a Harris equilibrium. In some other cases, TCSs have a bifurcated structure, that is, TCSs commonly have a double-peak, sometime multi-peak, current profile, and the current density has a minimum at the center of the sheet. TCSs are frequent phenomena in the magnetotail and hence raise a question on the interpretation of their formation and evolution (Asano et al., 2005).

Many theoretical models were attempted to describe the TCS structures and dynamics. In one category, an isotropic pressure is assumed. These models either choose the

particle distributions to be a function of two invariants of motion, namely the total particle energy and the component of the canonical momentum along the current direction, as in the Harris model but in their generalized non-Maxwellian forms, or adopt equivalently the Grad-Shafranov equation, in which the current density is a function of the electromagnetic field vector potential (Schindler et al., 2002, Mottez, 2003, Birn et al., 2004a, Genot et al., 2005, Camporeale et al., 2005). Therefore, it implies that in all of them, the pressure is isotropic, and the equilibrium is maintained by a balance between the field line tension and the plasma pressure gradient. In the other category, an anisotropic pressure is supposed, hence the equilibrium is achieved for one-dimension current sheet only if the magnetic tension is balanced by the tension due to the anisotropic pressure, namely the finite ion inertia (Eastwood, 1972). It was pointed out that in this case the current is confined to a thin layer, in which the particle motion may strongly differ from Larmor rotation, i.e., the particle dynamics does not obey the conventional guiding center theory, when its gyroradius becomes comparable to either the current sheet thickness or the curvature radius of the magnetic field. Behavior of these nonadiabatic ions is known as the Speiser motion (Speiser, 1965). Nonadiabatic ions including Speiser ions, quasi-trapped and trapped ions play an important role in the current sheet dynamics, and their kinetics in the TCS has been investigated intensively (Chen, 1992, Delcourt et al., 2004, 2006, Birn et al., 2004b). Moreover, when the current sheet is thin enough to obey some appropriate conditions, an integral of motion, the so-called quasi-adiabatic sheet invariant can be introduced (Sonnerup, 1971). Recently, a stationary state Vlasov theory involved the quasi-adiabatic sheet invariant was proposed to describe the TCS (Sitnov et al., 2000, 2003, 2006). Choosing the distribution of counterstreaming beams in the outer of the sheet, the numerical results show that a bifurcated current sheet appears in the case of ion anisotropy with  $T_{\perp} > T_{\parallel}$ ; while in the opposite case a single-peak current sheet embedded in a thicker Harris current sheet appears.

In addition, TCS is frequently found in association with rapid large-amplitude magnetic variations, namely flapping motion indicating rapid crossings through

up-down oscillating current sheet (Sergeev et al., 2003, Runov et al., 2003a, 2005). The flapping motion was identified to be a kink-like wave propagating in the current sheet direction. Statistical investigations revealed its particular propagating features. The propagating speeds are in the range of several tens km/s up to 200km/s. The propagating direction is flankward, that is, dawnward in the dawn sector and duskward in the dusk sector (Sergeev et al., 2004, Zhang et al., 2005). As pointed out, the wave properties do not match any local excitation mechanism previously discussed in the literature (Zhu et al., 1996, Daughton, 1999, 2002, 2003, Lapenta et al., 2002). It raises another question to understand the dynamics of TCSs.

Here, TCS dynamics is reported from observations during the Cluster spacecraft crossing of the magnetotail on September 15, 2001. First, an overview of the entire event, including the spacecraft configuration and characteristic parameters, is presented. Then various manifestations of TCSs in association with their ion anisotropy and nongyrotropy as well as their flapping motion are analyzed. Finally, discussion and summary are given.

## 2. Observations

### 2.1 Overview

Fig.5.1 shows the solar wind parameters from ACE in the time interval UT 00:00-06:00 on September 15, 2001. During this period, the IMF Bz was mainly northward, turned southward shortly at about UT 03:20 and during UT 04:30-05:00, and again shortly southward at about UT 05:30. After UT 03:00, the solar wind density apparently decreased from  $20 \text{ cm}^{-3}$  to  $7 \text{ cm}^{-3}$ , in association with an increase of the velocity from 460 km/s to 520km/s. Correspondingly, the plasma pressure decreased from 7 nPa to 3 nPa. A substorm was observed during UT 00:00 –00:50, which the AL index was up to -700 nT and then decreased to zero. The geomagnetic activity started again at UT 03:40. During the interval of UT 03:30-06:30, several auroral activations were registered by two geostationary satellites, GOES 8 and GOES

10 (Voronkov et al., 2006).

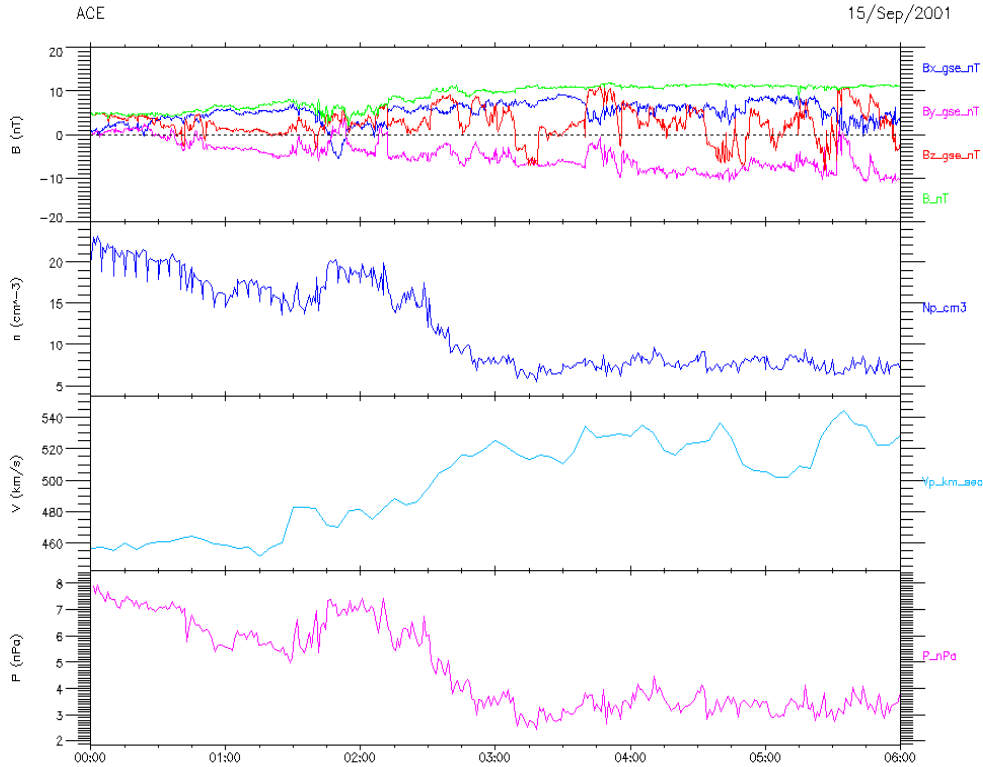


Fig. 5.1 Solar wind parameters from ACE.

The configuration of Cluster tetrahedron in the period UT 04:40-05:10 is shown in Fig.5.2. The characteristic scale of the tetrahedron is 1700km. It is worthy to notice that in the x-z plane, C3 is southmost and the other three satellites have small distances among them in the z-direction; all four satellites are in the dusk sector and in the y-z plane C2 is outermost. Characteristic parameters of the background plasma and fields in this event are  $T_H=2\text{keV}$ ,  $T_O=20\text{keV}$ ,  $B_0=30\text{nT}$  and  $n_i=0.5\text{cm}^{-3}$ , where  $T_H$  and  $T_O$  are the temperatures of proton and oxygen ions respectively,  $B_0$  is the magnetic field in the periphery of the plasma sheet and  $n_i$  is the total ion density. Thus, we have approximately  $\rho_H=220\text{km}$ ,  $\rho_O=2500\text{km}$  and  $c/\omega_{pi}=320\text{km}$ ,

where  $\rho_H$  and  $\rho_O$  are the gyroradius of proton and oxygen ions respectively and  $c/\omega_{pi}$  is the ion inertial length. The characteristic scale of the Cluster tetrahedron is comparable to the oxygen ion gyroradius and is almost five times the ion inertial length.

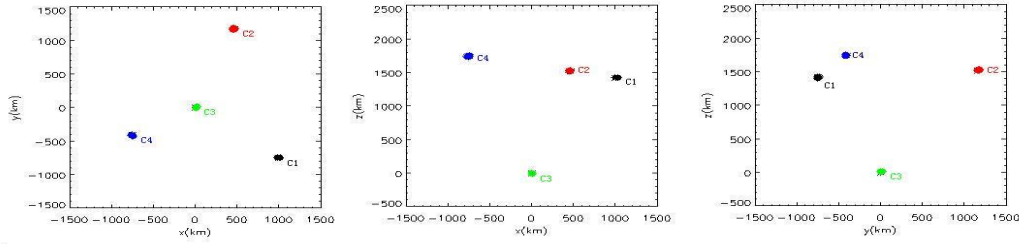


Fig.5.2 The configuration of Cluster tetrahedron in the time interval UT 04:40-05:10 on September 15, 2001.

Fig.5.3 shows the components of magnetic field from FGM experiment (Balogh et al. 2001) and the proton and oxygen ion densities from CIS-CODIF instrument (Rème et al., 2001). As represented by the whole shaded region in the interval UT 04:36-05:01 in Fig.5.3, all four satellites recorded a bell-shaped plasma density and current profiles, whose peaks are corresponding to the minimum of magnetic field. Hence it is indicated that a Harris-like current sheet was encountered. C1, C2 and C4 crossed almost simultaneously the central line at UT 04:48, as labeled by a vertical line, due to a global flapping motion of the bulk current sheet. A little later C3 crossed the central line at UT 04:50. However, compared to the Harris-like equilibrium with a larger thickness, in the interior of the thick sheet as shown by the narrow red shading, distinct manifestations of localized thin current equilibrium are encountered. Approximately in the interval UT 04:55-04:59, a thin proton dominated current sheet

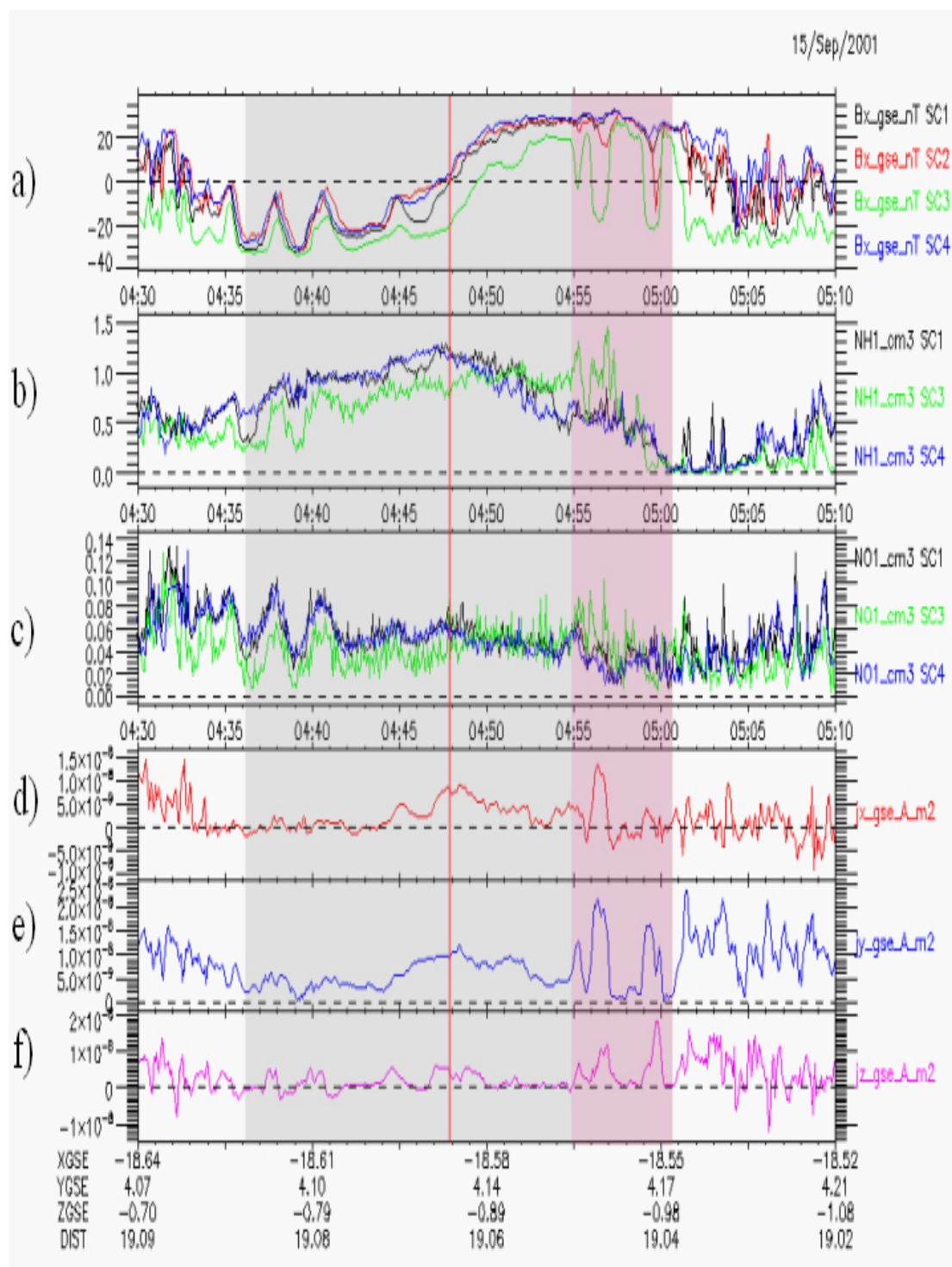


Fig.5.3 Overview of the Harris-like current sheet. a)  $B_x$  for the four Cluster satellites. b) and c) are the proton and oxygen ion densities respectively for C1, C3 and C4. d)-f) are the current density components. The shading region in the interval UT 04:36-05:01 denotes a Harris-like current sheet, whose central line is labeled by a vertical line at UT 04:48.

embedded into the southern part of the thick sheet was observed by C3. In addition, nearly in the time interval UT 04:58-05:00, a bifurcated thin oxygen ion current located in the northern part of the thick sheet was observed by C1 and C4. Here, it is worthy to notice that a plasma depletion layer was subsequently generated inside the plasma sheet. It can be seen that in the second panel in Fig.5.3, C3 at 04:59:00 and C1 and C4 at about 05:00:20, all of them observed a density decrease nearly to zero till 05:05:20.

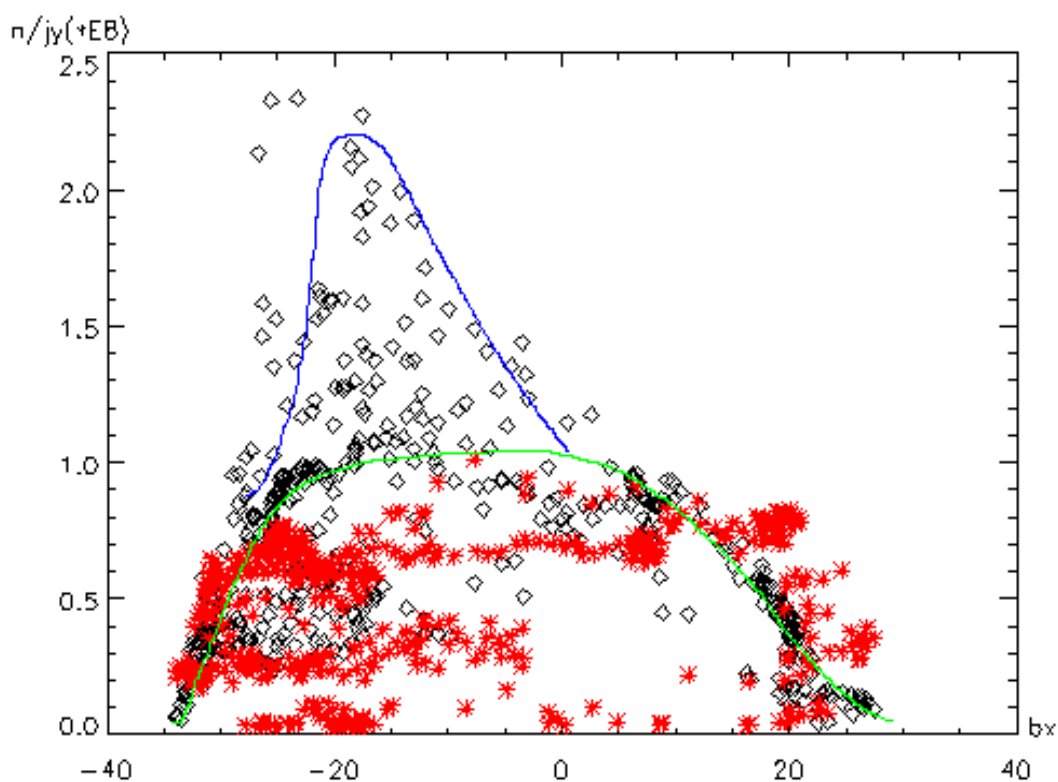


Fig.5.4 The scattering plot of the current density together with the proton density versus  $B_x$ . The red stars represent the proton density, and the black squares denote the current density in the y-direction (it is the average current density inside the satellite tetrahedron and is multiplied by a factor  $10^8$ , the units of current and ion density are  $A/m^2$  and  $cm^{-3}$  respectively). The green curve describes a fitting of the thick Harris-like current sheet, and the blue one depicts a fitting of the thin current sheet.

## 2.2 TCS embedding

The embedding feature of the proton dominated TCS was revealed in the scattering plot of the y-component of the current density (the total current density profile is similar to its y-component) together with the proton density versus  $B_x$ . As shown in Fig.5.4, the red stars represent the proton density, and the black squares denote the current density in the y-direction (it is the average current density inside the satellite tetrahedron and is multiplied by a factor  $10^8$ , the units of current and ion density are  $A/m^2$  and  $cm^{-3}$  respectively). The green curve describes a fitting of the thick Harris-like current sheet, and the blue one depicts a fitting of the thin current sheet. It can be seen that the two current profiles are distinct, the peak of green curve contained by the peak of blue curve. The ion density profile has a width that is roughly equal to that of the wider current profile. Hence the situation here is just the manifestation of the TCS embedding, which means that a thin current sheet with large current density is embedded into the southern part of a wider current sheet.

In the time interval UT 04:55:40-04:58:30, as shown by the shading in Fig.5.5, C3 measured continuously an anisotropic but gyrotropic pressure with  $p_{\parallel} > p_{\perp}$  for protons, while at the rest time it observed an apparent isotropic pressure. Simultaneously, the oxygen ion pressure was also nearly isotropic with negligible fluctuations. Fig.5.6 shows selected proton distribution functions at the beginning, the middle and the end of this period. All of them exhibited an apparent field-aligned beam distribution. It is worthy to notice that although a strong pressure anisotropy existed here, it still didn't achieve  $p_{\parallel} / p_{\perp} > 1 + 2 / \beta_{\perp}$ , which is the critical condition for exciting the firehose instability (Hasegawa, 1975). As pointed out by comparing the current distribution in the outer and in the center of the sheet, the current carried by a field-aligned beam satisfying the marginal firehose stability condition has a strong tendency to become thin, till a non-adiabatic current layer is formed (Eastwood, 1972, Cowley, 1978). Namely, when there is pressure anisotropy caused by field-aligned beams with  $p_{\parallel} > p_{\perp}$ , the current sheet should become an embedded

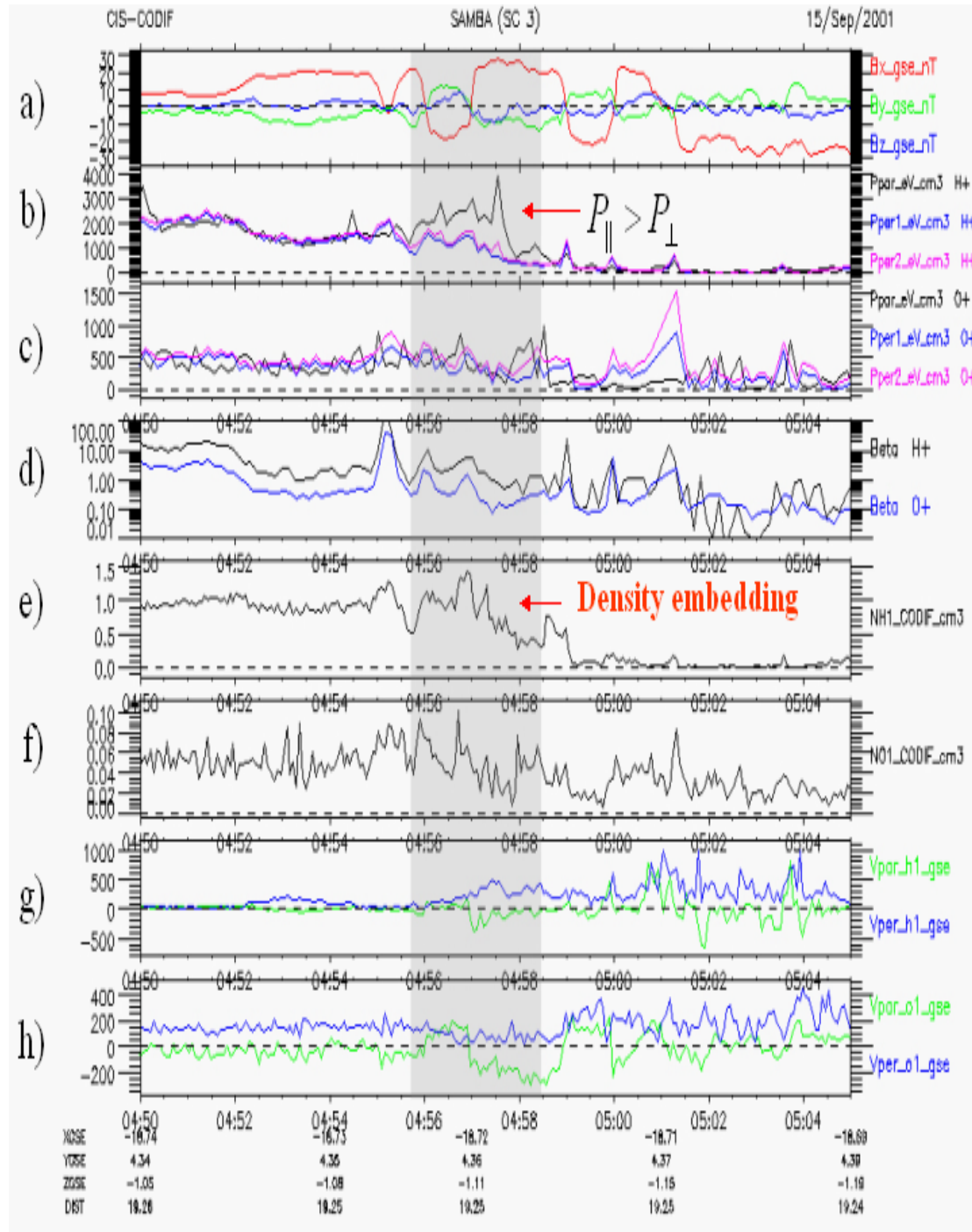


Fig.5.5 3-D momenta of proton and oxygen ions from C3. a) the components of magnetic field.. b) and c) are the pressure components of proton and oxygen ions respectively. d) beta value, a ratio of the plasma thermal pressure to the magnetic pressure. e) and f) are densities of proton and oxygen ions respectively. g) and h) are components of bulk velocity of proton and oxygen ions respectively. The shielding is an embedded proton TCS with an anisotropic but gyrotropic pressure  $p_{\parallel} > p_{\perp}$ .

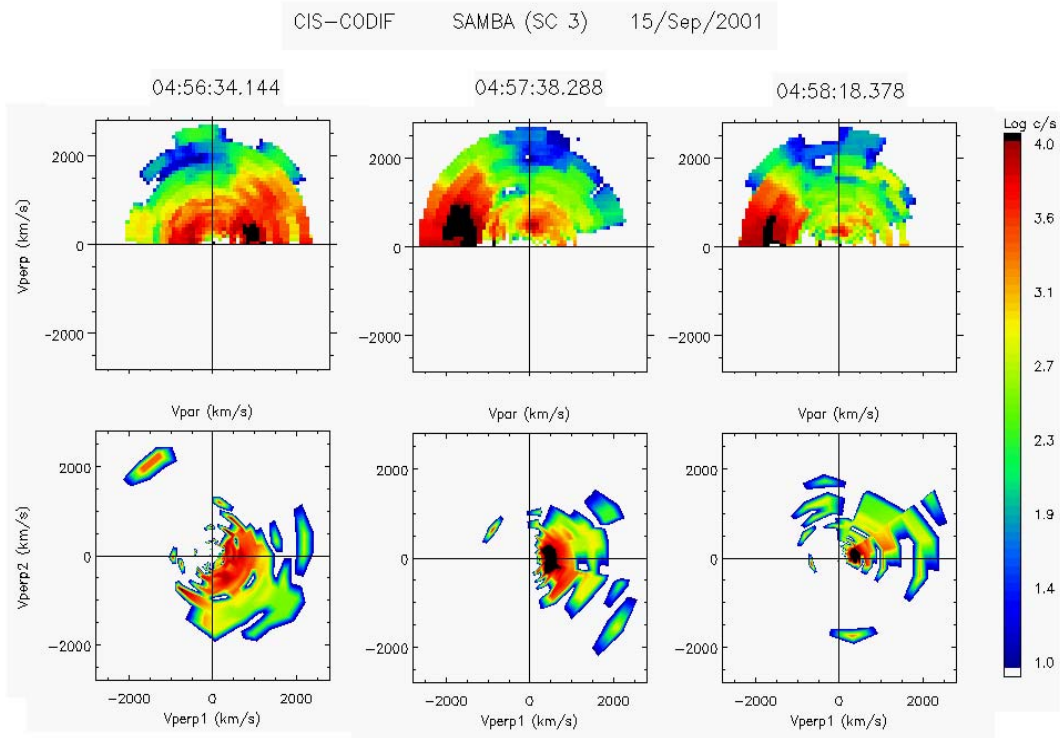


Fig.5.6 Distribution functions of protons in the  $V_{\parallel} - V_{\perp}$  coordinates from C3 in the embedded TCS. An apparent field-aligned beam can be found in these distributions. Where, the para-direction is defined in the direction along magnetic field, perp1 is in the direction of bulk velocity component perpendicular to the magnetic field, and perp2 is in the direction orthogonal both to para and perp1.

nonadiabatic thin layer, in which an equilibrium is achieved when the magnetic tension is balanced by the finite inertia of ions with meandering Speiser motion. Here it is also worthy to notice that the proton pressure is just only anisotropic and that no apparent nongyrotropy was detected. This seems to be contradictory since the ion motion should be nongyrotropic inside the TCS (Sitnov et al., 2006). We infer that ions are strongly nongyrotropic only in the center of the TCS but slightly nongyrotropic in the more outer part of the TCS. In the present situation, the satellite didn't stay close to the center of the TCS except for several rapid crossings of the central line, due to the flapping motion that will be shown in the following. It can be

also seen from the fact that in the panel d) in Fig.5.5, in this period  $\beta_H$  was moderate and no more than 1, while it was over 10 when the satellite was closer to the central line. This can explain why no apparent pressure nongyrotropy was observed. Apart from the current embedding, a plasma density embedding was also recorded. A proton density embedding is exhibited in the panel e) in Fig.5.5, while the oxygen ion density hasn't this manifestation. Although the concrete mechanism of density embedding isn't clear, there is an apparent correlation between the density embedding and the pressure anisotropy with  $p_{\parallel} > p_{\perp}$ .

### 2.3 TCS bifurcation

Nearly in the time interval UT 04:57:45-05:00:25, both the energy spectrogram and the pitch angle profile (they aren't shown here) reveal that a localized self-consistent current sheet equilibrium of oxygen ions was observed by C1 and C4, although in this very thin sheet the current contribution from oxygen ions is minor. We notice that due to the bulk excursion of the thicker Harris-like sheet (it is the up-down motion of the entire plasma sheet and is not the local flapping motion of the TCS observed by C3), the time difference of encounter of the above mentioned plasma depletion layer by C3 and C1 (at UT 04:59:05 and 05:00:25 respectively), which have a distance 1400km in the z direction between them, is about 80s, hence the shift velocity of the plasma sheet is about 17km/s. The duration of the crossing of the oxygen TCS is about 150s, thus the estimation of the thickness of the oxygen TCS is about 2500km. This is approximately one oxygen ion gyroradius and eleven times the proton gyroradius. Hence the localized oxygen ion current equilibrium is an extra-thin current sheet (Sitnov et al., 2006).

In the time interval UT 04:57:45-05:00:25, as shown by the shading in Fig.5.7, C1 measured an oxygen ion pressure anisotropy with  $p_{\parallel} < p_{\perp}$  and nongyrotropy  $p_{\perp 1} \neq p_{\perp 2}$  in the center of TCS, however in two edges the pressure is  $p_{\parallel} > p_{\perp}$  and nearly gyrotropic. The proton pressure in this time interval is isotropic in a surprising

level. As mentioned above, the ion motion is the non-adiabatic meandering Speiser motion in the TCS. Moreover, when the current sheet is thin enough to obey  $L \ll \rho_0 (B_0 / B_n)^2$  (where  $\rho_0$  is the particle gyroradius and  $B_0$  and  $B_n$  are the magnetic field at the outer of current sheet and its normal component in the center of sheet, to be satisfied definitely for the oxygen ion current sheet in the present situation), the motion of transient particles will be multi-crossings of the sheet, that is, a fast bounce motion across the thin sheet. In this case, the particle dynamics becomes approximately adiabatic or “quasi-adiabatic” along the normal direction of the sheet, and the so-called quasi-adiabatic sheet invariant can be introduced (Sonnerup, 1971).

As a consequence, the major motion of particles in the center of the TCS will be in the perpendicular direction. Fig.5.8 shows the oxygen ion distributions selected in the center of the thin sheet. It states the fact that the oxygen ion motion in the perpendicular direction is dominant. Combined with the necessary marginal firehose stability condition at the edge, it is exactly the particular observational feature in the present situation, that is, an oxygen ion pressure anisotropy with  $p_{\parallel} < p_{\perp}$  and nongyrotropy in the center of the TCS, but a gyrotropic pressure anisotropy with  $p_{\parallel} > p_{\perp}$  at edges. Moreover, non-adiabatic particles belonging to different classes with distinct dynamics in the phase space have different current carrying capabilities (Chen et al., 1986, Chen, 1992, Buchner et al., 1989, Burkhart et al., 1991, Zelenyi et al., 2002). The scattering of particle adiabatic invariant will result in the variation of the population of non-adiabatic particle and accordingly the current bifurcation. A detailed analysis on the particle kinetics will be presented elsewhere.

In the time interval UT 04:58:00-05:00:05, C4 recorded very similar features concerning the oxygen ion TCS as C1, as shown in Fig.5.9. The characteristics of oxygen ion distribution functions in the center of TCS are also like that observed by C1, as shown in Fig.5.10. We notice here that the distance between C1 and C4 in the Sun-Earth direction is the largest distance of the Cluster tetrahedron along the field line and that the distance in the normal direction between them is very small. The

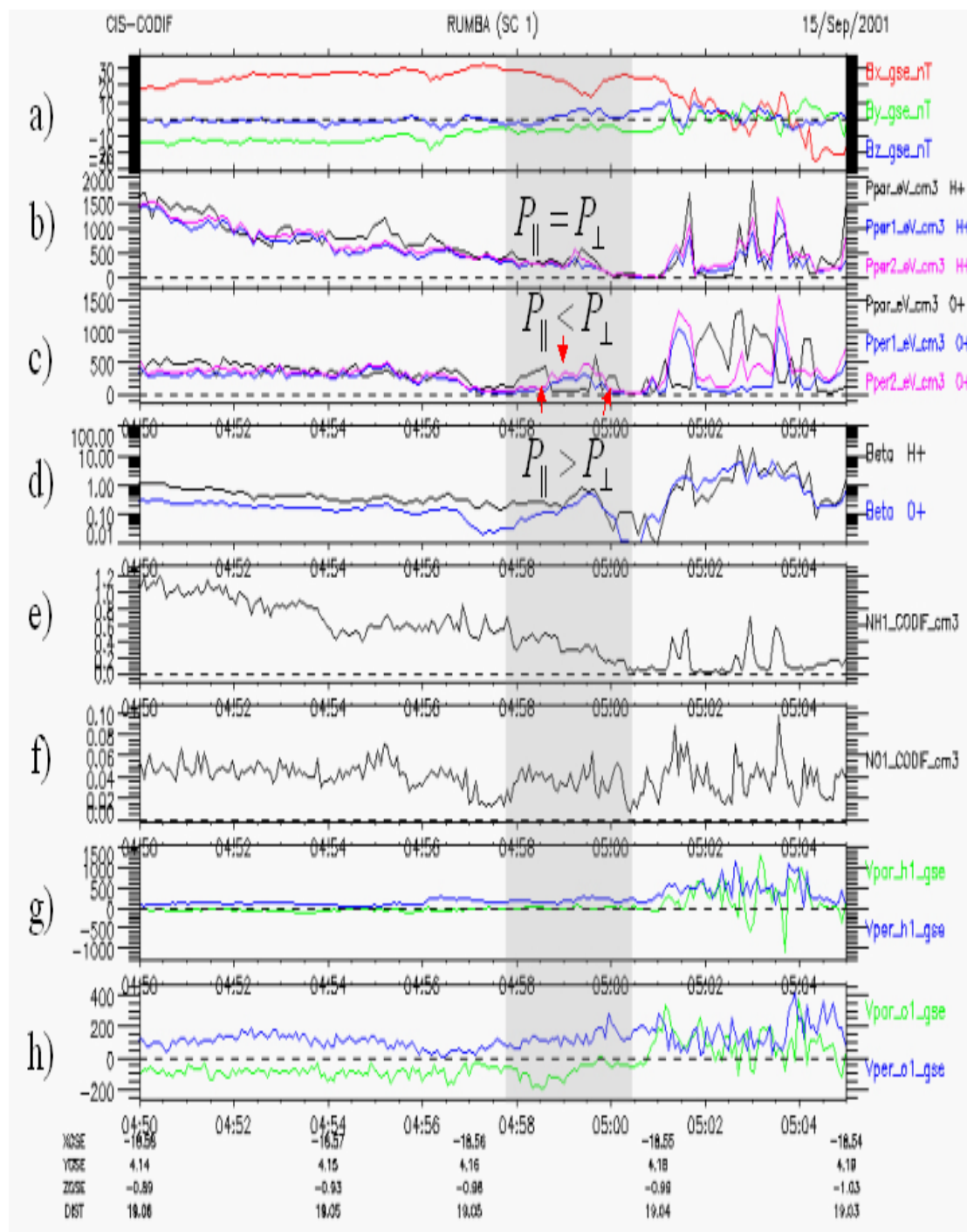


Fig.5.7 3-D momenta of proton and oxygen ions from C1. a) the components of magnetic field.. b) and c) are the pressure components of proton and oxygen ions respectively. d) beta value. e) and f) are densities of proton and oxygen ions respectively. g) and h) are components of bulk velocity of proton and oxygen ions respectively. The shielding is a bifurcated oxygen TCS with an anisotropic pressure  $p_{\parallel} < p_{\perp}$ .

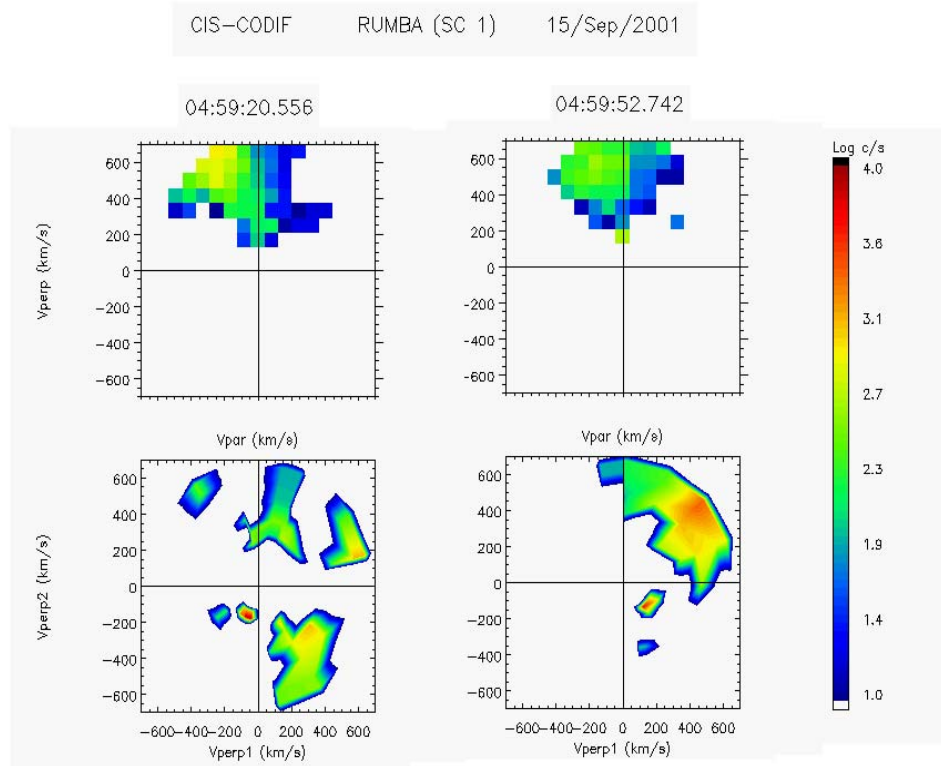


Fig.5.8 Distribution functions of oxygen ions in the  $V_{\parallel} - V_{\perp}$  coordinates from C1 in the bifurcated TCS.

similarity of measurements between C1 and C4 imply that the variance in the Sun-Earth direction is negligible, that is, the TCS can be described qualitatively by a one-dimension model. Also, absolute values of the plasma pressures recorded by C1 and C4 are nearly equal. This means that there is no pressure gradient in the field line direction. However, the pressure gradient is the necessary condition for TCS models with the isotropic pressure, in the case that the normal component of magnetic field is nonzero.

#### 2.4 Flapping motion

TCS is frequently found in association with rapid large-amplitude magnetic variations, namely flapping motion indicating rapid crossings through up-down oscillating

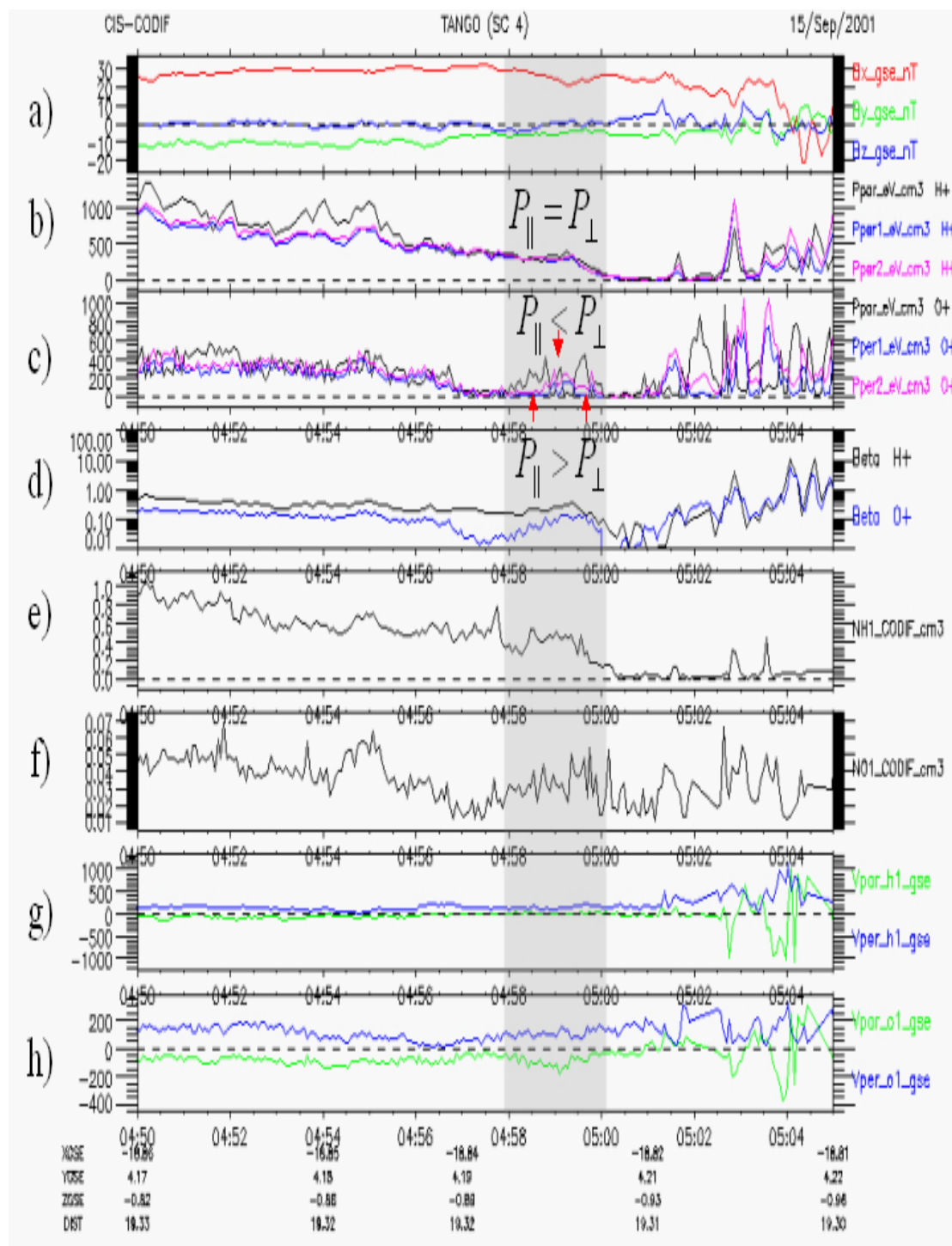


Fig.5.9 3-D momenta of proton and oxygen ions from C4. a) the components of magnetic field. b) and c) are the pressure components of proton and oxygen ions respectively. d) beta value. e) and f) are densities of proton and oxygen ions respectively. g) and h) are components of bulk velocity of proton and oxygen ions respectively. The shielding is a bifurcated oxygen TCS with an anisotropic pressure  $p_{\parallel} < p_{\perp}$ .

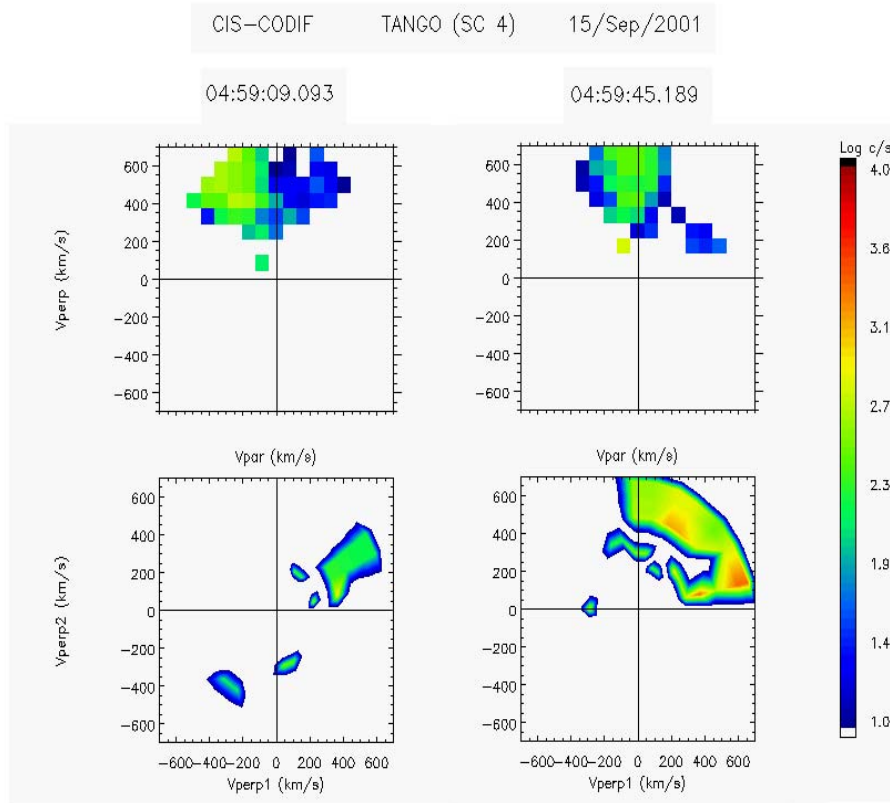


Fig.5.10 Distribution functions of oxygen ions in the  $V_{\parallel} - V_{\perp}$  coordinates from C4 in the bifurcated TCS.

current sheet. During the period of UT 04:55-05:02, four rapid large-amplitude  $B_x$  variations were observed by C3, as labeled by the shadings in Fig.5.11. Their peaks were at UT 04:55:10, 04:56:30, 04:59:35 and 05:01:30 respectively. The  $B_x$  variations were also apparently recorded, but weaker, in phase by C2; while C1 measured in phase the perceptible  $B_x$  variations only at the third and fourth oscillations, and C4 nearly recorded nothing except a variation with a negligible amplitude at the third oscillation. These magnetic variations are the manifestation of kink-like wave propagating in the dawn-dusk direction (Sergeev et al., 2003, Runov et al., 2003a, 2005). Utilizing the time difference of the peak of magnetic variations between C3 and C2, we can estimate its phase speed to be 120 km/s, 50 km/s, 30 km/s

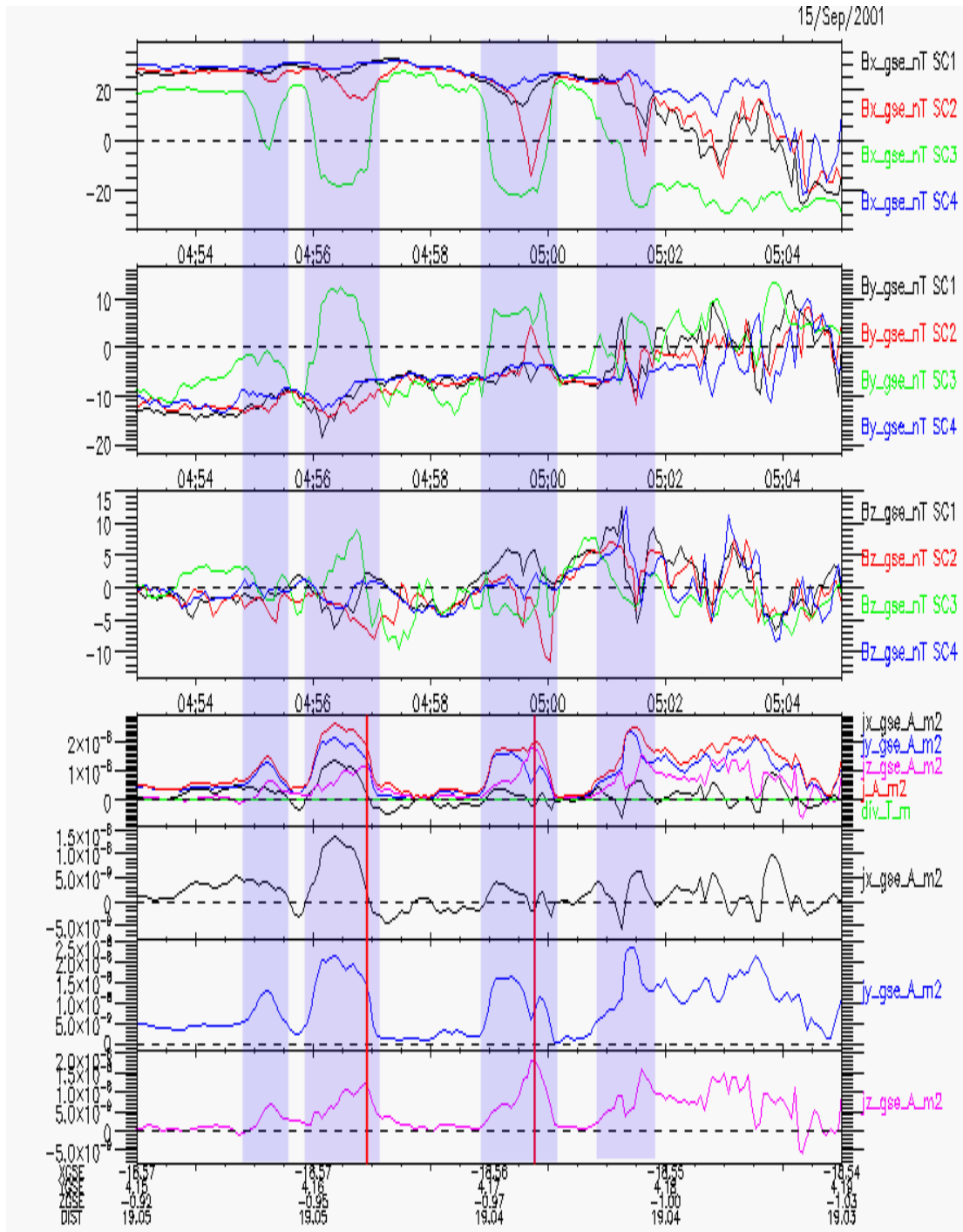


Fig.5.11 Components of magnetic field and the current density for the four Cluster satellites. Four large-amplitude magnetic variations due to flapping motion are labeled by the shadows. As labeled by solid vertical lines, peaks of  $j_z$  are not corresponding to peaks of  $j_y$  and  $j_x$ , but corresponding to edges of them. It is manifestation of localized large-amplitude kink motions of the current sheet.

and 40 km/s corresponding to four oscillations respectively. The periods of the four oscillations are 70 s, 190 s, 125 s and 110 s respectively. The wavelength is approximately  $0.8\sim 1.5 R_E$ . The propagating speed estimated here is in agreement with the previous statistical investigations, that is, in the range of several tens km/s up to 200 km/s (Sergeev et al., 2004, Zhang et al., 2005). Moreover, the present event reveals explicitly the solitary wave feature of the flapping motion. For the first and fourth oscillations, the flapping amplitude is smaller than that of the second and third oscillations. Recalling that the period and phase speed have also a similar feature, it is apparent that the behavior of flapping motion resembles to a solitary wave modulated both on its amplitude and frequency.

Due to the localized large-amplitude kink motion, the current would have a circular flow in the  $y$ - $z$  plane. This point can also be seen in the simulation work (Sitnov et al., 2006). Via the current density and its components shown from the panel d) to g) in Fig.5.11, circular flows corresponding to the second and third oscillations can be discovered. As labeled by a solid vertical line, at each circular flow, the peak of  $j_z$  is not corresponding to the peak of  $j_y$  and  $j_x$ , but corresponding to the edge of them. It is just about the manifestation of the current circular flow. At that time, the current sheet is tilted. As shown on the panel b) and c), for the second and third oscillations, C3 and C2 recorded large-amplitude  $B_y$  or  $B_z$  variations, reflecting the localized current sheet inclination.

### 3. Discussion

It is worthy to point out that although recently many observational investigations on TCS in the magnetotail were reported, but few of them involved the particle kinetics. The observations presented here reveal the crucial role played by the ion kinetics in the dynamics of TCS. Particles in the region with a strong magnetic field gradient have totally different properties of motion in contrast to magnetic momentum

adiabatic kinetics. The interaction of these nonadiabatic particles with the current sheet achieves eventually a self-consistent TCS equilibrium. These equilibria manifest distinct behaviors from Harris equilibrium, and in association with their intrinsic particle anisotropy and nongyrotropy. They are qualitatively in a good agreement with the conclusions given by these theoretical models considered into the so-called quasi-adiabatic sheet invariant (Sitnov et al., 2000, 2003, 2006).

The origin of TCS is unclear by now, although often referred it to the fast flow caused by the magnetic reconnection or substorm (Runov et al., 2003b, Asano et al., 2005). Here, the proton TCS was most likely due to field-aligned proton beams. But the source of these beams is also unclear. During the present event, a substorm onset around UT 04:55 had been claimed (Voronkov et al., 2006). However, any obvious explosive plasma flow was absent in the beginning of the occurrence of the proton TCS. In the panels g) and h) in Fig.5.5, we notice that till UT 04:57:00, no perceptible bulk proton flow was observed. A modest parallel flow was recorded once during the central line crossing at UT 04:57. From UT 04:57:30 a modest perpendicular flow was observed. Likewise, in this period a modest oxygen ion flow was observed to be no more than 200km/s. Similar measurements can also found in Fig.5.7 and Fig.5.9. TCS observations without any fast plasma flow have also been reported in previous investigations (Sergeev et al., 2003, Asano et al., 2005).

The excitation mechanism of TCS flapping motion is an argumentative issue, and seems not to match anyone that had been discussed so far in previous investigations. A heuristic approach on its ignition mechanism may be gained in the present event. In the panel b) in Fig.5.5, from UT 04:54 to 05:02, several small singular peaks of proton pressure was recorded, each corresponds to either the crossing of the central line or the stay at the outermost of TCS. Those peaks encountered across the central line are coming from density increases, and the corresponding small proton density peaks can be seen in the panel e). It indicates that density gradients exist in the center of TCS, in contrast to the case in thick sheets, in which the density gradient occurs only at the edge. Therefore, in the present event, the low hybrid drift instability is possible to

develop from the observed density gradients. In the current sheet, the low hybrid drift instability was intensely investigated and also had been considered as the source of the current sheet flapping motion (Daughton, 1999, 2002,2003, Lapenta et al., 2002). Meanwhile, at UT 04:54:24, before the ignition of TCS flapping, the first singular peak of proton pressure without any perceptible magnetic perturbation was recorded. It implies that the disturbance is a kinetic pressure pulse nearby the TCS at that time and will spread with the sound speed. When the fluctuation couples to the potentially excited low hybrid drift instability mentioned above, it might eventually evolve into a solitary wave modulated both on its amplitude and frequency via nonlinear interactions. Flapping motion is frequently not only associated with the TCS but also accompanied with the magnetic reconnection, both of them occurring in small scale. It also reflects, on the other hand, the concerned role played by the low hybrid drift instability, which is easier to grow up in TCSs than in thick sheets. Hence observations presented here also give an insight into the generation mechanism of the TCS flapping motion.

#### 4. Conclusion

During the Cluster spacecraft crossing of the magnetotail on September 15, 2001, both TCS embedding and bifurcation were recorded in one single event, due to the Cluster unique capabilities of spatial resolution on small scale. The intrinsic properties of nonadiabatic particle dynamics in the TCS are emphasized. It is indicated that the ion anisotropy and nongyrotropy are responsible for those new equilibrium features deviated from the conventional Harris model. An embedded proton TCS manifests a pressure anisotropy with  $p_{\parallel} > p_{\perp}$ , simultaneously associated with a density embedding, while a bifurcated oxygen ion TCS exhibits a pressure anisotropy mainly with  $p_{\parallel} < p_{\perp}$  and nongyrotropy. Except at edges  $p_{\parallel} > p_{\perp}$  is the necessary marginal firehose stability condition. The local flapping motion of the TCS was observed, and

some particular feature such as the solitary wave-like behavior and the kink motion in the  $y$ - $z$  plane was revealed. A heuristic approach on its ignition mechanism is presented to support that the TCS flapping motion is coming from a localized kinetic pressure pulse. The present investigation intimates the complexity of manifestations of magnetotail current sheet and displays the important role played by the ion kinetics in the self-consistent TCS equilibrium. The results of this chapter have been published in Cai et al., 2008.



## Conclusions et perspectives

En raison de l'avantage des mesures multipoints avec une grande résolution, les études observationnelles de quelques processus importants de plasma et de structures à petites échelles dans l'environnement spatial de la Terre sont faisables. Dans cette thèse, ces structures importantes, en association avec la cinétique des particules dans la magnétosphère terrestre, spécialement la cinétique des ions en régime basse énergie, dans quelques couches frontières cruciales avec diverses conditions de plasma ont été étudiées au moyen des données des missions Cluster et Double Star.

1. Les effets des particules individuelles jouent un rôle essentiel dans la formation de ces structures de plasma à petites échelles.

Les structures très petites des fluctuations de flux associées avec le phénomène de transport du plasma de la magnétogaine à travers la magnétopause sont la manifestation de l'instabilité de dérive en-dessous de la gyrofréquence ionique, dont la physique de base est l'accumulation de charges et la perturbation en résultant du potentiel électrostatique. Le mouvement éventuel du "cross-field vortex" dans l'état non linéaire de ce processus et l'échange de masse associé sont aussi attribués à l'effet des particules individuelles.

Dans la région d'écoulement vers l'extérieur de la reconnexion dans la queue magnétique, une cavité de densité se forme et manifeste une morphologie particulière comme un pré-choc due aux processus cinétiques complexes, de façon similaire au pré-choc terrestre. Dans la cavité, il existe des faisceaux de protons réfléchis alignés au champ magnétique et, simultanément, des distributions des distributions de protons de type cône de perte. En outre, deux manifestations d'électrons réfléchis avec un mode de "bump-on-tail" large et étroit sont observées juste en amont du bord d'attaque du pré-choc ionique et près du front de choc respectivement. Ces deux manifestations différentes des électrons réfléchis montrent les différences dans la physique microscopique du processus de réflexion.

La cinétique des particules domine la dynamique de ces minces couches de courant dans la queue magnétosphérique, dont l'épaisseur est de l'ordre du rayon de giration ou de la longueur inertielle. Ceci indique que l'anisotropie et la nongirotropie des ions sont responsables des caractéristiques de ce nouvel équilibre qui dévie du modèle conventionnel d'Harris. Les particules dans une région avec un fort gradient de champ magnétique ont des propriétés de mouvement totalement différentes de la cinétique adiabatique du moment magnétique. L'interaction de ces particules non-adiabatiques avec la couche de courant atteint éventuellement un équilibre self-consistant de la couche mince de courant.

2. La cinétique des particules dans les structures à petites échelles montre quelques caractéristiques des processus de microphysique non linéaire dans un plasma sans collision.

Dans la dynamique des ondes de dérive de basses fréquences, l'instabilité provient de la non adiabaticité de la dynamique parallèle des électrons due à leur plus grande viscosité effective, qui est responsable pour l'accumulation de charges. Ceci montre un processus de dissipation hyper visqueux.

Dans la cavité de type prè-choc dans la reconnexion de la queue magnétique, l'existence de particules réfléchies indique que, en plus de la résistivité anormale, qui est fournie par différentes instabilités déclenchées par le courant électrique généré à la mince rampe du choc, il y a une source additionnelle de dissipation par viscosité non locale pour maintenir la frontière d'attaque accentuée du jet des ions. C'est aussi un mécanisme de dissipation hyper visqueux.

Pour une couche de courant mince dans la queue magnétique, l'équilibre est atteint par balance entre la tension magnétique et la tension due à la pression anisotrope, au contraire de l'équilibre Harris, dans lequel l'équilibre est maintenu par la balance entre la tension de la ligne de champ et le gradient de pression du plasma. Ceci montre le rôle crucial joué par l'inertie finie des ions

dans la configuration magnétique de la couche mince avec un fort gradient de champ magnétique.

3. La cinétique des particules dans les structures à petites échelles est hautement dynamique et présente la caractéristique de processus de couplage multi-échelles.

A la magnétopause, un mouvement d'ensemble de la magnétogaine à grande échelle peut développer une région localisée sans cisaillement magnétique pour faciliter une instabilité de dérive et donc est relié aux structures fines ultérieures du processus de transport.

Dans la région d'empilement des lignes de champ dans la région d'écoulement de la reconnexion de la queue magnétique, la présence d'une frontière accentuée du jet d'ions rapides et ses accessoires avec une structure de type pré-choc sont très non-stationnaire et localisés dans l'espace et dans le temps. En outre, cette structure cohérente auto-organisée à moyennes échelles, plus petite que les dimensions de la couche entière de reconnexion mais plus grande que les échelles cinétiques des particules, peut agir comme un accélérateur des ions pour fournir plus d'accélération dans leurs processus d'accélération multi-pas dans la reconnexion.

La dynamique des couches de courant minces dans la queue magnétique présente non seulement des processus d'échelle cinétiques, par lesquels un équilibre auto-consistent peut éventuellement être atteint, mais aussi est en association avec une instabilité de d'ensemble à grande échelle du mouvement de battement de grande amplitude.

Des investigations précédentes nombreuses et nos études présentées dans cette thèse améliore notre compréhension de ces phénomènes à multiéchelles dans l'environnement spatial de la terre. Cependant en raison de leur complexité, les physiciens spatiaux ont encore besoin d'investigation plus profondes de physique fondamentale. La reconnexion magnétique et les couches de courant minces sont deux de ces questions difficiles.

Le commencement de la reconnexion est supposée survenir sur des échelles spatiales et temporelles des mouvements de giration des électrons et des ions, où les processus à microéchelles contrôle le changement de topologie du champ magnétique. D'un autre côté, les processus à grandes échelles contrôlent l'emplacement et la formation des couches minces de courant, et affectent aussi directement le déclenchement et l'évolution de la reconnexion. Il est donc essentiel d'étudier à la fois les processus à grandes échelles et les processus cinétiques du plasma pour comprendre la montée, l'évolution et les conséquences de la reconnexion magnétique.

Un des principaux buts de la recherche sur la reconnexion magnétique est de comprendre le mécanisme de dissipation dans la région de diffusion. Au voisinage d'un site de reconnexion, les ions et les électrons ne sont plus magnétisés et ne sont plus gelés au flux magnétique dans leurs régions de diffusion respectives, qui sont de l'ordre, respectivement, des rayons de giration des ions et des électrons. Dans la région de diffusion des ions mais en dehors de la région de diffusion des électrons, les électrons magnétisés continuent à s'écouler vers l'intérieur vers la région de diffusion des électrons mais les ions non magnétisés sont découplés du mouvement des lignes de champ magnétique. Le mouvement relatif des ions et des électrons génère un courant de Hall en association avec un champ électrique de Hall. Comme conséquence de ce système de courant une signature caractéristique de champ magnétique quadripolaire de Hall est générée. Cependant, la nature de la région de diffusion des électrons et les processus dans cette région qui démagnétisent les électrons, permettant le déclenchement de la reconnexion, ne sont pas bien compris. Afin de trouver quels mécanismes sont responsables de la diffusion des électrons, il est nécessaire de considérer les phénomènes à plus petites échelles, incluant l'anisotropie de pression des électrons associés avec des distributions de vitesses non-gyrotropes. En outre, nous avons aussi besoin de prendre en compte les interactions ondes-particules, qui peuvent diffuser et démagnétiser les électrons dans et autour de leur région de diffusion.

La plupart de l'énergie dégagée pendant le processus de reconnexion est transmise

aux ions et aux électrons. Le champ électrique de reconnexion est supposé avoir une composante le long de la direction du champ magnétique local dans la région de diffusion, qui accélérera rapidement les particules chargées. D'autres processus d'accélération sont aussi supposés sur les lignes de champ magnétique en contraction, dans les jets vers l'extérieur de la reconnexion, comme ceci a été montré dans cette thèse. Cependant, la compréhension de ces processus cinétiques est loin d'être complète. Des mesures sur des échelles ioniques et fluides sont nécessaires pour déterminer l'évolution de l'énergie des particules avec l'augmentation de la distance depuis l'endroit de la reconnexion et pour mesurer le champ magnétique et d'autres paramètres pour tester si le degré d'augmentation de l'énergie est consistant avec ce qui est supposé des modèles théoriques.

Les jets d'ions rapides dans la région d'écoulement, conséquence de la reconnexion magnétique, montrent des structures internes complexes dues à leurs interactions avec les plasmas ambiants. Une partie de celles-ci ont été étudiées dans cette thèse. Il est nécessaire d'apprendre plus sur les différentes couches frontières singulières dans ces jets d'ions rapides et leur évolution.

La dynamique de la couche mince de courant est un autre sujet intéressant, impliquant un nombre de processus physiques sur une large gamme d'échelles spatiales et temporelles. L'origine des couches minces de courant n'est pas claire actuellement, bien que dans le cas de la queue magnétique il est souvent attribué à l'écoulement rapide causé par la reconnexion magnétique ou le sous-orage. Cependant, les événements de couche mince de courant en association avec des écoulements rapides et sans écoulement rapide de plasma ont été présentés dans des recherches précédentes. Ainsi, l'initiation de couches minces de courant est cruciale pour comprendre les processus de conversion d'énergie dans la queue magnétique.

Le mécanisme d'excitation du mouvement d'oscillation des couches minces de courant est une question à débattre. Les caractéristiques observationnelles de la propagation vers les flancs et la faible vitesse de propagation sont inattendues et semblent ne satisfaire aucun modèle théorique discuté jusqu'ici. D'autres études,

expérimentales et théoriques, sont nécessaires pour clarifier ce problème.

La structure interne des couches de courant et les détails des populations de particules sont importantes pour comprendre leur dynamique. Les variations de la composition des ions dans la couche mince de courant pendant leur évolution ne sont pas encore bien comprises. Dans une couche mince de courant, les particules non adiabatiques appartenant à différentes classes avec une dynamique distincte dans l'espace des phases ont différentes possibilités pour transporter le courant. La diffusion des invariants adiabatiques des particules viendra de la variation de la population des particules non adiabatiques et ainsi influencera l'équilibre d'une couche mince de courant. Cependant, la compréhension complète de ces processus cinétiques est loin d'être atteinte. De plus, parfois des couches de courant très minces peuvent se développer, dont l'épaisseur peut être aussi fine que le rayon de giration des ions, et peut-être même de l'échelle cinétique des électrons. Dans ces couches très minces, la question reste ouverte pour savoir si les ions ou les électrons sont les porteurs principaux du courant à travers le champ. Tous ces processus complexes de microphysique nécessitent une totale compréhension.

En résumé, les expériences sur ces structures de plasma dans des couches frontières importantes de la magnétosphère sont de la plus haute importance afin d'améliorer notre connaissance de ces phénomènes spatiaux essentiels sur une large gamme d'échelles multiples espace-temps et leurs couplages à multi-échelles.

## Conclusions and perspective

Due to the advantage of multiple-point measurements with high resolution, observational studies of some important plasma processes and structures in small scales in the geospace are feasible. In the present thesis, those prominent structures in association with their particle kinetics in the terrestrial magnetosphere, especially ion kinetics in low energy regime in some crucial boundary layers with highly diverse plasma conditions, are investigated by means of the data from the missions of Cluster and Double Star.

1. Individual particle effects play a dominating role in formation of those small-scale plasma structures.

The fine structures of flux fluctuations associated with the transport phenomenon of magnetosheath plasma across the magnetopause, are found to be the manifestation of the drift instability below the ion gyrofrequency, whose underlying physics is charge accumulation and the resulting electrostatic potential perturbation. The eventual cross-field vortex motion in the nonlinear stage of this process and the associated mass exchange are also attributed to individual particle effect.

In the outflow region of reconnection in the magnetotail, a density cavity forms and manifests a particular foreshock-like morphology due to the complex kinetic processes, which is similar to that of the terrestrial foreshock. In the cavity, there exists reflected field-aligned proton beams and simultaneously magnetic-mirror loss-cone proton distributions. In addition, two manifestations of reflected electrons with a broad and narrow bump-on-tail pattern are observed just upstream of the leading edge of the ion foreshock and close to the shock front respectively. These two different manifestations of reflected electrons reveal the differences in their microscopic physics of the reflecting process.

Particle kinetics rules the dynamics of those thin current sheets in the magnetotail, whose thickness is on the order of the ion gyroradius or inertial

length. It is indicated that the ion anisotropy and nongyrotropy are responsible for those new equilibrium features that deviate from the conventional Harris model. Particles in a region with a strong magnetic field gradient have totally different properties of motion that are in contrast with the magnetic momentum adiabatic kinetics. The interaction of these nonadiabatic particles with the current sheet achieves eventually a self-consistent equilibrium of thin current sheet.

2. Particle kinetics in small-scale structures reveals some universal characteristics of nonlinear microphysical processes in collisionless plasma.

In the dynamics of the low-frequency drift wave, the instability results from the non-adiabaticity of the parallel dynamics of electrons due to their larger effective viscosity, which is responsible for the charge accumulation. It reveals a hyper-viscous dissipation process.

In the foreshock-like cavity in the magnetotail reconnection, the existence of reflected particles indicates that besides the anomalous resistivity, which is provided by various instabilities driven by the electric current generated at the thin shock ramp, there is an additional source of dissipation by non-local viscosity to maintain the steepened leading boundary of ions jet. It is also the hyper-viscous dissipation mechanism.

For a thin current sheet in the magnetotail, the equilibrium is achieved by the balance between the magnetic tension and the tension due to the anisotropic pressure, in contrast to Harris equilibrium, in which the equilibrium is maintained by a balance between the field line tension and the plasma pressure gradient. It reveals the crucial role played by the finite ion inertia in the magnetic configuration of thin sheet with a strong magnetic field gradient.

3. Particle kinetics in small-scale structures has diverse behaviors in various scales and exhibits the feature of cross-scale coupling processes.

At the magnetopause, a large-scale bulk motion of the magnetosheath can develop a localized region without magnetic shear to facilitate a low-frequency drift instability and therefore is linked to the subsequent fine structures of transport

process.

In the field line piled up region in the outflow region of magnetotail reconnection, the occurrence of a steepened boundary of the fast ion jet and its accessories with a foreshock-like structure are highly non-stationary and localized both in space and time. Further, this self-organized coherent structure in meso-scale, smaller than the size of the entire reconnection layer but larger than the particle kinetic scales, can act as an accelerator of ions to provide further acceleration in their multi-step acceleration processes in the reconnection.

The dynamics of thin current sheets in the magnetotail possesses not only kinetic scale processes, by which a self-consistent equilibrium is eventually achieved, but also is in association with the large-scale bulk instability of large-amplitude flapping motion.

Abundant previous investigations and our studies presented in this thesis improve our understanding of those multiscale phenomena in Geospace. However on account of their complexity, space physicists still need to have a deeper investigation on their fundamental physics. Magnetic reconnection and thin current sheets are two of these most challenging issues.

The onset of reconnection is expected to occur on the spatial and temporal scales of the relevant electron and ion gyromotions, where microscale processes control the change of topology of the magnetic field. On the other hand, large-scale processes control the location and formation of thin current sheets, and thus directly affect the triggering and evolution of reconnection. It is therefore essential to study both the large-scale and kinetic scale processes of the plasma to understand the onset, the evolution, and the consequences of magnetic reconnection.

One of the main goals of magnetic reconnection research is to understand the dissipation mechanism in the diffusion region. In the vicinity of a reconnection site, the ions and electrons are no longer magnetized and are not “frozen-in” to the magnetic flux in their respective diffusion regions, which are on the order of the ion and electron gyroradii respectively. In the ion diffusion region but out of the electron

diffusion region, magnetized electrons continue to flow inwards towards the electron diffusion region but unmagnetized ions are decoupled from the motion of magnetic field lines. The relative motion of ions and electrons generates a Hall current in association with a Hall electric field. As a consequence of this current system a characteristic quadrupolar Hall magnetic field signature is generated. However, the nature of the electron diffusion region and the processes within it that demagnetize the electrons, allowing reconnection to occur, are not well understood. In order to find which mechanisms are responsible for diffusing electrons, it is necessary to consider phenomena in further smaller scales, including electron pressure anisotropy associated with non-gyrotropic velocity distributions. In addition, we also need to take into account wave-particle interactions, which may scatter and demagnetize electrons in and around their diffusion region.

Most of the energy released during the reconnection process goes into the energization of ions and electrons. The reconnection electric field is expected to have a component along the local magnetic field direction in the diffusion region, which will readily accelerate charged particles. Some further acceleration processes are also expected on the contracting magnetic field lines in the reconnection outflow jets, as have been revealed in the present thesis. However, understanding of these kinetic processes is far from completion. Measurements on ion and fluid scales are needed to capture the evolution of particle energy with increasing distance away from the reconnection site, and to measure the magnetic field and other parameters to test whether the degree of energization is consistent with that expected from theoretical models.

The fast ion jets in the outflow region, as the consequence of magnetic reconnection, exhibit complex internal structures due to their interactions with the ambient plasmas. Parts of them have been investigated in the present thesis. It is necessary to learn further about various singular boundary layers in these fast ion jets and their evolution.

Dynamics of thin current sheet is another appealing subject, involving a number of

physical processes over a wide range of spatial and temporal scales. The origin of thin current sheets is unclear by now, although in the case of magnetotail it is often referred to the fast flow caused by the magnetic reconnection or substorm. However, events of thin current sheet both in association with fast flows and without any fast plasma flow have been reported in previous investigations. Thus, the initiation of thin current sheets is crucial to understand the processes of energy conversion in the magnetotail.

The excitation mechanism of flapping motion of thin current sheets is an issue of debate. The observational feature of flankward propagation and low propagating speed are unexpected and seem not to match any theoretical model that had been discussed so far. Further studies, both observational and theoretical, are needed to clarify this problem.

The internal structure of current sheets and the details of particle populations are important to the understanding of their dynamics. The variations of ion composition in thin current sheets during their evolution are not well understood yet. In a thin current sheet, non-adiabatic particles belonging to different classes with distinct dynamics in the phase space have different current carrying capabilities. The scattering of particle adiabatic invariants will result in the variation of the population of non-adiabatic particles and will thus influence the equilibrium of a thin current sheet. However, a complete understanding of these kinetic processes is far from being achieved. Moreover, sometime extra thin current sheets may develop, whose thickness can be as thin as the ion gyro radius, and possibly even of the electron kinetic scale. In these extra thin sheets, whether ions or electrons are the main carriers of the cross-field current remains an open question. All these complex microphysical processes need a full comprehension.

In summary, investigations on those plasma structures in important boundary layers of the magnetosphere are of paramount importance in order to improve our knowledge of those prominent space phenomena over a wide range of multiple spatio-temporal scales and their cross-scale couplings.



## References

- Abe, S. and M. Hoshino,: Nonlinear evolution of plasmoid structure, *Earth Planets Space*, 53, 663–671, 2001
- Akasofu, S.-I., Energy Coupling Between the SolarWind and the Magnetosphere, *Space Sci. Rev.* **28**, 121, 1981.
- Anderson, K. A., J. H. Binsack, and D. H. Fairfield, Evidence for hydromagnetic waves of 3- to 15-minute period on the magnetopause and their relation to bow shock spikes, *J. Geophys. Res.*, 73, 2371, 1968.
- Asano, Y., Nakamura, R., Baumjohann, W., Runov, A., Voros, Z., Volwerk, M., Zhang, T. L., Balogh, A., Klecker, B., and Rème, H.: How typical are atypical current sheets ?, *Geophys. Res. Lett.*, 32, L03108, doi:10.1029/2004GL021834, 2005.
- Bale, S. D., M. A. Balikhin, T. S. Horbury, V. V. Krasnoselskikh, H. Kucharek, E. Möbius, S. N. Walker, A. Balogh, D. Burgess, B. Lembege, E. A. Lucek, M. Scholer, S. J. Schwartz, and M. F. Thomsen,: Quasi-perpendicular shock structure and processes. *Space Sci. Rev.*, 118, 161-203, 2005
- Balogh, A., C. M. Carr, M. H. Acuña, M. W. Dunlop, T. J. Beek, P. Brown, K.-H. Fornacon, E. Georgescu, K.-H. Glassmeier, J. Harris, G. Musmann, T. Oddy, and K. Schwingenschuh,: The Cluster Magnetic Field Investigation: Overview of in-flight performance and initial results, *Ann. Geophys.*, 19, 1207–1217, 2001.
- Balogh, A., S. J. Schwartz, S. D. Bale, M. A. Balikhin, D. Burgess, T. S. Horbury, V. V. Krasnoselskikh, H. Kucharek, B. Lembege, E. A. Lucek, E. Mobius, M. Scholer, M. F. Thomsen, and S. N. Walker,: Cluster at the Earth's Bow Shock: Introduction. *Space Sci. Rev.* 118: 155–160, 2005.
- Bame, J. R., G. Moreno, A. J. Lazarus, and J. D. Sullivan,: Deceleration of the solar wind upstream from the Earth's bow shock and the origin of diffuse upstream ions, *J. Geophys. Res.*, 85, 2981 – 2990, doi:10.1029/JA085iA06p02981, 1980.
- Berchem, J. and C. T. Russell, The thickness of the magnetopause current layer, *J. Geophys. Res.*, 87, 2108, 1982.

Birn, J., Schindler, K., and Hesse, M.: Thin electron current sheets and their relation to auroral potentials, *J. Geophys. Res.*, 109, A02217, doi:10.1029/2003JA010303, 2004a.

Birn, J., Thomsen, M. F., and Hesse, M.: Acceleration of oxygen ions in the dynamic magnetotail, *Ann. Geophys.*, 22, 1305–1315, 2004b.

Buchner, J. and Zelenyi, L. M.: Regular and chaotic charged particle motion in magnetotail-like field reversals: 1. Basic theory, *J. Geophys. Res.*, 94, 11 821–11 842, 1989.

Burkhart, G. R. and Chen, J.: Differential Memory in the Earth's magnetotail, *J. Geophys. Res.*, 96, 14 033–14 049, 1991.

Cai, C.L., I. Dandouras, H. Rème, J.B. Cao, G.C. Zhou, G.K. Parks,: Cluster observations on the thin current sheet in the magnetotail, *Ann. Geophys.*, 26, 929-940, 2008.

Cai, C.L., I. Dandouras, H. Rème, J.B. Cao, G.C. Zhou, C. Shen, G.K. Parks, D. Fontaine, Magnetosheath excursion and the relevant transport process at the magnetopause, *Ann. Geophys.*, 27, 2997–3005, 2009a.

Cai, C.L., I. Dandouras, H. Rème, J.B. Cao, G.C. Zhou, G.K. Parks, D. Fontaine, Foreshock-like Density Cavity in the Outflow Region of Magnetotail Reconnection, *Ann. Geophys.*, 27, 3043–3053, 2009b.

Camporeale, E. and Lapenta, G.: Model of bifurcated current sheets in the Earth's magnetotail: Equilibrium and stability, *J. Geophys. Res.*, 110, A07206, doi:10.1029/2004JA010779, 2005.

Cao, J. B., Z. X. Liu, C. X. Yan, C. L. Cai, L. Y. Li, G. W. Zhu, S. J. Wang, H. Zhao, J. B. Liang, Q. Y. Ren, Y. Y. Zai, H. Rème, I. Dandouras, C. Aoustin, P. Escoubet, A. Fazakerley, S. McKenna-Lawlor, and M. Dunlop, First results of Chinese particle instruments in the Double Star Program, *Annales Geophysicae*, 23, 2775–2784, 2005.

Cao, J. B., H. S. Fu, T. L. Zhang, H. Rème, I. Dandouras, and E. Lucek,: Direct evidence of solar wind deceleration in the foreshock of the Earth, *J. Geophys. Res.*, 114, A02207, doi:10.1029/2008JA013524, 2009.

Cattell, C., J. Dombek, J. Wygant, J. F. Drake, M. Swisdak, M. L. Goldstein, W.

Keith, A. Fazakerley, M. Andre, E. Lucek, and A. Balogh,: Cluster observations of electron holes in association with magnetotail reconnection and comparison to simulations, *J. Geophys. Res.*, 110, A01211, doi:10.1029/2004JA010519, 2005.

Chapman, S., and V. Ferraro, A new theory of magnetic storms, I, the initial phase, *Terrest. Magnetism and Atmospheric Elec.*, 36, 171–186, 1931.

Chen, F. F.,: Introduction to Plasma Physics and Controlled Fusion, Vol 1: Plasma Physics, Second Edition, Plenum Press, 1984.

Chen, J. and Palmadesso, P. J.: Chaos and Nonlinear Dynamics of Single-Particle Orbits in a Magnetotail-Like Magnetic Field, *J. Geophys. Res.*, 91, 1499–1508, 1986.

Chen, J.: Nonlinear dynamics of charged particles in the magnetotail, *J. Geophys. Res.*, 97, 15 011–15 050, 1992.

Cornilleau-Wehrin, N., et al., The Cluster Spatio-Temporal Analysis of Field Fluctuations (STAFF) Experiment, *Space Science Reviews*, 79, 107–136, 1997.

Cowley, S. W. H.: The effect of pressure anisotropy on the equilibrium structure of magnetic current sheets, *Planet. Space Sci.*, 26, 1037–1061, 1978.

Daughton, W.: The unstable eigenmodes of a neutral sheet, *Phys. Plasm.*, 6, 1329–1343, 1999.

Daughton, W.: Nonlinear dynamics of thin current sheets, *Phys. Plasmas*, 9, 3668–3678, 2002.

Daughton, W.: Electromagnetic properties of the lower-hybrid drift instability in a thin current sheet, *Phys. Plasmas*, 10, 3103–3119, 2003.

Décréau, P. M. E., et al., Whisper, a Resonance Sounder and Wave Analyser: Performances and Perspectives for the Cluster Mission, *Space Science Reviews*, 79, 157–193, 1997.

Delcourt, D. C., Malova, H. V., and Zelenyi, L. M.: Dynamics of charged particles in bifurcated current sheets: The  $k \sim 1$  regime, *J. Geophys. Res.*, 109, A01222, doi:10.1029/2003JA010167, 2004.

Delcourt, D. C., Malova, H. V., and Zelenyi, L. M.: Quasiadiabaticity in bifurcated current sheets, *Geophys. Res. Lett.*, 33, L06106, doi:10.1029/2005GL025463, 2006.

Drake, J., M. Swisdak, C. Cattell, M. Shay, B. Rogers, and A. Zeiler,: Formation of electron holes and particle energization during magnetic reconnection, *Science*, 299, 873-877, 2003.

Drake, J. F., M. A. Shay, W. Thongthai, and M. Swisdak,: Production of energetic electrons during magnetic reconnection, *Physical Review Letters*, Vol. 94, 095001, 2005.

Eastwood, J. W.: Consistency of fields and particle motion in the “Speiser” model of the current sheet, *Planet. Space Sci.*, 20, 1555–1568, 1972.

Eastwood, J. P., A. Balogh, M. W. Dunlop, T. S. Horbury, and I. Dandouras,: Cluster observations of fast magnetosonic waves in the terrestrial foreshock. *Geophys. Res. Lett.* 29, 2046, doi:10.1029/2002GL015582, 2002.

Eastwood, J. P., A. Balogh, C. Mazelle, I. Dandouras, and H. Rème,: Oblique propagation of 30s period fast magnetosonic foreshock waves: A Cluster case study. *Geophys. Res. Lett.* 31, L04804, doi:10.1029/2003GL018897, 2004.

Eastwood, J., E. A. Lucek, C. Mazelle, K. Meziane, Y. Narita, J. Pickett, and R. Treumann,: The Foreshock. *Space Sci. Rev.* 118: 41–94, 2005.

Eriksson S., M. Øieroset, D. N. Baker, C. Mouikis, A. Vaivads, M. W. Dunlop, H. Rème, R. E. Ergun, A. Balogh,: Walén and slow-mode shock analyses in the near-Earth magnetotail in connection with a substorm onset on 27 August 2001, *J. Geophys. Res.*, 109, A10212, doi:10.1029/2004JA010534, 2004.

Escoubet, C. P., R. Schmidt, and M. L. Goldstein, Cluster: Science and Mission Overview, *Space Sci. Rev.*, 79, 11–32, 1997.

Fairfield, D. H.: On the average configuration of the geomagnetic tail, *J. Geophys. Res.*, 84, 1950–1958, 1979.

Feldman, W. C., et al., Evidence for slow-mode shocks in the deep geomagnetic tail, *Geophys. Res. Lett.*, 11, 599, 1984.

Fitzenreiter, R. J., A. J. Klimas, and J. D. Scudder,: Detection of bump-on-tail reduced electron velocity distributions at the electron foreshock boundary, *Geophys. Res. Lett.*, 11, 496–499, 1984.

Fu, H.S., J.B. Cao, T.L. Zhang, H. Rème, and E. Lucek,: Statistical study of the solar wind deceleration in the Earth's foreshock region, *Chinese Journal of Geophysics*, 52, 4, 895-901, 2009.

Gary, S. P., and T. E. Eastman, The lower hybrid drift instability at the magnetopause, *J. Geophys. Res.*, 84, 7378, 1979.

Genot, V., Mottez, F., Fruit, G., Louarn, P., Sauvaud, J.-A., and Balogh, A.: Bifurcated current sheet: Model and Cluster observations, *Planet Space Sci.*, 53, 229–235, 2005.

Gosling, J. T., M. F. Thomsen, S. J. Bame, W. C. Feldman, G. Paschmann, and N. Sckopke,: Evidence for specularly reflected ions upstream from the quasi-parallel bow shock. *Geophys.Res. Lett.* 9, 1333–1336, 1982.

Gurnett, D. A., R. L. Huff, and D. L. Kirchner, The Wide-Band Plasma Wave Investigation, *Space Science Reviews*, 79, 195–208, 1997.

Harris, E. G.: On a plasma sheath separating regions of oppositely directed magnetic fields, *Nuovo Cimento*, 23, 115–121, 1962.

Hasegawa, A.: *Plasma instabilities and nonlinear effect*, Springer-Verlag, New York, 1975.

Holzer, R. F., M. G. McLeod, and E. J. Smith, Preliminary results from the OGO 1 search coil magnetometer: Boundary positions and magnetic noise spectra, *J. Geophys. Res.*, 71, 1481, 1966

Hones, E. W., Jr.: Substorm processes in the magnetotail: Comments on “On hot tenuous plasma, fireballs, and boundary layers in the Earth’s magnetotail” by L. A. Frank et al., *J. Geophys. Res.*, 82, 5633-5640, 1977.

Hones, E. W.,: Transient phenomena in the magnetotail and their relation to substorms, *Space Sci. Rev.*, 23, 393-410, 1979.

Hones, E. W., Jr., T. A. Fritz, J. Birn, J. Cooney, and S. J. Bame, Detailed observations of the plasma sheet during a substorm on April 24, 1979, *J. Geophys. Res.*, 91, 6845, 1986.

Horbury, T.S., P. J. Cargill, E. A. Lucek, J. Eastwood, A. Balogh, M. W. Dunlop,

K.-H. Fornacon, and E. Georgescu, Four spacecraft measurements of the quasiperpendicular terrestrial bow shock: Orientation and motion, *J. Geophys. Res.*, 107, 1208, 10.1029/2001JA000273, 2002.

Hoshino, M., Nishida, A., Mukai, T., Saito, Y., Yamamoto, T., and Kokubun, S.: Structure of plasma sheet in magnetotail: Doublepeaked electric current sheet, *J. Geophys. Res.*, 101, 24 775–24 786, 1996.

Hoshino, M., T. Mukai, I. Shinohara, Y. Saito, and S. Kokubun,: Slow shock downstream structure in the magnetotail, *J. Geophys. Res.*, 105, 337–347, 2000.

Imada, S., R. Nakamura, P. W. Daly, M. Hoshino, W. Baumjohann, S. Muhlbacher, A. Balogh, and H. Rème,: Energetic electron acceleration in the downstream reconnection outflow region, *J. Geophys. Res.*, 112, A03202, doi:10.1029/2006JA011847, 2007.

Johnstone, A. D., C. Alsop, S. Burge, P. J. Carter, A. J. Coates, A. J. Coker, A. N. Fazakerley, M. Grande, R. A. Gowen, C. Gurgiolo, B. K. Hancock, B. Narheim, A. Preece, P. H. Sheather, J. D. Winningham and R. D. Woodliffe,: PEACE: A Plasma Electron and Current Experiment, *Space Sci. Rev.*, 79, 351-398, 1997.

Kaufmann, R. L., and A. Konradi, Explorer 12 magnetopause observations: Large-scale non-uniform motion, *J. Geophys. Res.*, 74, 3609, 1969.

Kivelson, M. G., and C. T. Russell, *Introduction to Space Physics*, Cambridge University Press, New York, 1995.

LaBelle, J., and R. A. Treumann, Plasma waves at the dayside magnetopause, *Space Sci. Rev.*, 47, 175, 1988.

Lapenta, G. and Brackbill, J. U.: Nonlinear evolution of the lower hybrid drift instability: Current sheet thinning and kinking, *Phys. Plasmas*, 9, 1544–1554, 2002.

Le, G. and C. T. Russell,: A study of ULF wave foreshock morphology - I: ULF foreshock boundary. *Planet. Space Sci.* 40(9), 1203–1213, 1992.

Lemaire, J., Impulsive penetration of filamentary plasma elements into the magnetospheres of the Earth and Jupiter, *Planet. Space Sci.*, 26, 887, 1977.

Lemaire, J., and M. Roth, Penetration of solar wind plasma elements into the

- magnetopause, *J. Atmos. Terr. Phys.*, 40, 331, 1978.
- Lembège, B. and P. Savoini,: Formation of Reflected Electrons Bursts by the Nonstationarity and Nonuniformity of a Collisionless Shock Front, *J. Geophys. Res.* 107, 1037, doi:10.1029/2001JA900128, 2002.
- Lembège, B., J. Giacalone, M. Scholer, T. Hada, M. Hoshino, V. Krasnoselskikh, H. Kucharek, P. Savoini and T. Terasawa,: Selected problems in collisionless-shock physics, *Space Science Reviews* 110, 161–226, 2004.
- Meziane, K. and C. d’Uston,: A statistical study of the upstream intermediate ion boundary in the Earth’s foreshock. *Ann. Geophys.* 16, 125–133, 1998.
- Meziane, K., C. Mazelle, R. P. Lin, D. Le Quéau, D. E. Larson, G. K. Parks, and R. P. Lepping,: Three-dimensional observations of gyrating ion distributions far upstream from the Earth’s bow shock and their association with low-frequency waves. *J. Geophys. Res.* 106, 5731–5742, 2001.
- Meziane, K., M. Wilber, C. Mazelle, D. Le Quéau, H. Kucharek, E. A. Lucek, H. Rème, A. M. Hamza, J. A. Sauvaud, J. M. Bosqued, I. Dandouras, G. K. Parks, M. McCarthy, B. Klecker, A. Korth, M. B. Bavassano-Cattaneo, and R. N. Lundin,: Simultaneous observations of field-aligned beams and gyrating ions in the terrestrial foreshock. *J. Geophys. Res.* 109, A05107, doi:10.1029/2003JA010374, 2004.
- Mottez, F.: Exact nonlinear analytic Vlasov-Maxwell tangential equilibria with arbitrary density and temperature profiles, *Phys. Plasm.*, 10, 2501–2508, 2003.
- Parker, E. N., Sweet’s mechanism for merging magnetic fields in conducting fluids, *J. Geophys. Res.*, 62, 509, 1957.
- Parker, E. N., Dynamics of the Interplanetary Gas and Magnetic Fields., *Astrophysical Journal*, 128, 664, 1958.
- Parks, G.K., E. Lee, F. Mozer, M. Wilber, E. Lucek, I. Dandouras, H. Rème, C. Mazelle, J. B. Cao, K. Meziane, M. L. Goldstein and P. Escoubet,: Larmor radius size density holes discovered in the solar wind upstream of Earth’s bow shock, *Physics of Plasmas* 13, 050701, doi:10.1063/1.2201056, 2006.
- Paschmann, G., N. Sckopke, I. Papamastorakis, J. Asbridge, S. Bame, and J. Gosling,:

Energetization of solar wind ions by reflection from the Earth's bow shock. *J. Geophys. Res.* 85, 4689-4693, 1980.

Paschmann, G., et al., The Electron Drift Instrument for Cluster, *Space Science Reviews*, 79, 233–269, 1997.

Pedersen, A., et al., The Wave Experiment Consortium (wec), *Space Science Reviews*, 79, 93–106, 1997.

Petschek, H. E., Magnetic field annihilation, AAS-NASA Symposium on the Physics of Solar Flares, NASA Spec. Publ. SP-50, 425-439, 1964.

Phan, T.D., C. P. Escoubet, L. Rezeau, R. A. Treumann, A. Vaivads, G. Paschmann, S. A. Fuselier, D. Attie, B. Rogers, and B. U. O. Sonnerup (2005), Magnetopause process, *Space Sci. Rev.* 118: 367–424.

Rème, H., et al., The Cluster Ion Spectrometry (CIS) Experiment, *Space Science Reviews*, 79, 303–350, 1997.

Rème, H., C. Aoustin, J. M. Bosqued, I. Dandouras et al.,: First multispacecraft ion measurements in and near the Earth's magnetosphere with the identical Cluster ion spectrometry (CIS) experiment, *Ann. Geophys.*, 19, 1303-1354, 2001.

Rème, H., I. Dandouras, C. Aoustin, J. M. Bosqued, J. A. Sauvaud, C. Vallat, P. Escoubet, J. B. Cao, J. Shi, M. B. Bavassano-Cattaneo, G. K. Parks, C. W. Carlson, Z. Pu, B. Klecker, E. Moebius, L. Kistler, A. Korth, R. Lundin, and the HIA team, The HIA instrument on board the Tan Ce 1 Double Star near-equatorial spacecraft and its first results, *Annales Geophysicae*, 23, 2757–2774, 2005.

Riedler, W., et al., Active Spacecraft Potential Control, *Space Science Reviews*, 79, 271–302, 1997.

Runov, A., Nakamura, R., Baumjohann, W., Zhang, T. L., Volwerk, M., and Eichelberger, H.-U.: Cluster observations of a bifurcated current sheet, *Geophys. Res. Lett.*, 30(2), 1036, doi:10.1029/2002GL016136, 2003a.

Runov, A., Nakamura, R., Baumjohann, W., Treumann, R. A., et al.: Current sheet structure near magnetic X-line observed by Cluster, *Geophys. Res. Lett.*, 30(11), 1579, doi:10.1029/2002GL016730, 2003b.

Runov, A., Sergeev, V. A., Baumjohann, W., et al.: Electric current and magnetic field geometry in flapping magnetotail current sheets, *Ann. Geophys.*, 23, 1391–1403, 2005, <http://www.ann-geophys.net/23/1391/2005/>.

Savoini, P. and B. Lembège,: Two-dimensional simulations of a curved shock: self-consistent formation of the electron foreshock, *J. Geophys. Res.* 106, 12975-12992, 2001.

Schindler, K. and Birn, J.: Models of two-dimensional embedded thin current sheets from Vlasov theory, *J. Geophys. Res.*, 107(A8), 1193, doi:10.1029/2001JA000304, 2002.

Schwartz, S. J., M. F. Thomsen, and J. T. Gosling,: Ions upstream of the Earth's bow shock – A theoretical comparison of alternative source populations. *J. Geophys. Res.* 88, 2039–2047, 1983.

Schwartz, S.J., Shock and Discontinuity Normals, Mach Numbers, and Related Parameters, in *Analysis Methods for Multi-Spacecraft Data*, Eds. Paschmann and Daly, 1998.

Sergeev, V. A., Mitchell, D. G., Russell, C. T., and Williams, D. J.: Structure of the tail plasma/current sheet at 11 Re and its changes in the course of a substorm, *J. Geophys. Res.*, 98, 17 345–17 365, 1993.

Sergeev, V., Runov, A., Baumjohann, W., Nakamura, R., Zhang, T. L., Volwerk, M., Balogh, A., Rème, H., Sauvaud, J. A., André, M., and Klecker, B.: Current sheet flapping motions and structure observed by Cluster, *Geophys. Res. Lett.*, 30(6), 1327, doi:10.1029/2002GL016500, 2003.

Sergeev, V., Runov, A., Baumjohann, W., Nakamura, R., Zhang, T. L., Balogh, A., Louarn, P., Sauvaud, J.-A., and Rème, H.: Orientation and propagation of current sheet oscillations, *Geophys. Res. Lett.*, 31, L05807, doi:10.1029/2003GL019346, 2004.

Shen, C., M. Dunlop, X. Li, Z. X. Liu, A. Balogh, T. L. Zhang, C. M. Carr, Q. Q. Shi, and Z. Q. Chen, New approach for determining the normal of the bow shock based on Cluster four-point magnetic field measurements, *J. Geophys. Res.*, 112, A03201,

doi:10.1029/2006JA011699, 2007.

Sitnov, M. I., Zelenyi, L. M., Malova, H. V., and Sharma, A. S.: Thin current sheet embedded within a thicker plasma sheet: Self-consistent kinetic theory, *J. Geophys. Res.*, 105, 13 029, doi:2001JA000287, 2000.

Sitnov, M. I., Guzdar, P. N., and Swisdak, M.: A model of the bifurcated current sheet, *Geophys. Res. Lett.*, 30(13), 1712, doi:10.1029/2003GL017218, 2003.

Sitnov, M. I., Swisdak, M., Guzdar, P. N., and Runov, A.: Structure and dynamics of a new class of thin current sheets, *J. Geophys. Res.*, 111, A08204, doi:10.1029/2005JA011517, 2006.

Slavin, J. A., E.J. Smith, B.T. Tsurutani, D.G. Sibeck, H.J. Singer, D.N. Baker, J.T. Gosling, E.W. Hones, and F.L. Scarf,: Substorm associated traveling compression regions in the distant tail: ISEE-3 geotail observations, *Geophys. Res. Lett.*, 11, 657-660, 1984.

Slavin, J. A., D. N. Baker, J. D. Craven, R. C. Elphic ,D. H. Fairfield, L. A. Frank, A. B. Galvin, W. J. Hughes, R. H. Manka, D. G. Mitchell, I. G. Richardson, T. R. Sanderson, D. J. Sibeck, E. J. SmithR, and D. Zwickl,: CDAW-8 observations of plasmoid signatures in the geomagnetic tail: An assessment, *J. Geophys. Res.*, 94, 15153-15175, 1989.

Slavin, J. A., E. I. Tanskanen, M. Hesse, C. J. Owen, M. W. Dunlop, S. Imber, E. A. Lucek, A. Balogh, and K.-H. Glassmeier,: Cluster observations of traveling compression regions in the near-tail, *J. Geophys. Res.*, 110, A06207, doi:10.1029/2004JA010878, 2005.

Smit, G.R., Oscillatory Motion of the Nose Region of the Magnetopause, *J. Geophys. Res.*, 73, 4990, 1968.

Smith, E. J., J. A. Slavin, B. T. Tsurutani, W. C. Feldman, and S. J. Bame, Slow mode shocks in the Earth's magnetotail: ISEE-3, *Geophys. Res. Lett.*, 11, 1054, 1984.

Sonnerup, B. U. O.: Adiabatic particle orbits in a magnetic null sheet, *J. Geophys. Res.*, 76, 8211–8222, 1971.

Southwood, D. J., and M. G. Kivelson,: On the form of the flow in the magnetosheath,

J. Geophys. Res., 97, 2873-2879, 1992.

Speiser, T. W.: Particle Trajectories in Model Current Sheets; 1. Analytical Solutions, J. Geophys. Res., 70, 4219–4226, 1965.

Sweet, P. A., The neutral point theory of solar flares, in *Electromagnetic Phenomenon in Cosmical Physics*, edited by B Lehnert, pp 123-129, Cambridge University Press, New York, 1958.

Thompson, S. M., Kivelson, M. G., Khurana, K. K., McPherron, R. L., Weygand, J. M., Balogh, A., Rème, H., and Kistler, L. M.: Dynamic Harris current sheet thickness from Cluster current density and plasma measurements, J. Geophys. Res., 110, A02212, doi:10.1029/2004JA010714, 2005.

Treumann, R. A., J. LaBelle, and R. Pottelette, Plasma diffusion at the magnetopause: The case of lower hybrid drift waves, J. Geophys. Res., 96, 16,009, 1991.

Treumann, R. A. and M. Scholer: 'The magnetosphere as a plasma laboratory'. In: *The Century of Space Science*. Kluwer Academic, 2001.

Ugai, M.: Computer studies on dynamics of a large-scale magnetic loop by the spontaneous fast reconnection model, *Phys. Plasmas*, Vol 3, 4172-4180, 1996.

Ugai, M.: Basic physical mechanism of reconnection development and magnetic loop dynamics, J. Geophys. Res. 104, 6929-6939, 1999.

Voronkov, I., Runov, A., Koustov, A., Kabin, K., Meurant, M., Donovan, E., Bryant, C., and Spanswick, E.: Features of magnetosphere-ionosphere coupling during breakups and substorm onsets inferred from multi-instrument alignment, Int. Conf. Substorms-8, 319, 2006.

Wilken, B., et al., RAPID - The Imaging Energetic Particle Spectrometer on Cluster, *Space Science Reviews*, 79, 399–473, 1997.

Winske, D., and N. Omidi, Diffusion at the magnetopause: Hybrid simulations, J. Geophys. Res., 100, 11923-11933, 1995.

Woolliscroft, L. J. C., et al., The Digital Wave-Processing Experiment on Cluster, *Space Science Reviews*, 79, 209–231, 1997.

Zelenyi, L., Delcourt, D., Malova, H., Sharma, A., Popov, V., and Bykov, A.: Forced

current sheets in the Earth's magnetotail: Their role and evolution due to nonadiabatic particle scattering, *Adv. Space. Res.*, 30, 1629–1638, 2002.

Zhang, T. L., Nakamura, R., Volwerk, M., Runov, A., Baumjohann, W., Eichelberger, H. U., Carr, C., Balogh, A., Sergeev, V., Shi, J. K., and Fornacon, K.-H.: Double Star/Cluster observation of neutral sheet oscillations on 5 August 2004, *Ann. Geophys.*, 23, 2909–2914, 2005, <http://www.ann-geophys.net/23/2909/2005/>.

Zhu, Z. and Winglee, R. M.: Tearing instability, flux ropes, and the kinetic current sheet kink instability in the Earth's magnetotail: A three-dimensional perspective from particle simulations, *J. Geophys. Res.*, 101, 4885–4897, 1996.